Creation of entangled states of a set of atoms in an optical cavity

Florian Haas

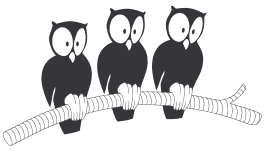

THÈSE DE DOCTORAT
DE L'UNIVERSITÉ PIERRE ET MARIE CURIE

Spécialité : Physique quantique

École doctorale : La physique de la particule à la matière condensée

réalisée au

Département de physique de l'École Normale Supérieure
Laboratoire Kastler Brossel

présentée par

Florian HAAS

pour obtenir le grade de :

DOCTEUR DE L'UNIVERSITÉ PIERRE ET MARIE CURIE

Sujet de la thèse :

Création d'états intriqués d'un ensemble d'atomes dans une cavité optique

À soutenir le 13/02/2014 devant le jury composé de :

M.	Dieter Meschede	Rapporteur
M.	Christoph I. Westbrook	Rapporteur
M	Patrice Bertet	Examinateur
M.	Klaus Mølmer	Examinateur
M.	Jean-Michel Raimond	Examinateur
M.	Jakob Reichel	Directeur de thèse
M.	Jérôme Estève	Membre invité

Summary

In this thesis, we demonstrate the creation and characterization of multiparticle entangled states of neutral atoms with the help of a high finesse cavity.

Our experimental setup consists of a fibre-based high finesse cavity above the surface of an atom chip. It allows us to prepare an ensemble of ^{87}Rb atoms with well-defined atom number. The atoms are trapped in a single antinode of an intracavity standing wave dipole trap and are therefore all equally coupled to the cavity mode. We present a scheme based on a collective, quantum non-destructive (QND) measurement and conditional evolution to create symmetric entangled states and to analyze them at the single-particle level by directly measuring their Husimi Q function. We use this method to create and characterize W states of up to 41 atoms. From the tomography curve of the Q function, we reconstruct the symmetric part of the density matrix via different reconstruction techniques and obtain a fidelity of 0.42.

Furthermore, we have devised an entanglement criterion which only relies on comparing two populations of the density matrix. We use it to infer the degree of multiparticle entanglement in our experimentally created states and find that the state with highest fidelity contains at least 13 entangled particles.

In addition, we show preliminary results on experiments to count the atom number inside a cavity in the QND regime and to create entangled states via quantum Zeno dynamics.

Résumé

Dans cette thèse, nous démontrons la création et la caractérisation d'états intriqués dans un ensemble atomique à l'aide d'un résonateur optique de haute finesse. Notre dispositif expérimental consiste en une cavité fibrée placée en dessous d'une puce à atomes. Les atomes sont tous piégés dans un seul ventre du piège dipolaire créé dans la cavité. Ainsi, ils sont également couplés au mode lumineux de la cavité. Nous présentons une méthode basée sur une mesure collective et non-destructive et une évolution conditionnelle qui sert à créer des états intriqués et symétriques puis à les analyser, avec la résolution d'une particule unique, en mesurant d'une manière directe leur fonction Husimi Q. En utilisant cette méthode, nous créons et caractérisons des états W contenant jusqu'à 41 atomes. Nous reconstituons la partie symétrique de la matrice densité à partir des données expérimentales de la fonction Husimi Q en utilisant différentes méthodes de reconstruction quantique et nous obtenons une fidélité de 0.42. Par ailleurs, nous avons établi un critère d'intrication qui consiste à comparer seulement deux populations de la matrice densité. Nous l'utilisons pour déterminer le degré d'intrication présent dans les états expérimentalement créés et nous trouvons que l'état de fidélité maximale contient au moins 13 particules intriquées. Pour finir, nous présentons des résultats préliminaires concernant des expériences de dénombrement d'atomes dans la cavité en régime de mesures non-destructives ainsi que des expériences de création d'états intriqués en se servant de la dynamique Zénon quantique.

Contents

Introduction

In the early days of quantum mechanics, supporters and critics illustrated the often counterintuitive consequences of the new theory by thought experiments, where single particles would interact with single photons, completely isolated from the environment. Prominent examples include Einstein's box, Heisenberg's microscope and Schrödinger's cat, the latter of which has attracted widespread interest even beyond the field of physics. These thought experiments proved very useful for the development of consistent concepts and the general understanding of the new theory, but they were considered to be purely theoretical. As late as 1952, Schrödinger wrote [1]:

> "We never experiment with just one electron or atom or (small) molecule. In thought experiments we sometimes assume that we do; this invariably entails ridiculous consequences."

Since then, there has been remarkable progress in the experimental investigation and control of quantum systems. Particularly in the field of atomic physics, where advancements have often been stimulated by the field of optics and vice versa: Until the 1940s, light was just used to investigate the properties of matter in spectroscopy experiments, but soon thereafter, the invention of the laser allowed to manipulate the atoms' external and internal degrees of freedom. The concepts of optical pumping [2], laser cooling [3, 4], magneto-optical traps [5] and optical traps [6, 7] were developed to control atoms with light. The high level of precision that has been obtained by now is impressively illustrated by the preparation of Bose-Einstein condensates (BEC) with both atoms [8, 9] and photons [10]. This development was honored by the attribution of the Nobel prize 1997 "for development of methods to cool and trap atoms with laser light" (to Claude Cohen-Tannouji, Stephen Chu and William Phillips) and the Nobel prize 2001 "for the achievement of Bose-Einstein condensation in dilute gases of alkali atoms" (to Eric Cornell, Carl Wieman and Wolfgang Ketterle). Thanks to these efforts and achievements during the last century, we are now in the fortunate situation to be able to experimentally realize some of the thought experiments that 60 years ago were thought to be impossible.

The research field of cavity quantum electrodynamics (CQED) can be seen as the fusion between the progress in experimental control of quantum systems and the desire to study the interaction between single photons and atoms in the spirit of thought experiments. In 1946, Purcell predicted that it is possible to change the decay properties of an atom when it is placed inside a cavity [11]. The cavity mirrors modify the density of electromagnetic modes in which the atom can emit. If the cavity is not resonant to the atomic transition, the emission rate is therefore reduced and the atom can be held in the excited state for a longer time. If the cavity is resonant, the emission rate is enhanced and the photon usually leaves the system via the cavity. However, if the cavity mirrors are sufficiently good, the photon stays in the cavity and can be reabsorbed by the atom. In the regime where the interaction between the cavity mode and the atom

surpasses the losses of the experimental system, the energy is thus coherently exchanged between the atom and the light field. This situation has first been described by Jaynes and Cummings [12]. Since then, CQED has been a vivid field of experimental research, demonstrating fascinating results such as the time-resolved observation of decoherence [13], the demonstration of a light switch realized by a single atom [14] or the stabilization of a quantum state in a feedback scheme [15]. The physical situation of CQED has been experimentally realized in a variety of different systems, such as Rydberg atoms in a microwave cavity [16, 17], neutral atoms in an optical cavity [18], superconducting qubits coupled to microwave stripline resonators [19] or quantum dots in a semiconductor microcavity [20]. Again, the impact and success of this area of research can be illustrated by the fact that a Nobel prize has recently been awarded to a researcher in this field "for ground-breaking experimental methods that enable measuring and manipulation of individual quantum systems" (2012, Serge Haroche together with David Wineland).

This thesis experimentally studies the regime where not only one, but an ensemble of atoms is placed inside a cavity. The physical concepts behind such an experimental system have already been theoretically studied as early as 1954, when Dicke found that N atoms cannot be considered independent when they equally couple to a mode of the electromagnetic field [21]. Instead, they collectively absorb radiation, which creates correlations between the atoms. The behavior of the system is thus fundamentally linked to the concept of multiparticle entanglement, which is one of the most intriguing and puzzling manifestations of quantum mechanics. The properties of two or more particles can be interwoven so that the result of a measurement on one particle is correlated to the results of measurements on the other particles [22]. The collective interaction between the atoms and the cavity mode makes CQED a convenient field to create and study multiparticle entanglement, leading to the observation of interesting new phenomena such as an atom number dependent mode splitting [23], superradiance [24] and the Dicke quantum phase transition [25]. Multiparticle entangled states are not only interesting from a fundamental point of view but also have practical applications. The attempt to harness the properties of entangled states has motivated the creation of new fields of research, which can be subsumed under the term of quantum information. Examples are:

- Quantum computation, which aims at using the properties of entangled states to increase computational power beyond classically possible performance [26]. The classical bit as the smallest storage unit is replaced by a "quantum bit" or qubit, which can take the values of a classical bit and any superposition between them. The computations are performed in quantum gate operations, which entangle different qubits. In order for the quantum computer to be superior to its classical counterpart, the entanglement has to be maintained during the whole computational operation.
- Quantum cryptography, where quantum states are used as information carriers to enable secure communication [27]. In the most common schemes, single photons serve as "flying qubits" to transport information between remote locations. However, communication over long distances is impeded because of unavoidable losses in the transmission channel. Simple amplification of the quantum signal is impossible

due to the no-cloning theorem. That is why the concept of "quantum repeaters" [28] was devised, at the heart of which lies an ensemble of entangled particles. The quantum state of a photon can be mapped onto this ensemble and stored for long periods of time. Concatenating several quantum repeaters can enhance the distance over which entanglement can be distributed.

- Quantum metrology, which improves the precision of interferometric measurements by exploiting quantum correlations in an entangled ensemble [29]. The direction of the total pseudospin of uncorrelated particles necessarily carries a minimum uncertainty, which prohibits phase measurements below a certain limit. Specifically tailored entangled states can redistribute the spin uncertainty to be more sensitive in the spin direction that is measured [30].

Attempts to create and characterize entangled states are pursued in diverse physical systems. The different approaches can be divided into two classes:

The "bottom up" approach, where entanglement is produced in quantum gate operations and where single qubit addressing is possible. Such systems are e.g. ions in linear Paul traps [31, 32, 33] or superconducting qubits [34, 35, 36]. The state characterization is realized by state readout of the individual particles, which quickly becomes cumbersome and time consuming when the number of particles is scaled up. In the case of ions, several technical challenges also impede an increase in the number of particles [37]. Therefore the number of entangled particles in these systems to date is limited to less than 20 qubits [38].

The other approach is to create entanglement in big ensembles, using some form of collective interaction. It is realized in spin squeezing experiments [39, 40, 41, 42] or in experiments where a single excitation is stored in an atomic cloud (e.g. in a DLCZ scheme [43, 44] or via the Rydberg blockade [45]). In all these examples, the analysis is not performed with single-particle resolution, which means that the states cannot be controlled at the quantum limit ((as required, for example, to reach the Heisenberg limit of quantum metrology [29]).

In this thesis, we present a new approach to create and analyze multiparticle entangled states based on CQED. Our experimental setup combines an atom chip with a fibre-based Fabry Pérot cavity of high finesse and enables us to load a cloud of ultracold ^{87}Rb atoms into one single antinode of the intracavity standing-wave dipole trap, which leads to identical coupling between the atoms and the cavity mode. We create entanglement in the atomic ensemble via collective evolution and a non-destructive cavity-based measurement of the atomic state. The creation of entanglement via collective measurement is advantageous because it is in principle independent of atom number. Here, it is realized for the first time with precision at the single particle level.

We have also devised a new method to characterize the state using the cavity measurement. We directly measure the Husimi Q function of the state, which enables us to infer the symmetric part of its density matrix. We use this method to create and characterize W states of different atom number and obtain a fidelity of 0.42 for a state containing 41 atoms. An analysis of the reconstructed density matrix shows that the state contains at least 13 entangled particles. The presented method constitutes the first direct measurement of a quasiprobability distribution for material particles and enables

the analysis of large entangled states at the single particle level.

Our experiments thus take a special position in the research field of entanglement creation and analysis: They combine the atom number scalability of schemes relying on collective interaction with single particle resolution known from experiments with ions or superconducting qubits. The states presented in this thesis constitute to our knowledge the highest number of entangled particles that have been analyzed at the single particle level.

Outline of the thesis

The first chapter introduces the theory of a cavity-based collective measurement. We first consider the case of a single atom strongly coupled to the cavity mode and discuss deviations because of real-life atoms and cavities. We then extend the theory to N atoms in the cavity and also analyze the errors and limits of a quantum non-destructive (QND) measurement in this situation.

The second chapter gives a short summary on the experimental setup and describes the steps to cool atoms from a vapor at room temperature and to load them into the intracavity dipole trap.

The third chapter is devoted to techniques for preparing and counting atom numbers. We present a method to prepare a well-defined atom number in the cavity and demonstrate its experimental realization. Furthermore, we compare the signal-to-noise ratio of different counting methods and propose a scheme to count atom numbers in the QND regime.

In the fourth chapter, we present the preparation and characterization of multiparticle entangled states. We introduce the principle and experimental parameters of our entanglement method and explain how the Husimi Q function can be measured with our cavity. We show tomography on experimentally created coherent states and W states with three different atom numbers and also analyze their temporal evolution.

In chapter five, the density matrices are reconstructed from their Q function with three different techniques and a criterion is derived to infer the depth of entanglement in the reconstructed state. We also investigate the limits to the fidelity of our preparation method.

Chapter six presents a proposition to create entanglement via QZD. We use a simulation to infer the optimal experimental parameters and to give an upper limit for the attainable fidelity. We also show preliminary experimental results.

Finally, a conclusion summarizes the main results and gives an outlook on future experiments.

1. Collective QND measurements in an atomic ensemble

In this chapter, we theoretically describe the principle which is at the heart of all the experiments presented in this thesis: A collective state measurement of an atomic ensemble in the quantum non-destructive (QND) regime. Such a measurement is realized with the help of a high-finesse cavity. We therefore briefly review the Jaynes-Cummings model, which constitutes the simplest case of a two-level system interacting with one single mode of the electromagnetic field. We then extend our considerations to open systems and show that our setup is a convenient tool to infer the internal state of a single atom. We also investigate the influence of deviations from the simple theoretical model such as the multilevel structure of the atom. We then discuss the main consequences when not only one, but many atoms interact with the light field and show that the cavity is a convenient tool to infer if all the atoms are in the same internal state. We finally discuss fundamental limits of the collective, QND nature of this measurement and investigate how its errors scale with atom number.

1.1. The Jaynes-Cummings Hamiltonian

We consider a two-level atom with levels $|\mathrm{g}\rangle$ and $|\mathrm{e}\rangle$, coupled to a single mode of the electromagnetic field via electric dipole interactions. The system is described by the Jaynes-Cummings Hamiltonian H [12]:

$$H = H_a + H_c + H_{JC} \tag{1.1}$$

with

$$\begin{aligned} H_a &= \hbar\omega_a \sigma^+\sigma^- \\ H_c &= \hbar\omega_c a^\dagger a \\ H_{JC} &= \hbar g(a^\dagger\sigma^- + a\sigma^+) \end{aligned} \tag{1.2}$$

Here, we have used the rotating wave approximation and defined the vacuum as the zero energy of the field. $\sigma^+ \equiv |\mathrm{e}\rangle\langle\mathrm{g}|$ ($\sigma^- \equiv |\mathrm{g}\rangle\langle\mathrm{e}|$) denotes the atomic rising (lowering) operator and $a^\dagger$ (a) denotes the creation (annihilation) operator of the electromagnetic mode. $\omega_a/2\pi$ and $\omega_c/2\pi$ are the resonance frequencies of the atom and the light field, respectively. The last term H_{JC} in (1.1) describes the interaction between the atom and the light field. It features the processes of the atom performing a transition from $|\mathrm{e}\rangle$ to $|\mathrm{g}\rangle$ while emitting a photon to the light mode ($a^\dagger\sigma^-$) and the absorption of a photon which changes the atomic state from $|\mathrm{g}\rangle$ to $|\mathrm{e}\rangle$ ($a\sigma^+$). Experimentally, such a system can be realized by placing the atom in a cavity, which filters out one single mode of the electromagnetic field and enhances the electric field of a single photon. The strength of this interaction, given by the coupling constant g, is then dependent on the cavity mode

volume V and the atomic matrix element μ_{ge}:

$$g = \sqrt{\frac{\omega_c}{2\hbar\epsilon_0 V}}\,\mu_{\mathrm{ge}} \tag{1.3}$$

The Hamiltonian H from (1.1) can be diagonalized and the eigenstates are

$$\begin{aligned} |+,n\rangle &= \cos(\theta_n/2)\,|\mathrm{e},n\rangle + \sin(\theta_n/2)\,|\mathrm{g},n+1\rangle \\ |-,n\rangle &= -\sin(\theta_n/2)\,|\mathrm{e},n\rangle + \cos(\theta_n/2)\,|\mathrm{g},n+1\rangle \end{aligned} \tag{1.4}$$

with

$$\tan\theta_n = \frac{g\sqrt{n}}{\Delta_{ac}/2 + \sqrt{g^2 n + (\Delta_{ac}/2)^2}} \qquad \Delta_{ac} = \omega_a - \omega_c \tag{1.5}$$

These states are called "dressed states", since they combine the atomic and photonic parts of the system. The corresponding eigenvalues are

$$E_n^{\pm} = n\hbar\omega_c + \frac{\hbar}{2}(\Delta_{ac} \pm \sqrt{\Delta_{ac}^2 + 4g^2 n}) \tag{1.6}$$

For $\Delta_{ac} = 0$, the two eigenenergies with n excitations are split by the frequency $2g\sqrt{n}$. In the case of $n = 1$, this effect is known as "vacuum Rabi splitting".

1.2. Characterization of the open system

The Hamiltonian approach is not sufficient to describe the phenomena we encounter in real-life experiments, since it does not include losses or pumping of the system. In reality, the system is coupled to the environment by the incoherent processes of atomic decay (i.e. spontaneous emission) γ and cavity decay κ. In addition, we can coherently excite the system by pumping the cavity at a rate η. Figure 1.1 schematically summarizes the relevant processes of the open atom-cavity system.

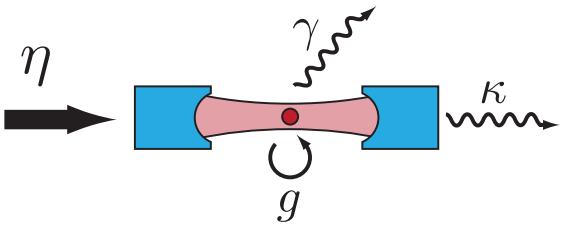

Figure 1.1.: Schematic of the open atom-cavity system. The cavity is pumped coherently at a rate η. Decay can either occur via cavity leakage (at a rate κ) or via spontaneous emission of the atom (at a rate γ). The coupling strength between the atom and the cavity mode is g.

The master equation

To include these processes, we use a master equation approach [46]: We assume that

the system is coupled to a reservoir of modes and calculate the joint evolution of the system and its environment by solving the master equation

$$\begin{aligned} \dot{\rho} &= \mathcal{L}\rho \\ \mathcal{L}\rho &= -\frac{i}{\hbar}[H,\rho] + \kappa\mathcal{D}_a\rho + \gamma\mathcal{D}_{\sigma^-}\rho \end{aligned} \tag{1.7}$$

The loss processes due to atomic decay and cavity decay are included as superoperators $\mathcal{D}$. Here, $\mathcal{D}_c$ associated with the operator c, is defined as

$$\mathcal{D}_c\rho \equiv 2c\rho c^\dagger - \{\rho, c^\dagger c\}, \tag{1.8}$$

with $\{\cdot,\cdot\}$ being the the anti-commutator. The pump term is added to the Hamiltonian as [47]:

$$H_P = -i\eta(a\mathrm{e}^{i\omega_p t} - a^\dagger \mathrm{e}^{-i\omega_p t}) \tag{1.9}$$

H then reads (in the frame rotating at the pump frequency ω_p):

$$H = \Delta_{ap}\sigma^+\sigma^- + \Delta_{cp}a^\dagger a + g(a^\dagger\sigma^- + a\sigma^+) - i\eta(a - a^\dagger) \tag{1.10}$$

with $\Delta_{ap} = \omega_a - \omega_p$ and $\Delta_{cp} = \omega_c - \omega_p$.

Solution to the master equation

Under the assumption of weak probing (i.e. only considering the three states $|\mathrm{g},0\rangle$, $|\mathrm{g},1\rangle$ and $|\mathrm{e},0\rangle$), the master equation (1.7) can be solved analytically [48] and we directly give the steady state solution here. The expectation values p_{ex} for the atomic excitation and n_{cav} for the intracavity photon number are

$$p_{\mathrm{ex}} = \langle\sigma^+\sigma^-\rangle = \frac{\eta^2 g^2}{\left|g^2 - \widetilde{\Delta}_{ap}\widetilde{\Delta}_{cp}\right|^2} \tag{1.11}$$

$$n_{\mathrm{cav}} = \langle a^\dagger a\rangle = \frac{\eta^2\left|\widetilde{\Delta}_{ap}\right|^2}{\left|g^2 - \widetilde{\Delta}_{ap}\widetilde{\Delta}_{cp}\right|^2} \tag{1.12}$$

with $\widetilde{\Delta}_{ap} = \Delta_{ap} - i\gamma$ and $\widetilde{\Delta}_{cp} = \Delta_{cp} - i\kappa$.

η^2/κ is the incoming photon rate. Since we assume lossless cavity mirrors, it is proportional to the intracavity photon number for an empty cavity on resonance:

$$\frac{\eta^2}{\kappa} = \kappa\, n_{\mathrm{cav}}(g = 0, \Delta_{cp} = 0) \tag{1.13}$$

We can obtain information from the system by analyzing the cavity transmission T. It is related to n_{cav} via

$$T = \kappa\, n_{\mathrm{cav}}. \tag{1.14}$$

In figure 1.2, we compare T for $g = 2\pi\cdot 240\,\mathrm{MHz}$ (blue curve) and $g = 0$ (green curve) in dependence of the atom probe detuning Δ_{ap}. For $g = 0$, we simply obtain the Lorentzian curve of an empty cavity transmission. In contrast, for $g = 2\pi\cdot 240\,\mathrm{MHz}$, the transmission features two peaks which are shifted from the initial resonance. These maxima

correspond to the non-degenerate eigenenergies $E_0^{\pm}$ of the coupled system (see (1.6)). We can thus use the cavity to detect single atoms: If we tune the probe light and the cavity resonant to the atomic transition ($\Delta_{ap} = 0$, $\Delta_{cp} = 0$), the transmission is reduced by a factor

$$\frac{T_{\text{atom}}}{T_0} = \frac{1}{1 + \frac{g^2}{\kappa\gamma}} \equiv \frac{1}{(1+2C)^2} \simeq \frac{1}{4C^2} \tag{1.15}$$

with respect to the empty cavity transmission T_0. Here, we introduced the cooperativity C:

$$C = \frac{g^2}{2\kappa\gamma} \tag{1.16}$$

If the coupling g is stronger than the losses κ, γ, then $C > 1$ and the system is governed by coherent evolution. The behavior of the coupled system is then conceptually different from the behavior of an empty cavity as can be seen in the cavity transmission. This experimental regime is known as "strong coupling regime".

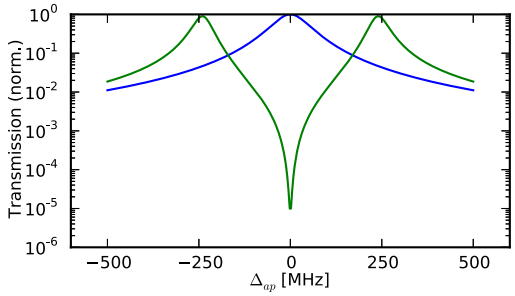

Figure 1.2.: Cavity transmission as a function of the probe laser detuning with the cavity resonance being fixed at the atomic frequency ($\Delta_{ap} = \Delta_{cp}$). The blue curve shows the signal of an empty cavity. This signal is strongly modified if a single resonant two-level atom is placed inside the cavity (green curve). The curves are plotted for the parameters of our experimental setup ($g = 2\pi \cdot 240\,\text{MHz}$, $\gamma = 2\pi \cdot 3\,\text{MHz}$, $\kappa = 2\pi \cdot 53\,\text{MHz}$).

The reduced intracavity photon number also leads to a reduced scattering rate Γ_{eff} of the atom:

$$\Gamma_{\text{eff}} = 2\gamma p_{\text{ex}} = \frac{2\gamma\eta^2 g^2}{|g^2 - \kappa\gamma|^2} \simeq \frac{2\gamma\eta^2}{g^2} = \frac{1}{C}\frac{\eta^2}{\kappa} \tag{1.17}$$

with p_{ex} being the population in the excited state $|e\rangle$. We see that the scattering rate per incoming photon is reduced by the cooperativity C.

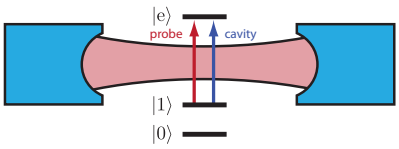

Figure 1.3.: Schematic of our experimental configuration to detect the atomic state. A three-level atom is placed inside a cavity. The cavity and the probe light is resonant with the atomic transition $|1\rangle \rightarrow |e\rangle$. In contrast, the other atomic transitions ($|0\rangle \rightarrow |e\rangle$, $|0\rangle \rightarrow |1\rangle$) are far from resonance.

Internal state detection

We use this manifestation of the vacuum Rabi splitting to infer the internal state of an atom. Consider a three-level atom in a high-finesse cavity (see figure 1.3). To infer if the atom is in state $|0\rangle$ or $|1\rangle$, we tune the cavity and probe light resonant to the transition $|1\rangle \rightarrow |e\rangle$. We coherently probe the cavity and observe photon counts in transmission with Poisson distribution and a different mean value T according to the internal state of the atom: If the atom is in $|1\rangle$, the mean cavity transmission $T_{|1\rangle}$ is low (as shown in the green curve of figure 1.2) due to the vacuum Rabi splitting. On the other hand, if the atom is in $|0\rangle$, the Lorentzian curve of the cavity resonance is basically undisturbed and the mean cavity transmission $T_{|0\rangle}$ is high. We choose a threshold value in between $T_{|0\rangle}$ and $T_{|1\rangle}$ and assign the outcome to $|1\rangle$ if the counted photon number is below the threshold, and to $|0\rangle$ if it is above. Figure 1.4 shows a schematic of the count distributions of the two possible outcomes and the threshold.

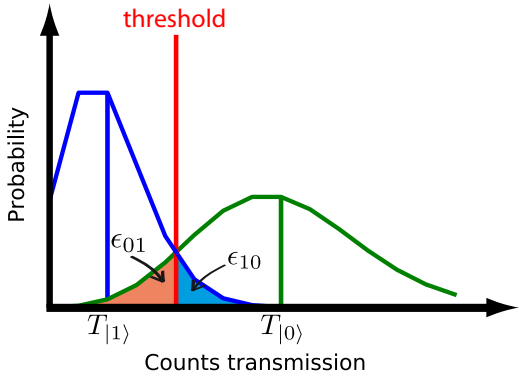

Figure 1.4.: Schematic of the count distribution in transmission for the two different measurement outcomes. We choose a threshold (red) and assign the counted photon number to the state $|1\rangle$ ($|0\rangle$) if it is below (above) the threshold. This results in a detection error ϵ_{10} (ϵ_{01}), which corresponds to the light blue (light red) area.

The detection error ϵ of such a measurement can be defined as the mean value of the two state dependent errors ϵ_{01} and ϵ_{10}:

$$\epsilon = \frac{\epsilon_{01} + \epsilon_{10}}{2} \tag{1.18}$$

where ϵ_{01} (ϵ_{10}) is the probability to wrongly conclude that the atom is in the state $|1\rangle$ ($|0\rangle$) while in reality it is in $|0\rangle$ ($|1\rangle$). ϵ_{01} (ϵ_{10}) can be calculated as the integral of the Poisson distribution with mean $T_{|0\rangle}$ ($T_{|1\rangle}$) below (above) the threshold. The measurement error ϵ can be reduced if a higher number of photons is sent onto the cavity. The overlap of the distributions then becomes smaller, which makes the internal atomic states more easily distinguishable.

In the case of our experimental setup, the transmission signal is modified so strongly, that a low number of probing photons is sufficient to infer the state. This allows us to measure the internal state without the occurrence of a spontaneous emission event: If the atom is in $|1\rangle$, the scattering rate is strongly reduced by the factor $1/C$ (see (1.17)).

On the other hand, if the atom is in $|0\rangle$, the intracavity light field is not resonant to the atomic transition. Typical detection errors as well as scattering probabilities are given in the next section.

1.3. Real-life atoms and cavities

Our experimental system consists of ^{87}Rb atoms, optically trapped in a fibre-based Fabry Pérot (FFP) cavity. The optical trap, imperfect cavity mirrors and the multilevel structure of the atom cause the system to behave differently from the simple model presented in the previous section. With the right experimental configuration, we can nevertheless realize it to good approximation.

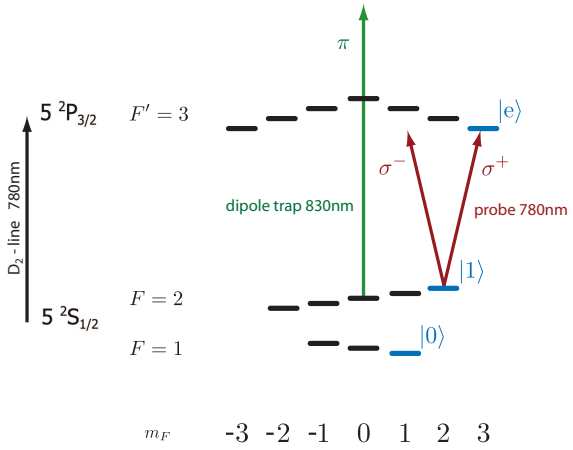

Figure 1.5.: The relevant part of the ^{87}Rb level scheme with the experimental configuration chosen for the experiments presented in this thesis. The dipole trap light is π-polarized and its light shift is m_F-dependent for the excited states. We send σ^+/σ^--polarized light into the cavity at a frequency resonant to the $|F = 2, m_F = 2\rangle \rightarrow |F' = 3, m_{F'} = 3\rangle$ transition. A magnetic field of 12.5 G, oriented along the polarization of the dipole light, lifts the degeneracy of the hyperfine ground states. The transitions between the levels in $F = 1$ and $F = 2$ can therefore be addressed individually with a microwave. For our experiments, we choose the states $|0\rangle \equiv |F = 1, m_F = 1\rangle$, $|1\rangle \equiv |F = 2, m_F = 2\rangle$ and $|e\rangle \equiv |F' = 3, m_{F'} = 3\rangle$, which realize a three-level system to good approximation.

Figure 1.5 shows the relevant level scheme of ^{87}Rb. We choose the D_2-line as the optical transition because of its comparatively high transition dipole matrix element. Due to birefringence in the mirror coatings, the cavity has two non-degenerate linear polarized eigenfrequencies [1]. The intracavity light is therefore necessarily linearly polarized. The light shift of a linearly polarized dipole trap is m_F-dependent for the excited states [49, 50] and orders the Zeeman levels of the $F' = 3$ manifold in a triangular structure as shown in figure 1.5. The linearly polarized probe light cannot exclusively probe the closed optical transition $|F = 2, m_F = 2\rangle \rightarrow |F' = 3, m_{F'} = 3\rangle$. We choose its polarization orthogonal to the dipole light, which results in σ^+/σ^- polarized light in the atomic frame.

1. The cavity is presented in detail in section 2.2.

A closed transition is therefore realized to good approximation, since the σ^--polarized light is tuned far from resonance due to the light shift of the optical dipole trap.

In addition, we apply a homogeneous magnetic bias field in the direction of the dipole trap polarization to lift the degeneracy in the hyperfine ground state manifolds $F = 1$ and $F = 2$. We can thus individually address the transitions between Zeeman levels in the hyperfine ground state (using a microwave) and encode our qubit states $|0\rangle$ and $|1\rangle$ in the states $|F = 1, m_F = 1\rangle$ and $|F = 2, m_F = 2\rangle$, respectively. With the excited state $|\mathrm{e}\rangle = |F' = 3, m_{F'} = 3\rangle$, this configuration realizes a three-level system like the one mentioned in the previous section to good approximation.

To quantitatively estimate the influence of the real-world atom and cavity, a master equation of the experimental system has been set up and solved numerically [51]. This master equation includes coupling between the $F = 2$ hyperfine ground state and all hyperfine states of the $5^2\mathrm{P}_{3/2}$ multiplet, the two cavity modes with orthogonal polarization, a light shift due to a linearly polarized dipole trap and a homogeneous magnetic field. The steady state solution shows that the experimental configuration presented in figure 1.5 is indeed the optimal choice for QND measurements [51]. We therefore use it in all experiments presented in this thesis. Figure 1.6a) and b) show the transmission T and the population p_{ex} in the $F' = 3$ manifold.

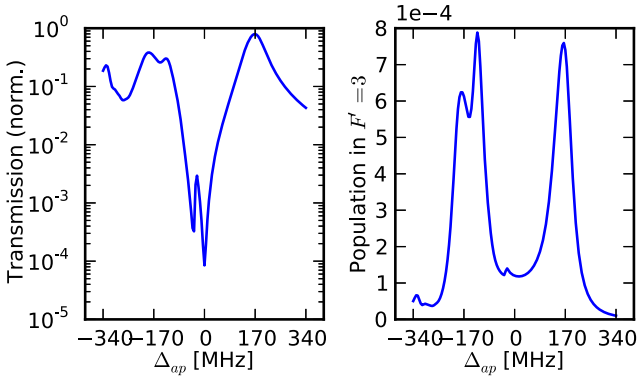

Figure 1.6.: Cavity transmission and population in the $F' = 3$ manifold according to the solution of the full master equation. The curves are calculated for the parameters of our experimental setup ($g_0 = 2\pi \cdot 240\,\mathrm{MHz}$, $\gamma = 2\pi \cdot 3\,\mathrm{MHz}$, $\kappa = 2\pi \cdot 53\,\mathrm{MHz}$), the light configuration shown in figure 1.5, a pump rate $\eta = 2\pi \cdot 1.9\,\mathrm{MHz}$ and a magnetic field $B = 12.5\,\mathrm{G}$ parallel to the dipole trap polarization. With respect to figure 1.2, the transmission features a more complex spectrum, because the multilevel structure of the atom is taken into account. The asymmetry with respect to the detuning between the probe laser frequency and the atomic transition Δ_{ap} is due to the m_F-dependent light shift of the dipole trap and the magnetic field.

The lowest transmission $T_{\mathrm{min}} = 8.5 \cdot 10^{-5}\, T_0$ is obtained when cavity and probe are resonant to the $|1\rangle \rightarrow |\mathrm{e}\rangle$ transition. This value allows us to assign an error to the state detection measurement. Furthermore, the population $p_{\mathrm{ex,min}} = 1.2 \cdot 10^{-4}$ in the $F' = 3$ manifold relates the number of incoming photons to the number of scattered photons via (1.17). Figure 1.7 summarizes this information. It shows the mean detection error of the state detection measurement in dependence of the mean number scattered photons. Here, we have also taken into account the increase in detection error due to optical losses

of the cavity, the fibres and the single photon detection setup. The value $T_{\min}$ is not as low as theoretically expected for a perfect two-level system with the same experimental parameters ($T_{\min}^{\text{theor}} = {}^{T_0}/_{4C^2} = 8 \cdot 10^{-6}$ for $C = 181$), but is still sufficiently low to measure the atomic hyperfine state with high fidelity and without spontaneous emission: We obtain from the graph that we can infer the atomic state with an error below 10% at a scattering probability of 0.2.

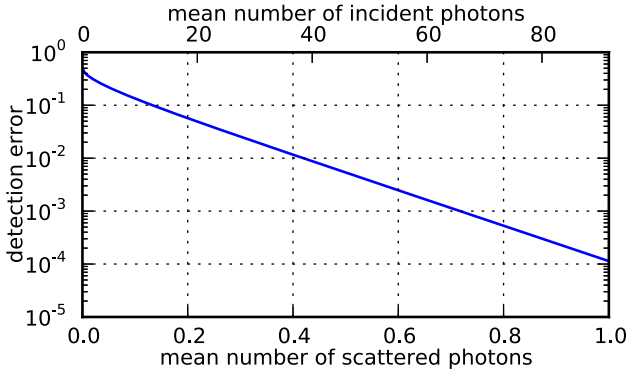

Figure 1.7.: The detection error of the hyperfine state measurement in dependence of the mean number of scattered photons and incident photons as expected from the solution of the master equation. For a higher number of probing photons, the detection error decreases while the mean number of scattered photons increases.

1.4. Cavity QED with an atomic ensemble

1.4.1. The Tavis-Cummings Hamiltonian

In the previous sections, we only considered a single atom coupled to a cavity mode. We now study the consequences on the state detection scheme if not only one, but N atoms are placed inside the cavity. For N two-level atoms equally coupled to the cavity mode, the Jaynes-Cummings Hamiltonian (1.1) has to be expanded to the Tavis-Cummings Hamiltonian H_N [52], which takes into account the energies and interactions of all N atoms:

$$H_N = \hbar\omega_c a^\dagger a + \hbar\omega_a \sum_{i=1}^{N} \sigma_i^+ \sigma_i^- + \hbar g \sum_{i=1}^{N} (a^\dagger \sigma_i^- + a\sigma_i^+) \tag{1.19}$$

The ground state of the system is $|0_c\rangle \equiv \left|g_1, g_2, \ldots, g_N, 0_{\text{ph}}\right\rangle$ with 0_{ph} being the ground state of the cavity field. If the system contains one single excitation, it can either be stored in the light field

$$|1_{c,\,\text{cavity}}\rangle \equiv \left|g_1, g_2, \ldots, g_N, 1_{\text{ph}}\right\rangle \tag{1.20}$$

or in the atomic ensemble. Due to the symmetry of the system, the excitation must then be equally shared by all the atoms:

$$|1_{c,\,\text{atoms}}\rangle = {}^1/\sqrt{N} \left(\sum_{i=1}^{N} \left|g_1, \ldots, e_i, \ldots, g_N, 0_{\text{ph}}\right\rangle \right) \tag{1.21}$$

This coherent, symmetric superposition of N-particle states is known as Dicke state. It has been introduced in [21] to describe the collective light emission from a cloud of atoms.

As in the single atom case, the eigenstates of the Hamiltonian (1.19) are dressed states, containing weighted contributions of the atomic and photonic excitation states. On resonance ($\omega_c = \omega_a$), the eigenstates with one excitation read [2]

$$|\pm, 1_N\rangle \equiv \frac{1}{\sqrt{2}} \left(|1_{c,\,\mathrm{cavity}}\rangle \pm |1_{c,\,\mathrm{atoms}}\rangle \right) \tag{1.22}$$

The spacing between the corresponding eigenenergies is proportional to $\sqrt{N}$:

$$E_{\pm,N} = \hbar\omega_c \pm \hbar\sqrt{N}g \tag{1.23}$$

The system thus behaves as if one "superatom" was coupled to the cavity field with a coupling constant $\widetilde{g} = \sqrt{N}g$.

When we consider the open system, we have to use a master equation approach similar to the one for the single-atom system [53] (cf 1.7):

$$\begin{aligned} \dot{\rho} &= \mathcal{L}\rho \\ \mathcal{L}\rho &= -\frac{i}{\hbar}[H_N, \rho] - \frac{i}{\hbar}[H_P, \rho] + \kappa\mathcal{D}_a\rho + \gamma \sum_{i=1}^{N} \mathcal{D}_{\sigma_i^-}\rho \end{aligned} \tag{1.24}$$

The results are analogue to the single-atom case when we define a collective cooperativity C_N:

$$C_N = \frac{\widetilde{g}^2}{2\kappa\gamma} = NC \tag{1.25}$$

The transmission T_N at resonance is reduced by a factor

$$\frac{T_N}{T_0} = \frac{1}{4C_N^2} = \frac{1}{N^2}\frac{1}{4C^2} \tag{1.26}$$

The total scattering rate, however, is the same as in the single atom case (cf. (1.17)):

$$\Gamma_{\mathrm{eff,N}} = \frac{N}{C_N}\frac{\eta^2}{\kappa} = \Gamma_{\mathrm{eff}} \tag{1.27}$$

1.4.2. State measurement in an ensemble

We now consider this result regarding our experimental system, namely a total number of N ^{87}Rb atoms in the cavity with a configuration as presented in figure 1.5. Equation (1.26) makes it seem possible to infer the number of atoms in the state $F = 2$ by probing the cavity on resonance and analyzing the transmission. However, we will find in the following that we can only distinguish if all atoms are in $F = 1$, or if at least one atom is in the hyperfine state $F = 2$. This is due to the fact that the cavity transmission is

2. There exist N-1 additional eigenstates. They are dark states and cannot be excited by driving the cavity mode. Therefore, they are not considered in the following.

already strongly reduced by a single atom in $F = 2$. Additional atoms in $F = 2$ do not measurably lower the transmission further.

We can quantitatively illustrate this by comparing the measurement signals for one or two atoms in $F = 2$. To infer the state inside the cavity, we have to assign the measurement result - a counted photon number n - to one of the possible Poisson distributions with the mean transmission T_1 for one atom in $F = 2$, and T_2 for two atoms in $F = 2$. We first consider the case of a measurement without spontaneous emission: Figure 1.7 shows that we must keep the number of incoming photons below 20, if we want to keep the single atom scattering probability below 0.2. The transmittance and losses of our cavity mirrors [3] lead to the fact that only 13% of the incoming photons are transmitted, if the cavity is on resonance and no atoms are in $F = 2$:

$$T_0 = 0.13 \cdot 20 = 2.6 \tag{1.28}$$

If one atom is in $F = 2$, the cavity transmission is reduced by $1/4C^2$:

$$T_1 = \frac{1}{4C^2} T_0 = 2.6 \cdot 10^{-4} \tag{1.29}$$

A second atom in $F = 2$ reduces the transmission further:

$$T_2 = \frac{1}{4}\frac{1}{4C^2} = 8 \cdot 10^{-5} \tag{1.30}$$

We calculate the detection error according to figure 1.4 and get:

$$\epsilon = 0.5 - 1 \cdot 10^{-4} \tag{1.31}$$

It is very close to the highest possible error $\epsilon_{\max} = 0.5$, which occurs when the result of the measurement is guessed. This means that the two different atom numbers are (practically) indistinguishable.

For a lossless cavity, the detection error would still be $\epsilon = 0.5 - 9 \cdot 10^{-4}$, which means that not only the experimenter, but also the environment cannot infer the atom number in F=2.

We conclude that while it is not possible to infer how many atoms are in $F = 2$, our experimental setup is well suited to distinguish if at least one atom is in the state $F = 2$ or if all the atoms are in the $F = 1$ manifold without a spontaneous emission event. This allows us to perform a state detection measurement with an atomic ensemble in the quantum non-destructive (QND) regime. By that, we mean that no energy exchange occurs between the atoms and the probing light field [54]. The measurement is thus a projective measurement with two eigenvalues. It projects the atomic state either onto the state where all atoms are in $F = 1$ or onto the orthogonal subspace, containing all states with at least one atom in $F = 2$, since these are the only states the cavity can distinguish.

To illustrate the difference between a QND measurement and a measurement involving scattering, we consider an ensemble of N atoms inside the cavity. We assume the atoms

3. Details on the cavity can be found in section 2.2.

are in a symmetric state, with a single excitation in $F = 2$ being shared by all the atoms. In a non-QND measurement, an atom in $F = 2$ might scatter a photon. The atom's external state (i.e. its position in the trap) is therefore entangled with the emitted photon and revealed to the environment when the photon is detected by the surroundings. The atom in $F = 2$ thus becomes distinguishable and the symmetric state is destroyed. On the other hand, a measurement in the QND regime detects if an atom is in $F = 2$ without spontaneous emission of a photon, hereby preserving the symmetric state. We use this possibility of non-destructive detection of symmetric states to generate entanglement in an atomic ensemble (see chapter 4).

We now release the constraint of a QND measurement. In this case, we are limited by the hyperfine state dynamics of the atoms: Under the influence of the probe light, the atoms can scatter off-resonantly and fall into the respective other hyperfine state. Precisely, an atom in $F = 2$ can off-resonantly be excited to $F' = 1, 2$ from where it can relax into $F = 1$. On the other hand, an atom in $F = 1$ can be excited to $F' = 0, 1, 2$ with a possible decay to $F = 2$. Both processes change the number of atoms in $F = 2$, which we actually want to measure. Experimentally, a change from $F = 2$ to $F = 1$ ($F = 1$ to $F = 2$) can be observed as a sudden change in the cavity signal from low to high (high to low) transmission. We have experimentally inferred that the state of a single atom is changed from $F = 2$ to $F = 1$ ($F = 1$ to $F = 2$) after a mean number of $n_{\mathrm{sc},21} = 1 \cdot 10^4$ ($n_{\mathrm{sc},12} = 5 \cdot 10^3$) incoming photons [51]. We must therefore stay below this number in our state detection measurement. Sending $5 \cdot 10^3$ photons into the cavity leads to the mean transmissions $T_1 = 0.065$ and $T_2 = 0.016$. The corresponding detection error $\epsilon = 0.48$ still does not allow a precise atom number measurement.

1.4.3. Deviation from the ideal measurement and atom number scalability

We now discuss some deviations from the basic Tavis-Cummings model and analyze how they affect the state detection scheme. In particular, we study up to which atom number N we can use the cavity to infer the internal state of the atomic ensemble.

1.4.3.a. Current limitations

- **Atoms couple unequally to the light mode:**
  In (1.19), we have assumed that all atoms couple to the cavity mode with the same coupling strength g. This condition is perfectly realized if a BEC is placed in the cavity. In this case, all atoms are prepared in the same external macroscopic quantum state and thus all have the same spatial overlap with the cavity mode. A technical limit is therefore only reached when the dimensions of the BEC are on the same order as the cavity length.
  However, due to the way the atom number is prepared (see section 3.1 for details), the experiments presented in this thesis are performed with a thermal ensemble in the cavity. In this case, the atoms do not couple equally to the light field. The atomic cloud is trapped in one single antinode of the standing wave dipole trap mediated by the cavity. Due to the temperature distribution, atoms occupy different mean positions in the trap and therefore experience a different probe light

intensity. This leads to a different coupling constant g_i for each atom. By itself, this does not prevent the performance of a collective, QND measurement. However, it partially reveals the external state of the atomic ensemble, which defeats the purpose of a QND measurement: To infer only *if* an atom is in F=2, but not *which* one it is.

In the following, we estimate a maximum temperature of the atomic cloud that still allows for a state detection measurement in a symmetric way. We impose that two different atoms a and b in $F = 2$ should be indistinguishable by a cavity measurement to a degree of 90%. This means that the error ϵ_g of their discrimination measurement should be higher than 0.45. This error for two different mean transmissions T_a and T_b is given by the integral of their Poisson distributions $\mathrm{Pois}(T_a, k)$ and $\mathrm{Pois}(T_b, k)$ above or below the threshold (in this case, we use a threshold of 0 photons, cf. figure 1.4):

$$\begin{aligned} \epsilon_g &= \frac{\epsilon_{ab} + \epsilon_{ba}}{2} \\ &= \frac{\sum_{k=1}^{\infty} \mathrm{Pois(T_a, k)} + \mathrm{Pois(T_b, 0)}}{2} = 0.45 \end{aligned} \tag{1.32}$$

For a measurement with scattering probability $p_{\mathrm{sc}} = 0.2$, we obtain T_{a} from the numerical simulation (cf. figures 1.6 and 1.7):

$$T_a = 17 \cdot 10^{-4} \tag{1.33}$$

For ϵ_g to be above 0.45, T_2 must not be higher than

$$T_b = 0.1 \approx 60\, T_a \tag{1.34}$$

Such a high mean transmission is observed for a value of the coupling constant g_b as low as

$$g_b = \frac{1}{\sqrt[4]{60}} g_a \simeq \frac{1}{3} g_a \tag{1.35}$$

The atoms are held in a harmonic trap with a trap frequency $\omega = 2\pi \cdot 0.9 \cdot 10^6\,\mathrm{MHz}$ [4]. A coupling constant g_b is then reached for atoms with a potential energy which corresponds to a trap temperature $\Theta_{\mathrm{max}} = 5\,\mathrm{mK}$. The atomic ensembles prepared in our experiments are always much colder than this. We will find in section 4.4 that the cloud temperature is approximately 0.5 mK.

- **Hyperfine state dynamics:**
  As we have already pointed out, off-resonant scattering events can change the hyperfine state of the atom and thus the quantity that we want to measure. We now investigate how the probability for such a scattering event scales with the atom number N.
  From (1.27), we obtain that the scattering rate for atoms in $F = 2$ is independent of the atom number N. It is thus the scattering events $F = 1 \to F = 2$ that put a

4. This is the trap frequency of the dipole trap along the cavity axis for the light intensity chosen in the experiments.

constraint to the maximum atom number $N_{\max}$. We can give an estimate of $N_{\max}$, if we assume that the off-resonant scattering events of the individual atoms are not correlated. We have experimentally inferred that a single atom in the cavity performs a quantum jump $F = 1 \to F = 2$ after a mean number of $n_{\mathrm{sc},12} = 5 \cdot 10^3$ incident photons. For N atoms, the mean photon number $n^N_{\mathrm{sc},12}$ necessary for the occurrence of a quantum jump is thus inversely proportional to the number of atoms:

$$n^N_{\mathrm{sc},12} = \frac{n_{\mathrm{sc},12}}{N} \tag{1.36}$$

The state detection fails if $n^N_{\mathrm{sc},12}$ is on the same order as the number of probing photons n_{probe}. For a QND measurement with a detection error of approximately 10%, the number of probing photons is $n_{\mathrm{probe}} = 25$ (see figure 1.7). The state detection should therefore be possible for atom numbers up to

$$N = \frac{n_{\mathrm{sc},12}}{n_{\mathrm{probe}}} = 200 \tag{1.37}$$

For the experiments in this thesis, we limit ourselves to atom numbers $N < 100$.

1.4.3.b. Improvement of the limit

In future experimental setups, we can improve the maximal atom number N by customizing the properties of the cavity. We are ultimately limited by the atomic structure of the ^{87}Rb atom.

To maximize N, we have to keep the number of scattering events $F = 1 \to F = 2$ as low as possible. When an atom relaxes from the $5^2\mathrm{P}_{3/2}$ manifold, it falls into $F = 2$ with a probability $p \simeq 0.5$. The rate $\Gamma_{\mathrm{sc},12}$ for the event $F = 1 \to F = 2$ is therefore related to the scattering rate of an atom in $F = 1$ as

$$\Gamma_{\mathrm{sc},12} = \frac{1}{2}\Gamma_{\mathrm{sc}} \tag{1.38}$$

For atoms in $F = 1$, we have $\Delta_{ap} \gg g, \kappa, \gamma$. The rate $\Gamma^N_{\mathrm{sc},12}$ for N atoms therefore is (cf. (1.11)):

$$\begin{aligned}\Gamma^N_{\mathrm{sc},12} &= \frac{1}{2}\Gamma_{\mathrm{sc}} N = \frac{1}{2}\frac{g^2}{\Delta_{ap}^2}\frac{\eta^2}{\kappa^2}\gamma N \\ &= \frac{\eta^2}{\kappa}\gamma^2 C N = \frac{1}{\Delta_{ap}^2} n \gamma^2 C N\end{aligned} \tag{1.39}$$

This favors a cavity with low cooperativity C. On the other hand, a high cooperativity is needed to perform the measurement in the QND regime. We need a minimal number of $n = 5$ incident photons on average in order to infer the state of the ensemble with a detection error below 0.01. Furthermore, we impose a maximal mean number of scattering events of atoms in $F = 2$, $N_{\mathrm{sc,F=2}} = 0.1$. This fixes the cooperativity to be (cf. (1.17))

$$C = \frac{n}{N_{\mathrm{sc,F=2}}} = 50 \tag{1.40}$$

Putting this result in (1.39), we see that we can perform the state detection measurement with a maximal number of approximately 2000 atoms. The limitations stems from the finite detuning Δ_{HF} between the hyperfine ground states.

1.5. Conclusion

In this chapter, we have shown that our cavity is a convenient tool to infer the internal atomic state with low detection error. Since the atom-cavity system is deeply in the strong coupling regime, the measurement can also be performed with low probability for the occurrence of a scattering event.

If we consider an ensemble of N atoms in the cavity, this means that we can realize a collective state measurement in the QND regime. More precisely, we are able to detect whether all the atoms are in $F = 1$ or at least one atom is in $F = 2$. The detection error of the measurement is below 10% at a scattering probability of 20%. Due to off-resonant scattering, the maximum atom number is limited to $N < 200$.

2. The experimental setup

The following chapter is dedicated to the experimental setup, which combines an atom chip experiment with a miniaturized Fabry-Pérot cavity. This setup has been extensively described in [55, 56, 51] and we therefore only give a summary over the most important components.

In section 2.1, we describe the setup needed to produce a trapped cold atomic cloud on the atom chip. This comprises the vacuum apparatus, the optical setup and the atom chip.

In section 2.2, we introduce the fibre-based Fabry-Pérot cavity (FFP), describe how it is produced and mounted in the experimental setup and give its characteristics.

We conclude this chapter with a description of a typical experimental sequence, starting from a vapor at room temperature and ending with a BEC in the optical dipole trap of the cavity.

2.1. The setup for the production of cold atoms

2.1.1. The vacuum assembly and periphery

The use of an atom chip allows for a rather simple vacuum setup: The steep gradients of atom chip traps create higher atomic densities and therefore permit evaporative cooling on much faster timescales [57] than conventional setups with macroscopic magnetic coils. Experiments therefore can be performed under moderate vacuum conditions. Furthermore, the atom chip itself forms the top cover of the vacuum cell [58] and can hence be electrically connected from the outside. This disposes us from using accident-prone electrical feedthroughs.

For these reasons, the vacuum chamber only consists of a single glass cell which is provided on the outside with an anti-reflective dielectric coating [1], attached to an apparatus that maintains an ultra-high vacuum (UHV). The atom chip forms the top cover of the cell and the bottom is connected to a glass-metal transition [2]. A Rb dispenser [3] is placed in the duct of the glass-metal transition. It releases atomic Rb when heated via resistive heating and is electrically connected to a current source via an electric feedthrough.

The rest of the vaccum assembly consists of commercial components to create and maintain a UHV: The glass-metal transition is connected to a six-way cross. Also connected are a valve with an ion getter pump [4] and a Ti sublimation pump. A gauge allows to monitor the cell pressure and a window at the bottom gives optical access to the chip and the cavity region. Figure 2.1 shows the parts of vacuum assembly.

1. Hellma 704.001-OG
2. using the epoxy glue Epo-Tek 301
3. SAES RB-NF-3.4-12FT10+10
4. Meca2000 25L/s

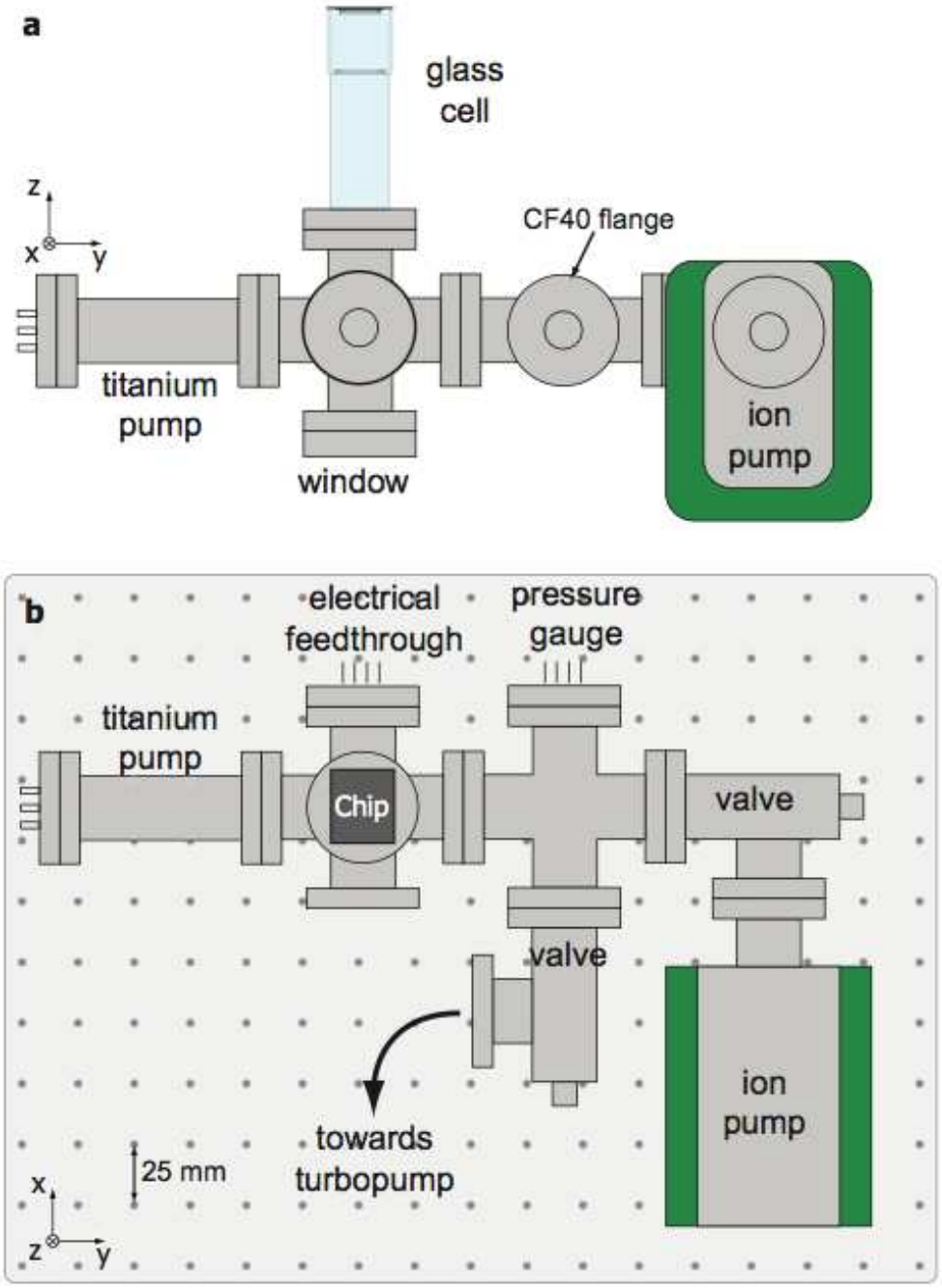

Figure 2.1.: Schematic of the vacuum assembly. a) side view b) top view. The vacuum assembly consists of the glass cell with the chip, attached to commercial UHV components. A six-way cross connects the glass cell to a Ti sublimation pump, an ion pump, an electrical feedthrough and a pressure gauge. An window gives optical access to the chip region. Adapted from [55]

The base pressure of the vacuum system is $3 \cdot 10^{-10}$ mbar. When the Rb dispenser is turned on, the pressure rises to approximately $1 \cdot 10^{-9}$ mbar.

A metal cage is placed around the glass cell. It holds three coil pairs in Helmholtz-configuration which provide magnetic bias fields in the three spatial directions and one pair in anti-Helmholtz-configuration which provides a field gradient for magnetic transport.

A microwave antenna is positioned at a distance of approx. 50 cm from the glass cell. It is connected to a homebuilt microwave generator and a series of amplifiers with a global gain of 51dB, providing a total output power of approx. 15 W. The system allows to drive Rabi oscillations between the two ground state levels $F = 1$ and $F = 2$ of ^{87}Rb, which are separated by approx 6.8 GHz.

2.1.2. The optical setup

The optical setup has five objectives. It generates the light necessary for the
- Cooling of the atoms in a magneto-optical trap (MOT) [5]
- Pumping of the atoms into a magnetically trappable Zeeman state
- Probing of the atoms (in an absorption imaging technique and in the cavity)
- Generation of a locking signal of the FFP cavity
- Generation of an optical dipole trap

In figure 2.2, the frequencies that are needed for these purposes are shown together with the level scheme of the D_2-line of ^{87}Rb.

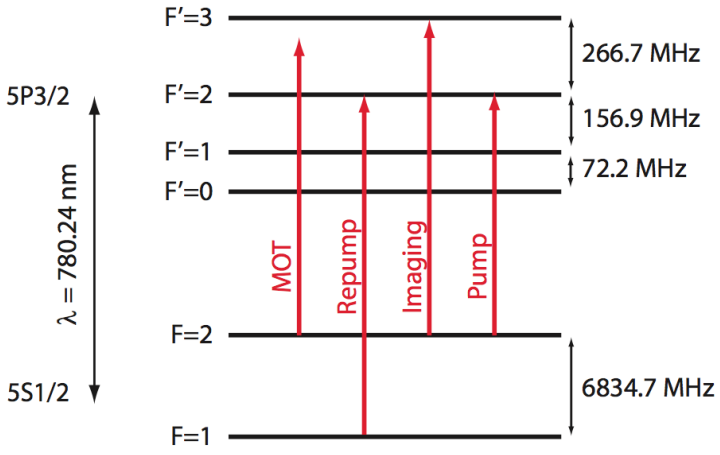

Figure 2.2.: Level scheme of the D_2-line of ^{87}Rb with the laser frequencies that are needed to cool and probe the atoms.

The light sources in our setup are laser diodes provided with an external cavity in form of a diffraction grating mounted in Littrow configuration [59]. They are frequency stabilized by feeding back an error signal to a piezo controlling the length of the external cavity. The error signal is created via frequency modulation Doppler free saturation spectroscopy [60, 61].

The optical setup is divided into four parts: The "main experimental" table, the "locking" table, the "detection" table and the optical setup surrounding the vacuum cell. In the following, they are described in detail:

The main experimental table contains a standard laser setup to produce a MOT and an optical molasses and to pump the atoms into a trappable Zeeman state. Furthermore, it generates the light used to probe the atoms via absorption imaging as well as in the cavity. Figure 2.3 shows a schematic of the beam paths. The table features four laser diodes:

- A "cooling" laser at 780 nm, locked to the $F = 2 \rightarrow F' = 2/F = 2 \rightarrow F' = 3$ crossover. A part of the light is branched off at a beam splitter and shifted by −264 MHz to the $F = 2 \rightarrow F' = 3$ transition using an acousto-optic modulator (AOM) mounted in a double pass configuration [62]. It is coupled into a polarization maintaining single mode (PMSM) fibre and sent to the vacuum chamber, where it serves to pump the atoms into the magnetically trappable $|F = 2, m_F = 2\rangle$ state. Another small part of the light is branched off and used to generate a beat lock signal with the probe laser.
- A "slave" laser at 780 nm, which provides the optical power necessary for the MOT stage. It is fed from the cooling laser, which is sent through a double pass AOM and shifted by 138 MHz before it is injected into the slave laser diode. The emitted light is thus at the same frequency as the injected light. Most of it is shifted again by −80 MHz in a single pass AOM and coupled into four PMSM fibres for the generation of the MOT. A small fraction is shifted by −106 MHz and coupled into two PMSM fibres for the detection via absorption imaging in x and y direction [5].
- A "repump" laser at 780 nm, locked to the $F = 1 \rightarrow F' = 1/F = 1 \rightarrow F' = 2$ crossover via Doppler free saturation spectroscopy. Its frequency is shifted by −83 MHz to the $F = 1 \rightarrow F' = 2$ transition by an AOM before the light is coupled into a PMSM fibre and sent to the vacuum chamber. There, it is used during the MOT phase to pump atoms that have fallen out of the cooling cycle back into the $F = 2$ state.
- A "probe" laser at 780 nm, which generates the light used to probe the cavity. To allow for a variety of different experimental configurations, we want this light either to be resonant to the $F = 1 \rightarrow F' = 2$ or the $F = 2 \rightarrow F' = 3$ transition. This is realized by a beat lock scheme, which either beats the probe light with light from the repump beam or from the cooling beam. The probe light can then still be shifted on the range of several hundred MHz in a double pass AOM. It is sent to the "locking" table through a PMSM fibre, where it is strongly attenuated by a single pass AOM before being sent to the detection table.

Except for the probe beam and a fraction of the cooling beam used for locking, all light from this table is fibre coupled and sent to the optical setup around the experimental chamber.

5. After having performed the experiments presented in this thesis, we have slightly modified the setup: Instead of using a master-slave configuration, we now deploy a tapered amplifier. This leads to an increase in the optical power for the MOT by a factor of 3 with respect to the configuration presented here. We therefore can reduce the MOT loading time from initially 6 s to 2 s.

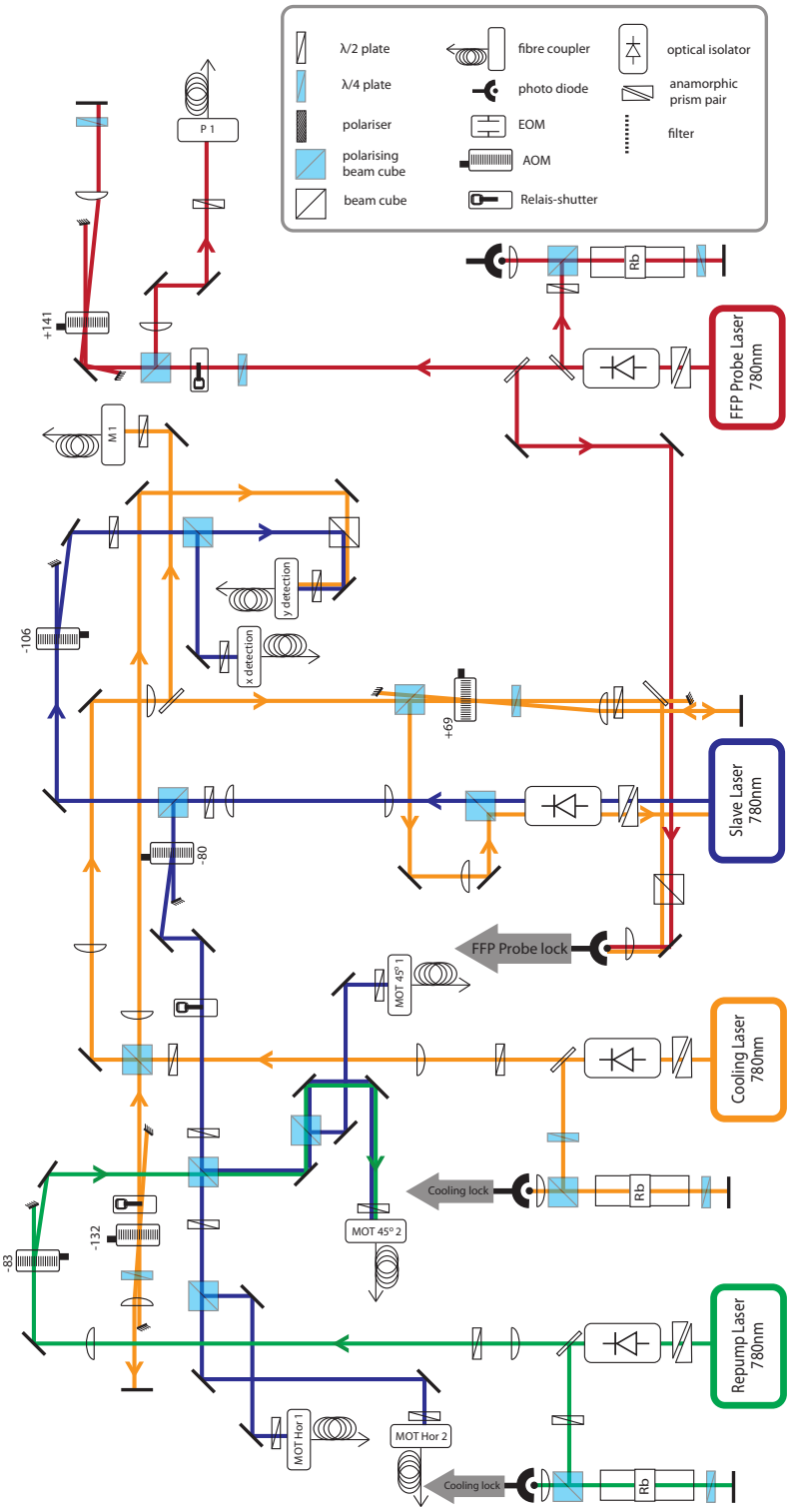

Figure 2.3.: Beam paths of the main table. The light mainly serves to generate a MOT and to pump the atoms into a magnetically trappable state. It is coupled into SMPM fibres and sent to the optical setup around the vacuum chamber (see figure 2.7). The light from the FFP probe laser is used to probe the atoms in the cavity and is sent to the "detection" table (see figure 2.5). The numbers next to the AOMs denote their frequency shift in MHz.

The locking table generates the light necessary to lock the FFP cavity and to generate an optical dipole trap inside it. It comprises a transfer cavity to ensure that the length of the FFP cavity is stabilized with respect to an atomic transition and that it can be frequency shifted independently from the probe light.

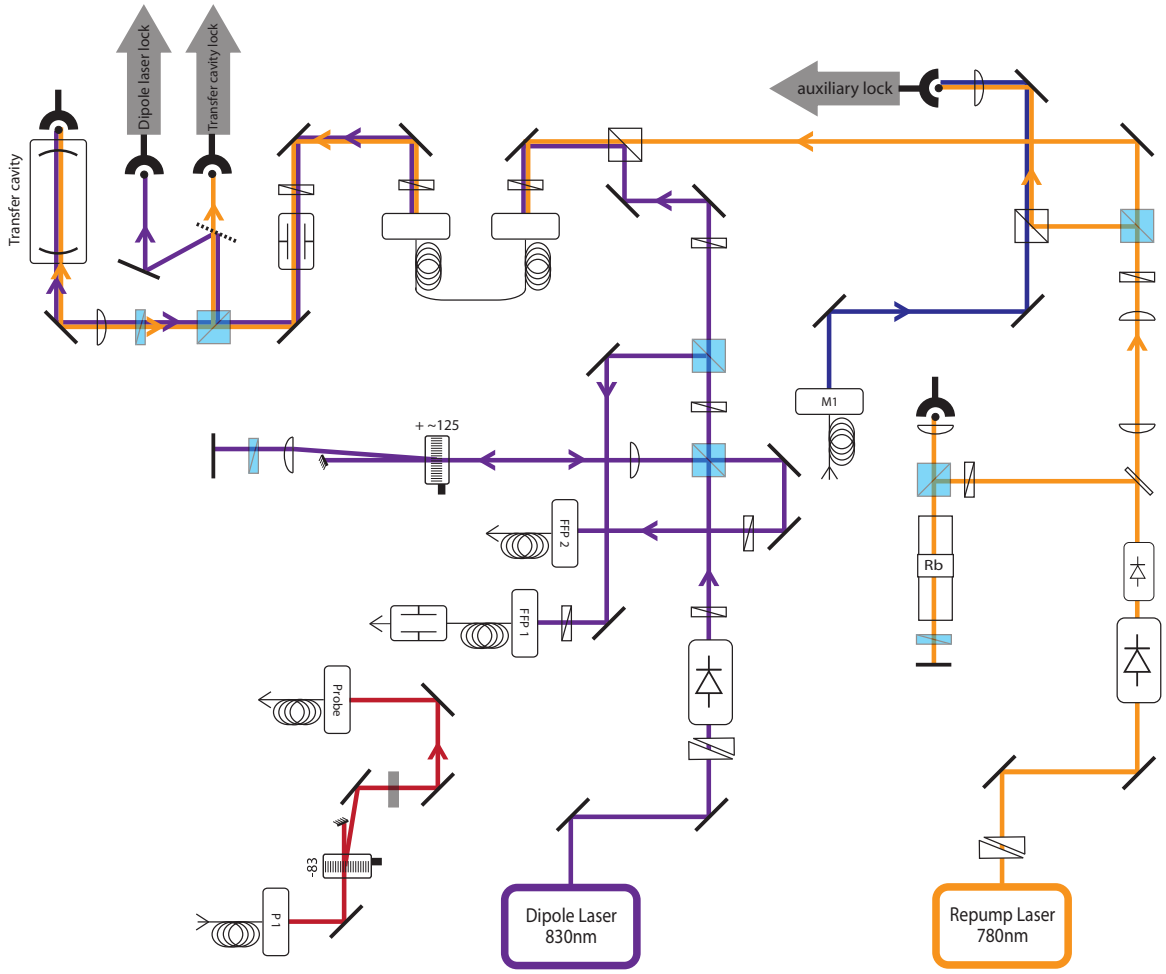

Figure 2.4.: Beam paths of the locking table. A legend of the symbols can be found in figure 2.3. The light from this table is coupled into SMPM fibres and sent to the detection table (see figure 2.5). The numbers next to the AOMs denote their frequency shift in MHz.

Figure 2.4 shows the optical paths on this table. It features two laser diodes.

– The "auxiliary" laser emits light at 780 nm and is locked in a beat lock scheme, obtained by superimposing it with a fraction of the cooling laser from the main table and detecting the beat signal with a photodiode (PD). The light is then sent through an electro-optic modulator (EOM) [6] and coupled into a macroscopic "transfer" cavity. The reflected light is sent onto a PD. A Pound-Drever-Hall (PDH) error signal [63] is generated from the signal of the PD and is fed to a piezo attached

6. Qubig High-Q EOM, modulated at 17.9 MHz

to a mirror of the transfer cavity. Hereby, the length of the transfer cavity is locked to the frequency of the auxiliary laser.

– The "FFP lock" laser emits light at 830nm. A part of it is superimposed with the auxiliary beam and also sent through the EOM and the transfer cavity. The reflected light is separated from the auxiliary beam by a reflective frequency filter [7] and sent on a PD. A PDH error signal is generated and fed back to the FFP lock laser. That way, the FFP lock frequency is stabilized with respect to an atomic transition, mediated by the auxiliary laser and the transfer cavity.
  The main part of the light is used to stabilize the length of the FFP cavity. It is frequency shifted in a double pass AOM by approx. 2·125 MHz and sent to the "detection" table through a fibre-coupled EOM [8]. The EOM modulates the light at a frequency of 1.8 GHz which is used to lock the FFP cavity in a PDH scheme.

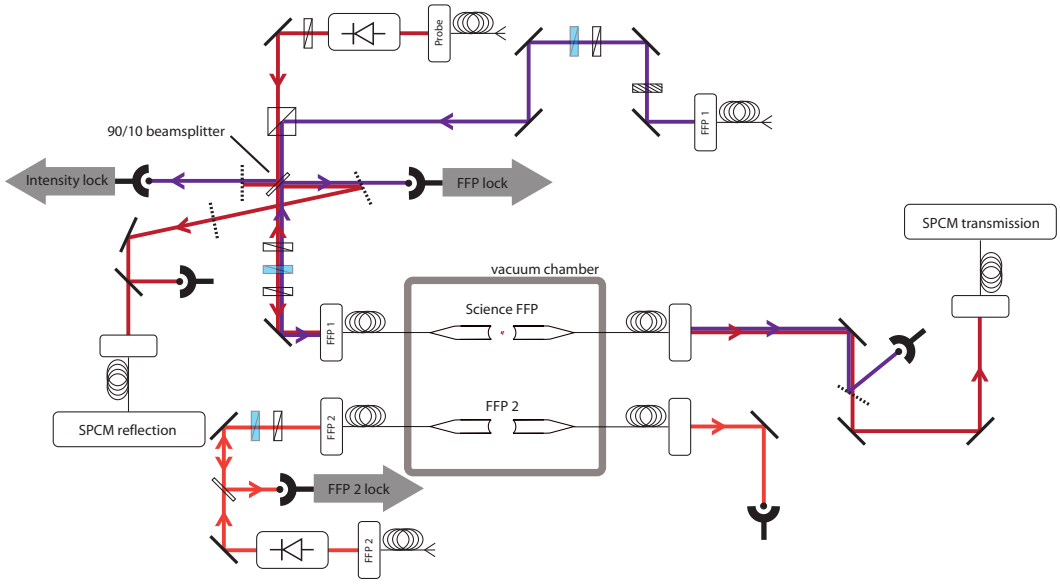

Figure 2.5.: Beam paths of the "detection table". A legend of the symbols can be found in figure 2.3.

The "detection" table (see figure 2.5) combines the probe light and the FFP lock light. Part of the latter is branched off and sent onto a PD. The voltage signal is compared to a set point and an error signal is generated, which regulates the amplitude of the AOM on the locking table and serves to stablize the intensity of the FFP lock light. A combination of $\lambda/2$- and $\lambda/4$-plates in the FFP lock beam path and the combined beam path ensure that the polarization of the two light fields can be adjusted independently. Afterwards the light is coupled into the input fibre of the FFP cavity.

The light reflected from the cavity is separated from the incoming light by a $^{90}/_{10}$

7. Semrock BL 786
8. Photline NIR-MPX800-LN-10

beam splitter and is split into its two frequency components. The FFP lock light is sent on a fast PD to generate the PDH error signal for the FFP cavity, while the probe signal is sent to a single photon counting module (SPCM). We also have the possibility to add a removable mirror in the beam path to monitor the reflected probe signal on a PD. In the same manner, the light transmitted by the FFP cavity is split into probe and FFP lock part. The latter is monitored on a PD, while the probe light is sent to a SPCM.

During the experimental sequence, we cannot always send light into the FFP cavity: When the magnetically trapped atoms are moved in between the two cavity fibres, The dipole trap light in the cavity has to be switched off in order not to degrade the cavity loading efficiency. The light is therefore blocked during 2 ms, which also removes the lock signal. To ensure that the cavity length meanwhile does not drift too far, an "artificial" error signal is applied during this time. This signal is generated from the second FFP cavity on the chip (FFP II): A part of the FFP lock light is branched off and sent to the FFP II cavity. The fibres of this cavity are aligned so that both the TEM00 and the TEM01 mode are excited. The reflected light intensity therefore contains the distinctive feature shown in figure 2.6. The light is collected on a PD and converted to a proportional voltage which directly serves as a error signal. This error signal is not only used to stabilize the length of the FFP II cavity but is also added to the error signal of the FFP cavity. During the 2 ms in which the FFP light is blocked, the change in cavity length is mainly due to thermal drifts which act on both cavities in the same way. The error signal of FFP II can therefore also compensate the length drifts of the FFP cavity.

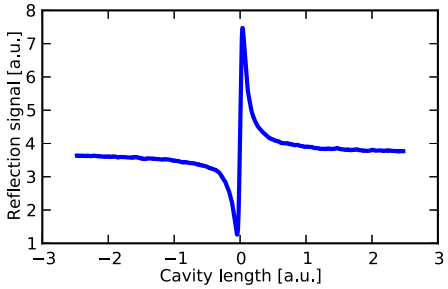

Figure 2.6.: The reflection signal of the FFP II cavity. Since the TEM00 and the TEM01 mode are both excited, the reflection features a zero crossing at resonance, which can be used as a lock signal.

The optical setup surrounding the vacuum cell disposes the light generated on the main table and coupled into PMSM fibres.

The MOT light is expanded to a beam diameter of 2.54 cm and sent onto the experimental chamber in a "mirror MOT" configuration [64, 65, 66]. This means that the three pairs of counter propagating beams necessary for a MOT are generated with the help of the surface of the atom chip, which is provided with a dielectric coating and acts as a mirror. Thereby, two beams can be omitted and the MOT conditions are satisfied in a spatial region below the chip by sending only four light beams into the glass cell.

Two detection beams are also sent onto the vacuum cell. The first one - referred to as

"y detection" beam - is superimposed with the horizontal MOT beam by a polarizing beam cube and illuminates the chip area where the MOT is generated. The second one - referred to as "x detection" beam - illuminates the cavity region. Two cameras[9] are positioned in the beam path behind the experimental chamber and allow for absorption imaging of the cold atoms during different stages in the sequence.

Furthermore, the light dedicated to the excitation of intracavity atoms from the side enters the experimental chamber from the bottom glass port and is focused on the cavity region.

Figure 2.7 shows a schematic of the optics surrounding the glass chamber.

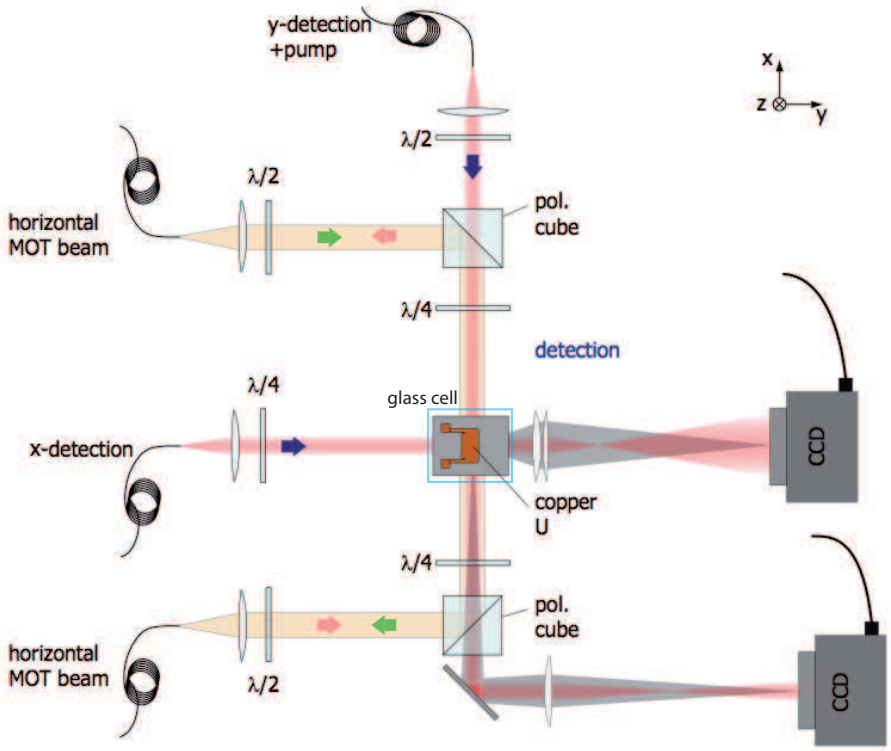

Figure 2.7.: Schematic of the optical setup surrounding the glass cell (top view). Two of the four MOT beams are shown. The other two beams hit the chip under an angle of 45° and are reflected by the chip surface to create a mirror-MOT. The two detection beams allow to make absorption images of the atomic cloud in the MOT region (y-detection) and in the cavity region (x-detection). Adapted from [55].

2.1.3. The atom chip

Atoms have to be confined so that they can be studied and manipulated. The interaction energy of a neutral atom in a magnetic field is

$$E(B) = g_F m_F \mu_B |B| \tag{2.1}$$

9. JAI CV-M50-IR

where m_F is the magnetic quantum number, g_F the Landé g-factor and μ_B the Bohr magneton. A position dependent B-field thus creates a position dependent potential for the atom. Dependent on the sign of $g_F m_F$, the atom is either attracted towards minima ($g_F m_F > 0$, "low-field seeking states") or maxima ($g_F m_F < 0$, "high-field seeking states") of the magnetic field.

Since the Maxwell-equations forbid field maxima in free space, only low-field seeking states can be magnetically trapped. Conventional magnetic traps provide a minimum of the magnetic field by using macroscopic current-carrying coils, typically placed several centimeters away from the atoms. The steepness of the trap is proportional to $\delta B/\delta r$ and therefore scales with $1/r^2$, which makes it desirable to reduce the distance between the trap and the conductor.

The atom chip, first proposed in 1995 [67] reduces this distance by orders of magnitude: Currents run through planar wire structures on a surface and create magnetic fields with strong gradients. Atoms can be trapped at a close distance (typically tens of µm) from the surface.

The higher field gradients compared to conventional, macroscopic traps create a tighter confinement which leads to a higher density of the atoms. This strongly improves the efficiency of evaporative cooling techniques: While the time for BEC condensation in conventional traps typically is on the order of tens of seconds, it is only around 1s for magnetic traps created by an atom chip [57].

The conducting structures are printed on the substrate using photolithography. This method allows the fabrication of two-dimensional structures with very complex shape, which enables the generation of a variety of different trapping potentials.

Furthermore, the fact that an atomic sample can be trapped in direct vicinity of a surface makes the atom chip a versatile tool to study interactions between cold atoms and surfaces [68, 69, 70] or to combine cold atoms with solid states systems such as mechanical resonators [71] or in our case - a miniature Fabry-Pérot cavity.

2.1.3.a. The principle

In the following, we illustrate the working principle of atom chip traps and introduce the trap configurations that are used on the chip in our experiment.

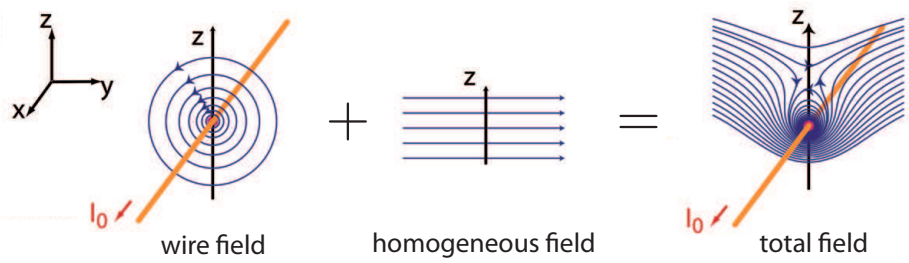

Figure 2.8.: The magnetic field of an infinitely thin wire (left), combined with a homogeneous field (middle) creates a field with a minimum parallel to the wire which can serve to confine atoms in two dimensions (right). Adapted from [72].

The wire guide The B-field of an infinitely thin wire, oriented along $\hat{e}_x$ and carrying a current I_0, is expressed by the law of Biot-Savart:

$$B(z) = \frac{\mu_0}{2\pi}\frac{I_0}{z} \tag{2.2}$$

It is sufficient to add a homogeneous magnetic field $B_{b,y}$ perpendicular to the wire in order to create a two-dimensional confinement (see figure 2.8). The magnetic field then is zero along a line parallel to the wire at a distance z_0, given by

$$z_0 = \frac{\mu_0}{2\pi}\frac{I_0}{B_{b,y}} \tag{2.3}$$

Around this field minimum, the total field can be approximated by a two-dimensional quadrupole with gradient

$$\frac{\partial B}{\partial z}(z_0) = -\frac{2\pi}{\mu_0}\frac{B_{b,y}}{I_0} \tag{2.4}$$

This configuration is known as "wire guide" configuration [72].

The dimple trap The wire guide can be extended to provide three dimensional confinement by adding a second, perpendicular wire. If the current I_1 through this additional wire is sufficiently small, the field minimum is still given by Eq. 2.3. The configuration can then be seen as the overlap of two two-dimensional traps. A quadratic field minimum forms at the crossing of the two wires (see figure 2.9). This configuration is referred to as a "dimple trap".

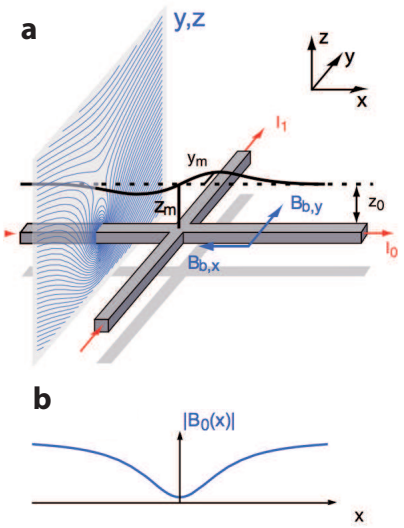

Figure 2.9.: The dimple trap. The wire guide formed by I_0 and a homogeneous field $B_{b,y}$ is combined with the field from the current through a second wire I_1, which provides axial confinement. Above the wire intersection, a quadratic field minimum forms in all three dimensions. a) Wires and magnetic field in the y,z plane; b) absolute value of the magnetic field along x. Adapted from [72].

The "H" and "Z" trap An alternative three-dimensional trap with larger trapping volume can be generated using three wires. We consider the wire configuration shown in figure 2.10a). The direction of the currents in the wires perpendicular to the wire guide is reversed with respect to the dimple trap. Above the wire crossing, at a distance $z = z_0$, the B-field in direction $\hat{e}_x$ therefore has a field maximum while the confinement in $\hat{e}_y$ remains. Two such crossings hence form an elongated three-dimensional trap. In the case of $I_1 = I_2$, this wire configuration can be further simplified: The z-shaped wire shown in figure 2.10c) essentially generates the same trapping field.

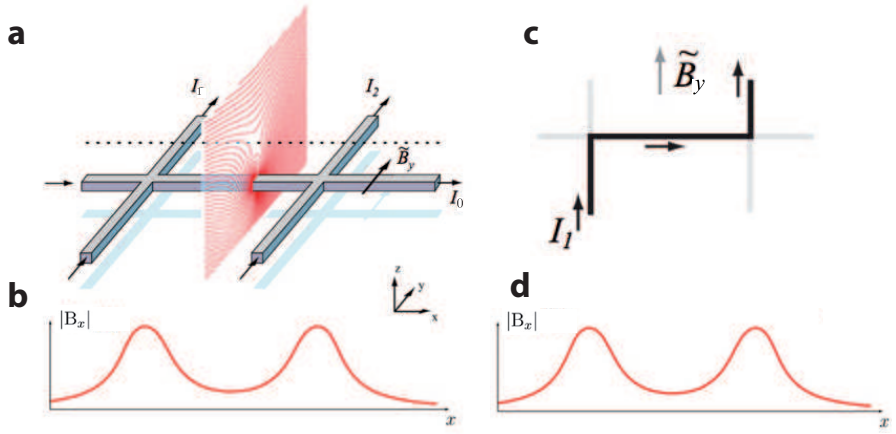

Figure 2.10.: The H and Z trap. a) The H trap is formed by a wire guide and two perpendicular wires. The currents I_1, I_2 have opposite sign with respect to I_1 in the dimple trap. b) absolute value of the magnetic field along x. c) In the case $I_1 = I_2$, the Z trap is equivalent to the H trap. d) The Z trap has the same absolute value of the magnetic field along x. Adapted from [73].

2.1.3.b. The atom chip of the FFP experiment

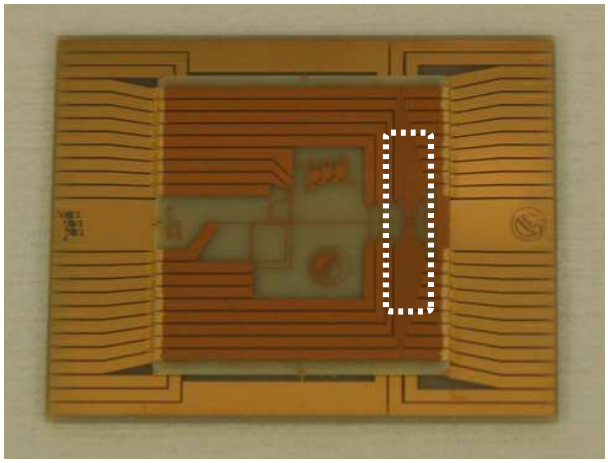

Figure 2.11.: A photo of the atom chip used in the experiment. It consists of two chips made of Aluminium Nitride that are glued together. The wires on the chip substrates are made of gold and are grown on the substrate by galvanic deposition. The two chips are electrically connected by bond wires. In this image, the fibre cavity is not yet glued to the chip. Its later position is indicated by the dotted line.

Figure 2.11 shows a picture of the atom chip used in our experiment. It is specially designed to generate a cold sample of atoms and to move it precisely in between the two fibres of the miniature cavity. A support holding the cavity fibres will be glued onto the chip surface at the position is indicated by the dotted line.

Design and vacuum assembly The chip actually consists of two atom chips glued together with thermally conductive, electrically isolating glue [10]. Both chips are made of AlN. The conducting structures are made of Au and are lithographically patterned on the chips [11]. The bigger "base" chip on the bottom has the dimensions 35 mm × 45 mm × 0.8 mm and contains wire structures with a width of about 0.2 to 1 mm and a thickness of 7 µm. The smaller chip or "Science chip" has the dimensions 28 mm × 26 mm × 0.63 mm and contains wire structures as small as 50 µm in width and 7 µm in height. The top of the science chip is covered with a dielectric "transfer" coating [55] which is highly reflective at 780nm [12]. This enables cooling and trapping of the atoms in a mirror-MOT configuration. The design of the science chip is shown in figure 2.16.

The atom chip is glued on the top of the open glass cell. While the science chip is completely immersed in the cell, the base chip protrudes the top area of the cell, hereby forming the upper lid of the vacuum chamber. This makes the base chip easily accessible from the outside. For electrical connection of the chip wires, we use a commercial "Mini

10. Epo-Tek H77

11. For a detailed description of the fabrication process, see [74, 75]. For a possible future setup, we fabricated an atom chip with the same design as used in the experiment. Its fabrication protocol can be found in appendix A.

12. from OIB Jena, glued with Epo-Tek 353ND

PCI" connector which is clamped to the two protruding parts of the base chip (see figure 2.12). The wires on base and science chip are electrically connected through bonding wires (14 Au bonding wires with a diameter of ∅ = 25 µm per connection). The cavity fibres and the electric connections of the piezo actuators for the cavity (see section 2.2) are fed into the chamber through small kerfs in the glass cell, which are sealed with epoxy glue [13].

The upper surface of the atom chip is directly accessible from the outside. We use this access to attach a macroscopic "U"-shaped copper piece to the chip. In the first part of the experimental sequence, we send 57.2 A through this piece to create the magnetic quadupole field for the MOT. To dissipate the resistive heat of the copper "U" as well as of the chip wires, the copper "U" and a thermistor are immersed in a copper block which is glued to a Peltier element. The hot side of this element is attached to a water cooled copper block. This system enables us to actively stabilize the chip temperature.

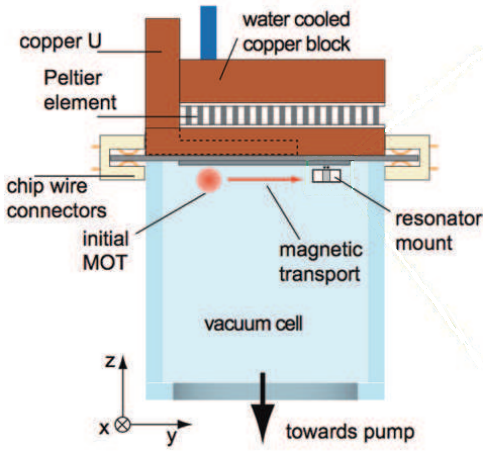

Figure 2.12.: A schematic of the chip as the top of the glass cell. It is electrically connected by two commercial PCI connectors. A U-shaped copper piece is glued on the outside of the chip to create the magnetic quadrupole field for the MOT stage. On top of it, there is a Peltier element and a water cooled copper block, which enable active stabilization of the chip temperature. Also indicated are the positions of the inital MOT and the cavity fibre mount. Adapted from [55].

2.2. The Fibre Fabry-Pérot cavity

The heart of the experimental setup consists of a fibre-based Fabry-Pérot (FFP) cavity. It is a miniaturized cavity, which consists of the highly reflective end facets of two optical fibres. Such a cavity has some advantages compared to cavities consisting of macroscopic mirrors (as e.g. used in [76, 14, 77, 78]):

- The mirror surfaces have a very small diameter. Therefore they can be brought very closely together even if they have a big radius of curvature. This leads to a very small cavity mode volume.
- Because of its small dimensions, the cavity can be brought very close to the chip

13. Epo-Tek 301

surface where the high magnetic gradients can strongly confine the trapped atomic cloud and can spatially control it with high precision. We can therefore load all the atoms of a magnetically trapped cloud into one single antinode of the intra-cavity standing wave dipole trap [23].

In the following, the fabrication and implementation of an FFP cavity in our setup are described. We then summarize its physical properties.

2.2.1. Fabrication and experimental implementation

Fabrication FFP cavities can be produced from any sort of glass fibre, independent of its waist, light guiding properties (wavelength, polarization maintaining, single mode/multimode) or cladding material.

In a first step, the cleaved fibre end facets are provided with a concave structure. This is done by shooting onto them with a focused CO_2 laser beam. Hereby, some part of the glass in the fibre is evaporated and some part is melted, which leads to a concave structure with a very low surface roughness ($\sigma_{sr} = 0.2(1)\,\mathrm{nm}$). Depending on the used light power, the pulse length and the beam waist of the CO_2 laser, radii of curvature down to 50 µm can be produced [79]. Figure 2.13 shows the end facet of a fibre after such a CO_2 laser fabrication process.

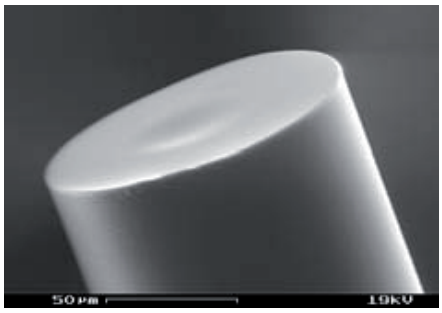

Figure 2.13.: An electron microscope image of an optical fibre after CO_2 processing. The tip features a well-centered concave structure. The fibre has a diameter of 125 µm.

The fibre tip is then provided with a highly reflective coating through an ion beam sputtering process [14]. The absorptive and reflective properties of the coating can be designed to meet the experimental requirements.

Experimental implementation Due to its small size, the alignment and fixation of the fibres is a very delicate process. The fibres are mounted in such a way that - except for the cavity length - the cavity alignment is fixed.

The support of the cavity consists of a Macor ceramic bridge. To be able to shift the cavity length (by approx. 1 µm in total), piezo shear actuators are glued on the bridge. The stripped fibres (⌀ = 125 µm) are glued into silicon V-groove substrates, which are glued onto the shear piezos with slow-curing epoxy glue [15]. During the curing

14. performed e.g. at the Laserzentrum Hannover
15. Epo-Tek 301

process, which takes several days, the cavity transmission is monitored and the fibres are constantly realigned.

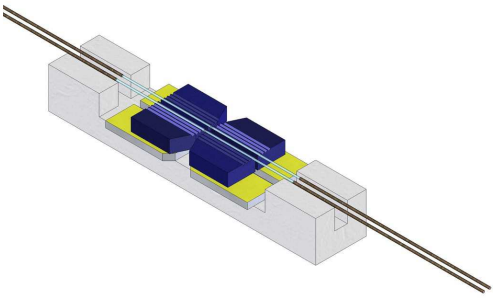

Figure 2.14.: A schematic of the bridge assembly. The stripped glass fibres are glued into commercial V-groove substrates (dark blue), which are fixed on shear piezo acutators (yellow/dark grey). The ensemble is held by a Macor bridge (light grey), which is glued onto the chip surface. (Image by Konstantin Ott)

Figure 2.14 shows the supporting bridge with the glued cavity. We actually have two cavities glued in the V-grooves, of which only one is used for the experiments (FFP cavity) while the second one serves for locking purposes (FFP II, see section 2.1.2). To simplify the alignment procedure, the cavities consist of one single mode fibre and one multimode fibre. A hole in the middle of the Macor bridge allows optical access to the cavity region.

The whole bridge assembly is then positioned above the specified chip location and fixed on the chip with UV glue. The thickness of the bridge is designed so that the distance between the fibres and the chip surface is 90 µm. The optical mode of the cavity is therefore positioned approx. 150 µm above the chip surface. Figure 2.15 shows the bridge with the cavities glued to the atom chip.

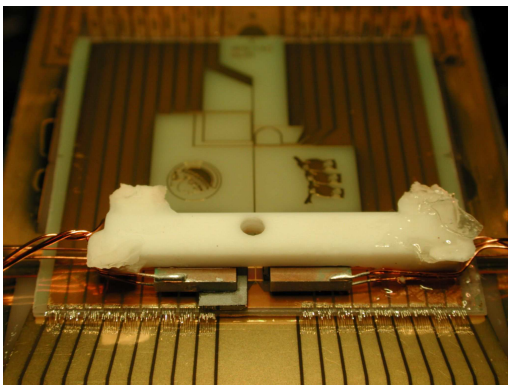

Figure 2.15.: A picture of the Macor bridge glued on the atom chip. It is fixed with UV-glue so that the cavity fibres are placed above a wire crossing. For positioning, the bridge was glued to a translational stage. Transparent residuals of the glue are visible on top of the bridge.

2.2.2. Characteristics

The cavity used in our setup consists of a single mode fibre with a radius of curvature $r_1 = 450\,\mu m$ and a multi mode fibre with radius of curvature $r_2 = 150\,\mu m$. They are brought closely together to form a cavity of length $l = 38.6\,\mu m$. At 780 nm, the cavity mode waist therefore amounts to

$$w_0 = \left(\frac{\lambda}{\pi} \left[\frac{l(r_1 - l)(r_2 - l)(r_1 + r_2 - l)}{(r_1 + r_2 - 2l)^2} \right]^{\frac{1}{2}} \right)^{\frac{1}{2}} = 3.9\,\mu m \tag{2.5}$$

and the cavity mode volume is

$$V_m = \frac{\pi w_0^2 l}{4} = 461\,\mu m^3 \tag{2.6}$$

The maximum coupling g_m^{theory} can be obtained from (1.3) by choosing the maximal dipole matrix element $d_{22\to33} = 2.53 \cdot 10^{-29}\,Cm$ from the $|F = 2, m_F = 2\rangle \to |F' = 3, m_{F'} = 3\rangle$ transition:

$$g_m^{\text{theory}} = 2\pi \cdot 214\,MHz \tag{2.7}$$

In addition, the coupling has also been determined experimentally [51] to be

$$g_m = 2\pi \cdot (240 \pm 10) MHz \tag{2.8}$$

We will use this value in the calculations of this thesis, since the radii of curvature, which are on the basis of g_m^{theory}, are not known with sufficient precision.

The coating company specifies the losses and transmission of the dielectric coating to be $\mathcal{L}$ =56 ppm and $\mathcal{T}$ =31 ppm. The measured value of the finesse $F = 36600$ corresponds well to these values.

The cavity mirrors feature birefringence: photons of orthogonal linear polarization accumulate a phase difference when reflected on the mirror. This leads to two different cavity resonance frequencies for two orthogonal linear polarizations which in our case are spaced by $\Delta\omega = 2\pi \cdot 504\,MHz \approx 10 \cdot \kappa$. This restricts the way in which we can probe atoms in the cavity: We can only send linearly polarized light into one of the cavity resonances which corresponds to either π-polarized light or σ^+/σ^--polarized light in the atomic frame.

However, there are still many different possible configurations for polarization and detuning of the probe and dipole light. Our choice and its influence on the photon number in the cavity and the population in the excited atomic states are presented in section 1.3.

The dipole trap The cavity not only has to be resonant to the probe light at 780nm, but also to the FFP lock light at 830nm. This light serves both to create a standing wave dipole trap and to lock the cavity length. To maximize the coupling g between the atoms and the cavity mode, the cavity length is chosen so that both frequencies have an odd number of antinodes in the cavity and the atoms are trapped exclusively in the middle antinode of the dipole trap.

2.3. A typical experimental sequence

The experiment is controlled by three PCI-boards [16] with analog and digital outputs. A computer program controls these outputs and runs a predefined static protocol. We usually use such a protocol to create a cold atomic cloud and to load it into the optical dipole trap.

In order to react in real time on experimental results, we have a second control system: a real-time controller [17] with analog and digital in- and outputs can be activated at times during the sequence when feedback on experimental events is required. We usually use the real-time controller system at an experimental stage where a cold cloud of atoms is inside the cavity. The real-time controller then changes the further course of the sequence according to the outcome of transmission and reflection measurements of the SPCMs.

In the following, we quickly summarize the first, static part of the experimental sequence until the atoms are placed in the optical dipole trap. This then is the starting point of the sequence part that is controlled by the real-time controller. All experiments in this thesis (see chapters 3, 4 and 6) are described from that point onwards. Figure 2.16 shows the science chip and gives the names of important wires referred to in the text. A detailed description of the experimental sequence is given in [51].

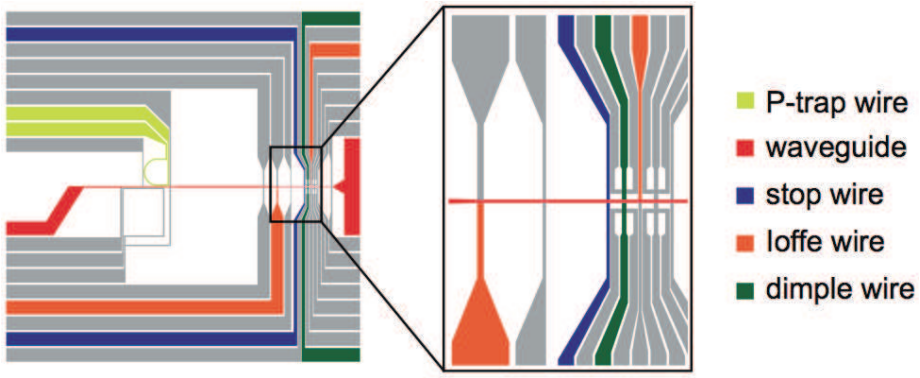

Figure 2.16.: The wire configuration of the science chip. Important wires for the sequence are marked in color and named. The inset shows a zoom on the cavity region. Adapted from [51].

First, we trap a cloud of approximately $1.2 \cdot 10^7$ atoms in a MOT. The magnetic quadrupole field for this MOT is generated by the copper U wire above the atom chip and an external bias field.

The atoms are then loaded into a MOT whose magnetic quadrupole field is generated by a U wire on the base chip.

The MOT is then compressed and brought closer to the chip surface. After a short phase of optical molasses (3 ms), where the atoms are cooled down to a temperature of approximately 70 µK, they are pumped into the $|F = 2, m_F = 2\rangle$ state and trapped in a magnetic trap created by the P-trap wire and an external bias field.

16. National Instruments PCI-3360 and PCI-4820
17. Jaeger Electronics ADWin light

By changing the orientation of the magnetic bias field, the spatial orientation of the trapped cloud is changed [80] until its longitudinal axis coincides with the orientation of the waveguide wire.

The cloud is then transported from the P-trap along the waveguide towards the cavity region (see the inset of figure 2.16) by moving the zero point of the external quadrupole field. At this stage, the atomic cloud is too hot and too large to fit between the cavity fibres. The cloud is therefore kept from colliding with the fibres by the potential of a stop wire. The atoms are trapped in a Z-type trap formed by Ioffe- and stop wire. By increasing the the magnetic bias fields, the cloud is compressed. At the same time, current is sent through the dimple wire, which creates a dimple trap (cf. figure 2.9) at the position between the cavity fibres.

The barrier created by the stop wire is then ramped down and a radio frequency ramp is applied during 500 ms to evaporatively cool the atoms and trap them inside the dimple trap.

In a next, optional step, the magnetic bias fields can be changed so that the position of the dimple trap is shifted close to one of the cavity fibres, where the hottest atoms stick to the fibre surface. This step of surface evaporation can be used to condense the atoms into a BEC or to just reduce the atom number, in case we want to perform experiments with a small atomic ensemble.

Finally, the magnetic trap is moved to the exact center of the cavity mode. The magnetic fields are slowly ramped down while the dipole trap light is slowly ramped up and the atomic cloud is adiabatically transferred from a magnetic trap to the optical dipole trap.

The experimental cycle time is approximately 8 s, including 6 s of MOT loading time [18].

18. The experiments described in this thesis have been conducted before the tapered amplifier was installed on the optical table. With the tapered amplifier, the total cycle time is reduced to 3 s, with a MOT loading time of 2 s.

3. Atom number preparation and counting in the dispersive regime

In this chapter, we present a method to prepare mesoscopic ensembles of well-defined atom number in the cavity. A fixed atom number is a prerequisite for many experimental tasks including quantum tomography, where many identical samples of a quantum state must be produced. The standard approach consists in preparing a certain atom number by evaporative cooling. In our case, this technique is far from single atom resolution, because of the statistical nature of the temperature distribution and fluctuations of the trap bottom due to fluctuations of the magnetic field. We therefore choose a different approach, which makes use of the cavity: A measurement of the transmitted or reflected light intensity can infer the number of atoms, since non-resonant atoms shift the cavity resonance. We first calculate the expected signal-to-noise ratio (SNR) of such an atom number counting measurement before we use this method to not only count, but prepare a fixed atom number in the cavity. The method presented here will also be used in chapter 4 to prepare the initial state for the generation of multiparticle entanglement.

The second part of this chapter is dedicated to an attempt to count the atom number in the QND regime, i.e. without any energy exchange between the probing light field and the atomic ensemble. We investigate a method of atom number counting based on a measurement of the phase of the cavity light field and compare its performance to the atom number counting scheme via intensity measurement. We will find that both methods yield the same measurement precision in terms of scattered photons. Finally, we perform an experimental realization of a phase measurement at low light powers using a single photon counting module (SPCM) and present preliminary results.

3.1. Preparation of a fixed atom number in the cavity

3.1.1. Counting atoms in an intensity measurement

In the following, we calculate how accurately we can infer the atom number in a measurement of the cavity transmission or reflection. We also analyze the result in terms of scattered photons.

If we place atoms in our cavity resonant to an atomic transition, the intracavity intensity I_I and the transmitted intensity I_T are reduced by $1/4C^2$. As we have shown in chapter 1, the transmission drop caused by one resonant atom is sufficient to completely block the cavity transmission. All the incoming light is then reflected and we cannot determine the atom number in the cavity. If the atomic transition is however far detuned from the cavity transition ($\Delta_{ap} \gg \frac{g^2}{\kappa}$), an atom only acts as a refractive index on the photons entering the cavity, effectively shifting the cavity resonance by an amount

$\Delta_{cp}^{\mathrm{at}} = \frac{g^2}{\Delta_{ap}}$. This effect is proportional to the number of atoms N:

$$\Delta_{cp}^{\mathrm{N\,atoms}} = N\frac{g^2}{\Delta_{ap}}. \tag{3.1}$$

This changes the cavity transmission and reflection intensity, hereby allowing to determine the atom number in the cavity within a detuning range of $\pm 2\kappa$.

In the following, we apply the experimental parameters of our atom cavity system and consider the case of atoms in the hyperfine state $F = 1$ and the cavity as well as the probe light resonant to the $F = 2 \rightarrow F' = 3$ transition (see figure 3.1). The light is detuned by $\Delta_{ap} = 2\pi \cdot 6.8\,\mathrm{GHz}$, which is much larger than the hyperfine structure in the excited state. This means that in order to compute the frequency shift induced by the atoms, all the possible transitions $F = 1 \rightarrow F' = 0, 1, 2$ have to be taken into account. The coupling constants add up to $g_1 = \sqrt{\frac{2}{3}} g_{22\rightarrow 33}^{\sigma^+} = 2\pi{\cdot}195\,\mathrm{MHz}$ [56]. With $\kappa = 2\pi{\cdot}53\,\mathrm{MHz}$, the detuning caused by one atom is $\Delta_{cp}^{\mathrm{at}} = 2\pi{\cdot}5.6\,\mathrm{MHz}$.

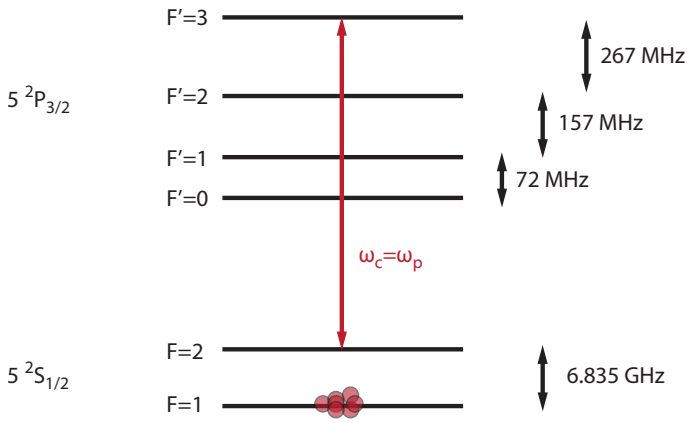

Figure 3.1.: The level scheme of ^{87}Rb and the experimental configuration considered for the measurement of the atom number in the dispersive regime. The atoms are placed in $F = 1$, while the probe light and the cavity are resonant to the $F = 2 \rightarrow F' = 3$ transition.

This configuration has two experimental advantages: Firstly, the shift of one atom is convenient to measure atom numbers of approximately 10 atoms in the cavity, which suits well our ambitions to create entangled states consisting of mesoscopic atom numbers. Secondly, putting the cavity resonant to the $F = 2 \rightarrow F' = 3$ transition allows us to observe quantum jumps between the hyperfine ground states: If an atom jumps to $F = 2$, the transmission signal drops to zero. We can therefore assume that if we observe a signal, all atoms are in $F = 1$ and every atom shifts the cavity by the same amount. Figure 3.2 shows the expected shift in transmission due to different atom numbers for our cavity parameters.

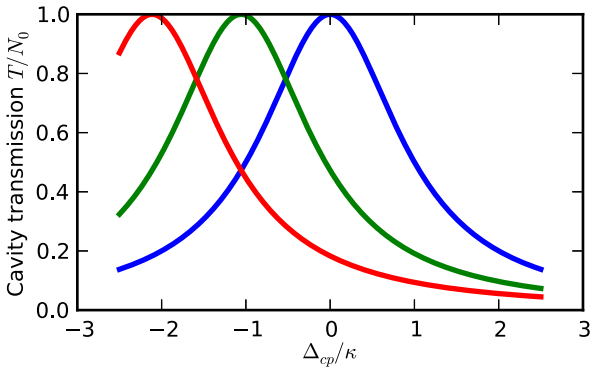

Figure 3.2.: The cavity transmission as a function of the effective cavity probe detuning $\Delta_{cp} = \omega_c - \omega_p$, caused by 0, 10 and 20 atoms in the cavity (blue, green and red, respectively.). The atoms are far detuned from the cavity resonance ($\Delta_{ap} = 2\pi{\cdot}6.8\,\mathrm{GHz}$) and maximally coupled to the cavity mode ($g_1 = 2\pi{\cdot}195\,\mathrm{MHz}$).

For $\Delta_{ap} \gg \frac{g^2}{\kappa}$, the cavity transmission in terms of photons T is given by (cf. (1.12)):

$$T = \frac{\alpha^2 N_0}{\Delta_{cp}^2 + \kappa^2} \tag{3.2}$$

with N_0 being the number of incoming photons and $\alpha = \frac{\mathcal{T}}{\mathcal{T}+\mathcal{L}}$ being the transmission factor of the cavity [1].

The relevant signal for distinguishing different atom numbers is the change in the number of transmitted photons induced by one atom:

$$\frac{\partial T}{\partial \Delta_{ca}} \Delta_{cp}^{\mathrm{at}} \tag{3.3}$$

In this measurement, the accuracy is fundamentally limited by the shot noise of the transmitted photons $\sqrt{N_T}$. The SNR of this method therefore amounts to

$$\mathrm{SNR} = \frac{2\alpha\kappa\Delta_{cp}}{(\Delta_{cp}^2 + \kappa^2)^{\frac{3}{2}}} \sqrt{N_0}\, \Delta_{cp}^{\mathrm{at}} \tag{3.4}$$

The SNR in reflection can be calculated accordingly. Figure 3.3 shows the SNR of a transmission and reflection measurement for an ideal (i.e lossless, $\alpha = 1$) cavity. We see that only for $\Delta_{cp} = \kappa$, the information is equally distributed between the transmitted and reflected signal.

In reflection, the highest information can be obtained at resonance: Since the intensity is zero, the shot noise is minimal and the SNR maximal at this detuning. It is $\frac{3}{2}\sqrt{3}$ times higher than the maximal SNR in transmission.

1. Our FFP cavity has a transmittance of $\mathcal{T} = 31$ ppm and losses of $\mathcal{L} = 56$ ppm and a corresponding transmission factor of $\alpha = 0.36$.

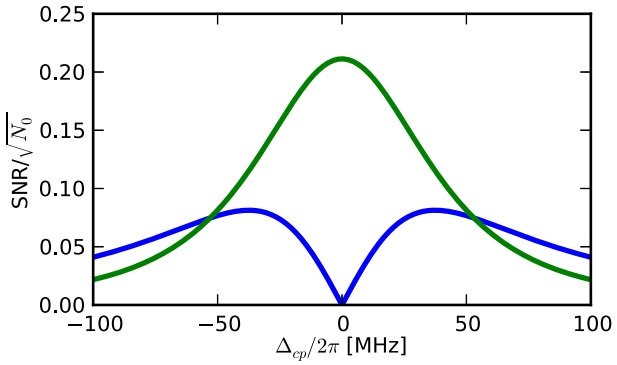

Figure 3.3.: The SNR for an intensity measurement in transmission (blue) and reflection (green) in dependence of the cavity detuning Δ_{cp}, induced by atoms in the cavity. The cavity linewidth is $\kappa = 2\pi{\cdot}53\,\mathrm{MHz}$.

We also depict the case of a lossy cavity, namely when the losses $\mathcal{L}$ are higher than the transmittance $\mathcal{T}$, since this is the case for our experimental system. Figure 3.4 shows the SNR for transmission and reflection. In contrast to the lossless case, the optimal measurement point in reflection is now at a detuning $\Delta_{cp} \neq 0$.

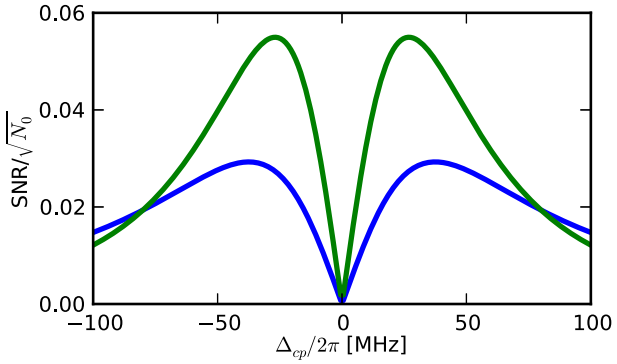

Figure 3.4.: The SNR in transmission (blue) and reflection (green) for a cavity with transmittance $\mathcal{T}$ =30 ppm and losses of $\mathcal{L}$ =53 ppm (corresponding to $\alpha = \frac{\mathcal{T}}{\mathcal{T}+\mathcal{L}} = 0.36$).

SNR in terms of scattered photons

We can also state the SNR in dependence of the number of scattered photons, which is useful if we want to infer the atom number in the QND regime or if we want to compare the counting method to a different one. According to (1.17), the number of scattered photons is related to the number of incident photons via the formula

$$N_{\mathrm{sc}} = \frac{2g_1^2\gamma}{\kappa\Delta_{ap}^2} N_0 \tag{3.5}$$

The maximal SNR for the intensity measurement in transmission is obtained at $\Delta_{cp} = {}^{k}/\sqrt{2}$. In terms of scattered photons, it is

$$\left(\frac{2}{3}\right)^{\frac{3}{2}} \frac{\alpha\Delta_{ap}}{\sqrt{\gamma\kappa}g_1}\sqrt{N_{\mathrm{sc}}}\,\Delta_{cp}^{\mathrm{at}} \tag{3.6}$$

The SNR for reflection at the same detuning can be derived in an analogue way, yielding:

$$\frac{4}{3\sqrt{3}}\frac{\alpha^2-2\alpha}{\sqrt{2\alpha^2-4\alpha+3}}\frac{\Delta_{ap}}{\sqrt{\gamma\kappa}g_1}\sqrt{N_{\mathrm{sc}}}\,\Delta_{cp}^{\mathrm{at}} \tag{3.7}$$

3.1.2. Principle of the atom number preparation

To prepare a well-defined atom number in the cavity, we combine the atom number counting method presented above with a controllable loss mechanism of atoms from the trap.

A schematic of the preparation principle is shown in figure 3.5. We load an ensemble with ill-defined atom number (typically 150-200 atoms) into the central node of the standing wave dipole trap. The atoms are initially in the state $F = 1$. The cavity and the probe laser are resonant to the $F = 2 \rightarrow F' = 3$ transition. We then shine probe light onto the cavity and monitor the cavity transmission. Initially, it is low since the atoms detune the cavity from resonance. However, the atoms can now undergo light assisted collisions [81]: An atom may get excited to $F' = 3$ by the resonant probe light. If it is close enough to an atom in the ground state, the two atoms form a loosely bound pair and interact through an attractive dipole-dipole potential. The pair can thus acquire kinetic energy before it decays back to the ground state. If this energy is bigger than the trap depth, both atoms leave the trap during such a process. While the probe light is on, atoms thus continuously leave the trap and cavity transmission increases. When it reaches a predefined threshold corresponding to the desired atom number, we switch off the probe light. This stops the loss process and we end up with a well-defined atom number in the cavity. In order to prepare different atom numbers, the empty cavity resonance can be shifted before the atom number preparation.

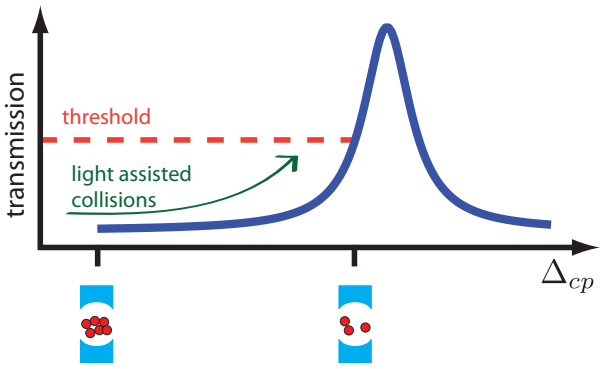

Figure 3.5.: Principle of the atom number preparation. Off-resonant atoms in the cavity induce a shift Δ_{cp}, which is proportional to the atom number. The cavity transmission (blue) is monitored while the atoms leave the cavity due to light assisted collisions. the light is switched off when the transmission reaches a certain threshold, corresponding to a well defined atom number in the cavity.

3.1.3. Experimental parameters and results

Figure 3.6a) shows a typical transmission trace of the atom number preparation. We monitor the counts in cavity transmission T_{prep} in bins of 200 µs with a SPCM and stop the probe light if $T_{\text{prep}} > 60$, which corresponds to one fifth of the mean empty cavity transmission (the empty cavity transmission count rate is set to 1.5 MHz). We then apply a short light pulse on the $F = 2 \rightarrow F' = 3$ transition, which pushes atoms in $F = 2$ out of the trap and ensures that all remaining atoms are in $F = 1$. At this point, the initial state is prepared with a well defined atom number N_{tot} in $F = 1$ and a small probability ($\simeq 10\%$) to have an atom in $F = 2$.

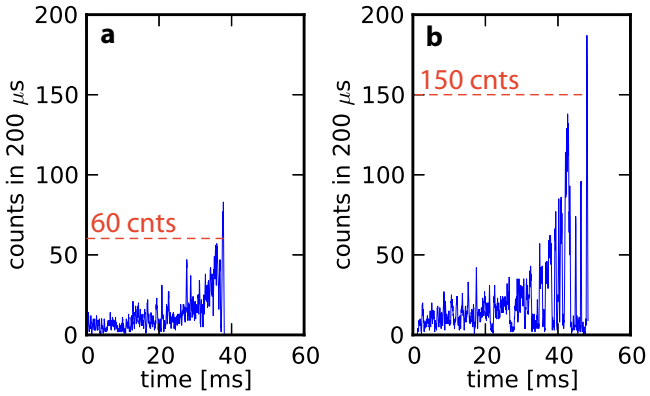

Figure 3.6.: a) Typical transmission signal during the atom number preparation. When the count rate exceeds 60 counts in 200 µs, the light is switched off and we end up with a well defined atom number in the cavity. b) Transmission trace for a threshold $T_{\text{prep}} = {}^{T_{\max}}/_{2}$. The lifetime for atoms in $F = 2$ is increased when the cavity is close to resonance (in this trace for times higher than 40 ms).This leads to longer periods of low transmission and increases the uncertainty of the prepared atom number.

We have prepared three different atom numbers N_{tot} = 73, 51, 34 by shifting the empty cavity resonance prior to the atom number preparation. We shifted by an amount of $-2\pi \cdot 240\,\mathrm{MHz}, -2\pi \cdot 105\,\mathrm{MHz}, 0\,\mathrm{MHz}$ by detuning the frequency of the cavity lock laser. The actually prepared atom number was deduced in a separate measurement by measuring the frequency shift necessary to tune the cavity back to resonance with the atoms inside.

The standard deviation of the atom number preparation can be estimated using (3.4), considering only the last detection bin. This corresponds to a detuning $\Delta_{cp} = 2\kappa$ and a photon number $N_0 = 1.5\,\mathrm{MHz} \cdot 200\,\mu\mathrm{s} = 300$. We obtain that the SNR is bigger than 1 for a signal variation of ±2 atoms. However, if we consider additional information stored in the transmission trace (e.g. the second last detection bin must have less than 60 counts etc.), we see that the method prepares the atom number more precisely. To estimate the precision, we perform a likelihood analysis on the last two detection bins: We evaluate a high number of preparation traces (>1000). For each preparation trace, we calculate the likelihood for a given atom number to produce the obtained count rates, where we assume that a certain atom number generates a Poisson distributed photon count rate. Figure 3.7 shows the mean likelihood in dependence of the atom number for a measurement where a mean atom number $N_{\mathrm{tot}} = 34$ was prepared. It fits well to a Gaussian distribution with a standard deviation of $\sigma_{N_{\mathrm{tot}}} = 1.2$ atoms.

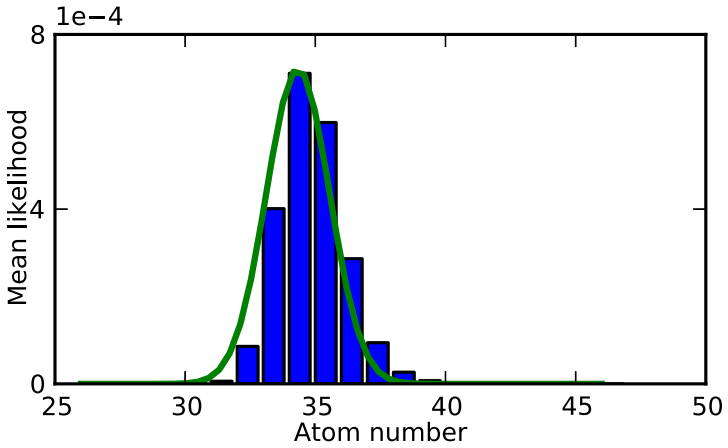

Figure 3.7.: Analysis of the atom number preparation method, shown for a mean atom number N_{tot}=34. We plot the mean likelihood to produce the obtained count rates in the last two detection bins for different possible atom numbers (blue bars). The result is fitted to a Gaussian distribution (green curve) and we obtain $\sigma_{N_{\mathrm{tot}}} = 1.2$.

We perform this analysis for all prepared atom numbers and conclude that this method can prepare a fixed atom number with a precision $\sigma_{N_{\mathrm{tot}}} < 2$ atoms. Note that this method gives an absolute error $\sigma_{N_{\mathrm{tot}}}$ which is in principle independent of the prepared atom number.

We would like to comment on two details of this preparation method.

- The loss mechanism of this method is light assisted collisions, so the atoms must necessarily scatter many photons. The atom number preparation sequence takes

on average 50 ms and the mean transmission count rate is approximately 150 kHz. Every atom in $F = 1$ therefore scatters on average 5 photons until the correct atom number is prepared. The atoms are initially in the well-defined state $|0\rangle \equiv |F = 1, m_F = 1\rangle$, but due to the many scattering events, they get distributed over the $F = 1$ manifold in the course of the atom number preparation. This means that while we can prepare a well-defined atom number in $F = 1$, we have no control over the populations in the Zeeman sublevels. We discuss the consequences for the generation of entangled states in section 4.3.4.a.

- The threshold value $T_{\text{prep}} = T_{\max}/5$ was chosen even though the SNR of the transmission measurement is maximal for $\Delta_{cp} = \kappa/\sqrt{2}$. Indeed, we had initially used a higher threshold but we have found that the lifetime of atoms in $F = 2$ is strongly increased. This leads to larger periods of low transmission in the trace (see figure 3.6b), which makes us less sensitive to atom number changes and therefore increases the uncertainty of the preparation method.
  We attribute the increased lifetime in $F = 2$ to the influence of the second cavity mode: In our experimental configuration, we tune the polarization of the probe light so that only the red cavity eigenmode is pumped. This eigenmode is set (near) resonant to the atomic transition (see figure 3.8a). Atoms in $F = 1$ shift the cavity resonance to the red which brings the second mode closer to the transition $F = 2 \rightarrow F' = 3$ (see figure 3.8b). This enables the atoms in $F' = 3$ to decay via a second channel, leading to a Purcell-enhanced spontaneous emission. This reduces the lifetime in $F = 2$ and allows us to prepare the atom number with higher precision.

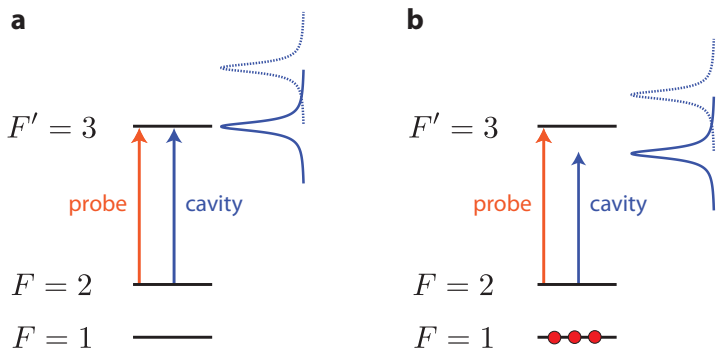

Figure 3.8.: Level scheme and cavity configuration during the atom number preparation. a) The empty cavity is set (near) resonant to the $F = 2 \rightarrow F' = 3$ transition. The polarization of the probe beam is set so that only the red eigenmode of the cavity is pumped (solid blue line). The blue cavity resonance is therefore blue detuned with respect to the atomic transition (dotted blue line). b) Atoms in $F = 1$ shift the cavity towards lower frequencies. The unpumped cavity resonance is therefore coming nearer to the atomic resonance and the spontaneous emission of atoms in $F' = 3$ is increased. This is the configuration we use in the experiment.

3.1.4. Preparation of different atom numbers in one experimental run

The atom number preparation described in this section constitutes the first step in our scheme to generate multiparticle entangled states (see chapter 4). The tomograhy of these states requires the repeated performance of many different measurements. To reduce the total measurement time, we thus want to perform several measurements with a single cold atomic sample. We have therefore devised a method to prepare different atom numbers in one experimental run.

At the beginning of each run, we prepare a well-defined atom number as described above. We then perform the scheme to generate an analyze entangled state, which in general distributes the atoms randomly in the states $|0\rangle = |F = 1, m_F = 1\rangle$ and $|1\rangle = |F = 2, m_F = 2\rangle$. We then apply a light pulse on the $F = 2 \rightarrow F' = 3$ transition to push all the atoms in $|1\rangle$ out of the trap. At this point, we have a state with reduced, ill-defined atom number in the cavity, where all the atoms are in $|0\rangle$. This is the same situation as in the beginning of the experiment and we can therefore prepare another entangled state with reduced atom number. We shift the cavity resonance so that the detuning corresponds to a smaller atom number and start a new atom number preparation procedure. Figure 3.9 shows a typical transmission trace of a full experimental run. In this case, four different atom numbers are produced.

We have to take into account the possibility that there are not enough atoms left after the previous state tomography. Such preparation traces can be easily identified and discarded, because the transmission threshold $T_{\mathrm{prep}} = {}^{T_{\max}}/_{5}$ is then instantly surpassed. However, this means that the success rate of the first atom number preparation within an experimental run is in general higher than the success rates of the following ones.

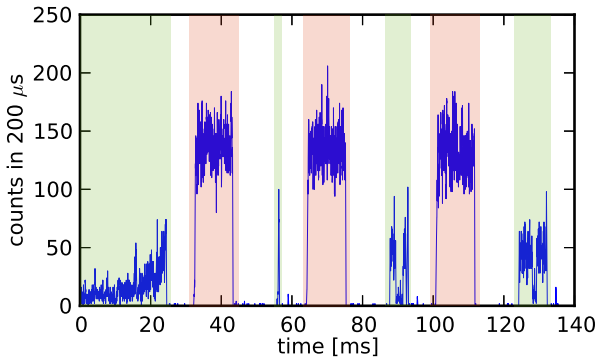

Figure 3.9.: A typical transmission trace of a full experimental cycle. The atom number preparation phases are marked in green. After each atom number preparation, an entanglement generation experiment is performed. This part is not visible in the trace, as it does not take more than 650 µs and is executed at small light intensities. At the end of every experiment phase, a light pulse is applied to push the atoms in $F = 2$ out of the trap (marked in red). In this particular trace, the result of the second atom number preparation is discarded in postselection: The transmission threshold is reached after a very short time which indicates that there are not enough atoms in the trap.

3.2. Counting atoms in a phase measurement: The Pound-Drever-Hall method

In this section, we compare the counting method via cavity intensity to a counting method via phase measurement. Photon detectors cannot measure the phase of light directly, which is why homodyne measurement techniques have been devised. One of the most common ones is the Pound-Drever-Hall (PDH) technique. We introduce it in the following and analyze the expected SNR. We then give preliminary experimental results on an atom number measurement based on the PDH method, using a SPCM.

3.2.1. The expected SNR

Measurement principle

The Pound-Drever-Hall method (PDH) was first introduced in [63] as a method to stabilize the frequency of a laser with the help of an external cavity. Here, we invert this scheme to probe fluctuations in cavity length (introduced by a certain number of atoms in the cavity) using a laser with stable frequency. We use the setup schematically presented in figure 3.10. The light of a laser is modulated by a phase modulator (most commonly an electro-optical phase modulator (EOM)) and sent onto a Fabry-Pérot cavity. At the modulation frequency, the reflected light now contains the information of the intensity response to frequency changes of the laser. To obtain this information, the reflected light is separated from the incident beam and sent onto a fast photodiode (PD). The part oscillating at the modulation frequency is isolated by mixing the signal with the local oscillator. Hereby, a DC signal is generated, which can be isolated by a low-pass filter. Within a region of $\Delta_{cp} = \pm\kappa$, it is proportional to the frequency shift of the cavity Δ_{cp}.

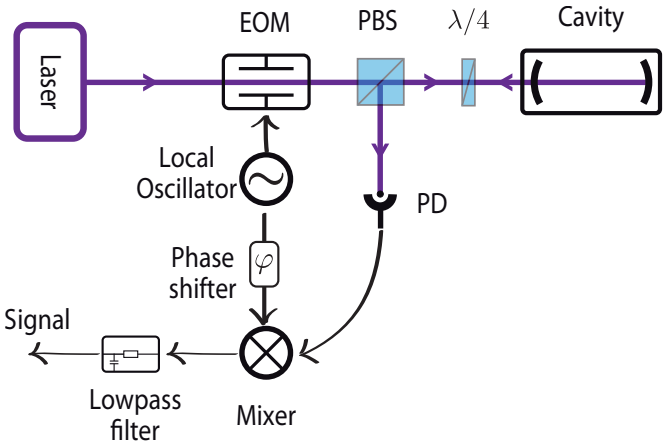

Figure 3.10.: A typical PDH setup.

Quantitative description

We consider a laser being phase modulated at Ω, which is the equivalent of adding two sidebands at $\pm\Omega$, with the amplitudes of the different frequency components given by

the Bessel-functions J_0 and J_1 and the modulation depth β. The full derivation of the PDH signal is e.g. given in [82]. Here, we directly state the result in terms of incident photons N_0. Within a cavity detuning of $\Delta_{cp} = \pm\kappa$, the PDH signal can be approximated by a linear slope $D \cdot \Delta_{cp}$ with gradient

$$D = -2\alpha/\kappa \sqrt{2J_0^2(\beta)J_1^2(\beta)}\, N_0 \tag{3.8}$$

A typical PDH signal for the parameters of our cavity and $\Omega = 2\pi \cdot 230\,\mathrm{MHz}$ is shown in figure 3.11.

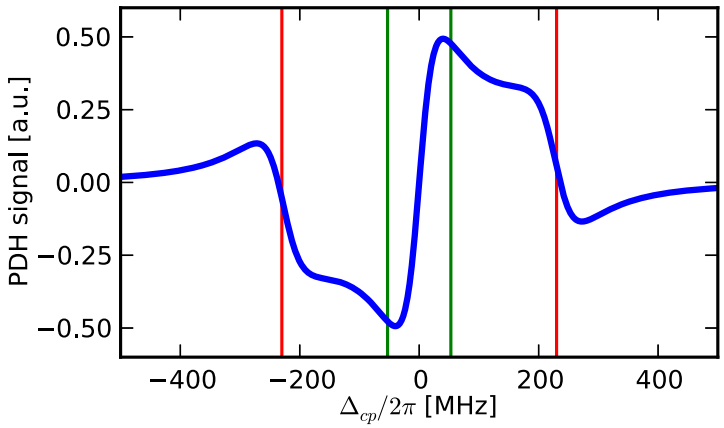

Figure 3.11.: The signal of a PDH measurement using a cavity with $\kappa = 2\pi{\cdot}53\,\mathrm{MHz}$ (green bars) and a modulation frequency of $\Omega = 2\pi{\cdot}230\,\mathrm{MHz} = 4.3\,\kappa$ (red bars). The error signal is approximately linear from $-\kappa < \Delta_{cp} < \kappa$.

As for the intensity measurement, the fundamental limit for the PDH method is photon shot noise. The mean light power incident on the photodiode oscillates at the modulation frequency and thus the associated shot noise is nonstationary. However, we can assume a resulting noise as a white distribution with a power spectrum equal to the average energy of the noise [2].
With this assumption, the shot noise is proportional to the square root of number of reflected photons R:

$$\sqrt{R} \approx \sqrt{|F(\Delta_{cp})|^2 J_0^2(\beta) + 2J_1^2(\beta)}\sqrt{N_0} \tag{3.9}$$

Here, we have introduced the reflection coefficient of the cavity $F(\Delta_{cp})$:

$$F(\Delta_{cp}) = \frac{1 - \alpha - i\Delta_{cp}/\kappa}{1 - i\Delta_{cp}/\kappa} \tag{3.10}$$

We have also assumed that the photons in the sidebands are totally reflected by the cavity. The SNR at a detuning of $\Delta_{cp} = 0$ - the detuning with maximal SNR - therefore

2. This assumption is justified as the correction factor is only a few percent (cf. [83]). A more subtle analysis is given in [83, 84].

amounts to:

$$\mathrm{SNR} = \frac{2\alpha}{\kappa} \frac{J_0(\beta)J_1(\beta)}{\sqrt{(1-\alpha)^2 J_0^2(\beta) + 2J_1^2(\beta)}} \sqrt{N_0}\, \Delta_{cp}^{\mathrm{at}} \tag{3.11}$$

Figure 3.12 shows the SNR for a PDH measurement. For $\Omega = 4.4\kappa$, it is approximately six times smaller than the SNR of an intensity measurement in reflection (cf. figure 3.4).

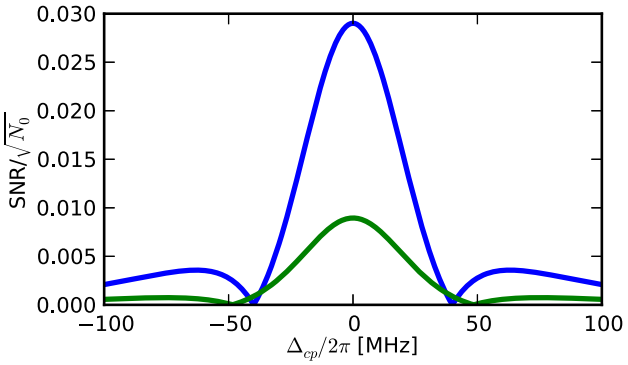

Figure 3.12.: The SNR in a PDH measurement in dependence of the detuning of the cavity Δ_{cp} for an ideal cavity (blue) and a lossy cavity with $\alpha = 0.36$ (green). The experimental parameters are $\kappa = 2\pi \cdot 53\,\mathrm{MHz}$, $\beta = 1.2$ and $\Omega = 2\pi \cdot 230\,\mathrm{MHz}$.

SNR in terms of scattered photons

One might think that the PDH measurement is better suited for photon counting in the QND regime, since the photons at the modulation frequency do not enter the cavity and cannot cause spontaneous emission. However, a comparison of the SNR in terms of scattered photons shows that this is not true.

As in for the intensity measurement, we depict N_0 in the number of scattered photons N_{sc}. Here, however, we also have to take into account the photons in the sidebands and their detuning with respect to the cavity $\Delta_{cp} = \pm\Omega$ and with respect to the atom $\Delta_{ap} = \Delta_{\mathrm{HF}} \pm \Omega$. This is a cumbersome expression and we only state the result in the limit of high modulation frequencies, where N_{sc} is minimal and the SNR is maximal:

$$N_{\mathrm{sc}} = N_0 \left(\frac{J_0^2(\beta) 2 g_1^2 \gamma}{\kappa \Delta_{\mathrm{HF}}^2} + \frac{4 J_1^2(\beta) g_1^2 \kappa \gamma}{\Omega^4} \right) \tag{3.12}$$

We insert (3.12) in (3.11) and obtain in the limit of large modulation depth:

$$\mathrm{SNR} = \sqrt{2} \frac{\alpha \Delta_1 \Delta_{ap}}{\sqrt{\gamma \kappa}\, g_1} \sqrt{N_{\mathrm{sc}}}. \tag{3.13}$$

It is the same SNR as for an intensity measurement in reflection.

We conclude that the SNR in terms of scattered photons is always lower in a PDH measurement and that it gives the same results as an intensity measurement for high modulation frequencies and high modulation depths. The PDH technique is thus not superior to a simple intensity measurement if only shot noise is considered [3].

3. In contrast to shot noise, most technical noise has a spectrum that falls off at higher frequencies.

3.2.2. Preliminary measurements using a SPCM

Measurement principle

We perform test measurements with our experimental setup to verify the theoretical predictions and identify the contribution of technical noise in addition to the shot noise. In later experiments, the counting scheme should be the starting point for experiments where we need to be able to count single photons. We therefore use a SPCM instead of a normal photodiode to detect the photons reflected from the cavity. The voltage signal of the SPCM is sent to a time-to-digital converter (TDC), which can translate the arrival time of a voltage pulse into a digital signal. This makes it impossible to simply demodulate our signal using a mixer, since the voltage signal generated by the TDC is only non-zero at the arrival time of a photon. We therefore extract the signal at the modulation frequency by calculating the Fourier transform of the TDC time trace.

Preliminary experimental results

In these first measurements, we do not load atoms in the cavity, but simulate their presence by detuning the cavity resonance by a controlled amount $\Delta_{cp} = N_{\text{atom}} \cdot 2\pi \cdot 5.6\,\text{MHz}$. The probe intensity is adjusted so that the scattering probability per atom is approximately 1%. The modulation frequency is set to $\Omega = 2\pi \cdot 230\,\text{MHz}$ [4].

We measure the PDH signal for a detuning of up to $\Delta_{cp} = 2\pi \cdot 50.4\,\text{MHz}$ in steps of $2\pi \cdot 5.6\,\text{MHz}$, which corresponds to a maximal shift caused by 9 atoms in the cavity. Figure 3.13 shows the SNR obtained in this experiment, compared to the SNR we expect from theory.

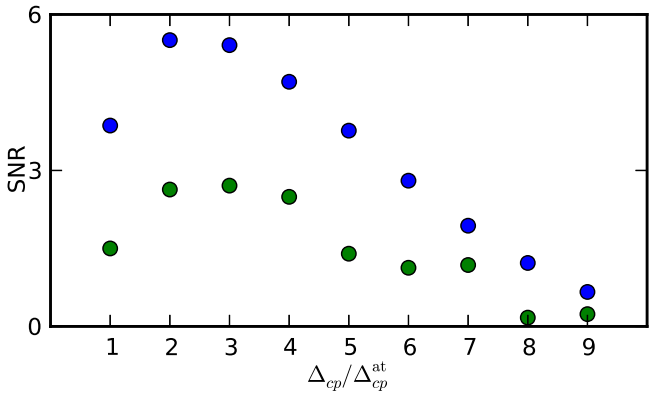

Figure 3.13.: The signal obtained in a PDH measurement using a SPCM, in dependence of the cavity detuning Δ_{cp}. The experimental data (in green) can be compared to the theoretical expectation (in blue).

The result of the experiment (see figure 3.13) shows a SNR > 1 for atom numbers from

Since the PDH method only relies on the signal at the modulation frequency, it reduces such noise contribution to the signal. It is thus the method of choice in experimental systems where the SNR is not limited by shot noise.

4. We have seen in the last section that a higher Ω leads to an increase of the SNR. However, we cannot increase Ω further, since the voltage signal of the SPMC has a time jitter of 400 ps.

1 to 7. The best SNR of 2.7 is obtained at a detuning corresponding to 3 atoms. The result is in agreement with the theoretical expectation with a noise that is approximately twice as much as expected from shot noise. This means that our detection method is still dominated by technical noise. The main contributions are

- the probe laser frequency,
- the probe laser intensity,
- the TDC resolution,
- the cavity lock.

Noise analysis shows that by far the main contribution stems from the cavity lock system.

Obviously, the next experimental step is to repeat the measurement with real atoms in the cavity. We do not expect the performance of the measurement to decrease substantially in this case: Since the experiment is performed in the QND regime, the coupling $\widetilde{g} = \sqrt{N} g_1$ of the ensemble to the cavity mode should not change during the measurement (e.g. due to recoil heating or light assisted collisions).

While the results of the measurement indicate that we can in principle perform atom counting measurements in the QND regime, the PDH measurement is not the most suitable method. The experiment could therefore be repeated using an intensity measurement and the results could be compared.

3.3. Conclusion

In this chapter, we have presented a method to prepare a well-defined atom number in the cavity. It is based on the measurement of transmission while a loss process due to light assisted collisions slowly reduces the number of atoms. We have used it to prepare different atom numbers up to $N_{\mathrm{tot}} = 73$ atoms with a standard devation $\sigma_{N_{\mathrm{tot}}} < 2$.

Furthermore, we have investigated an atom number counting method based on the PDH technique, using a SPCM. We have analyzed the SNR and have performed preliminary experimental results with an empty cavity that confirmed the theoretical expectation.

4. Generation and tomography of W states

The generation of entanglement between material particles is a challenging task and a vivid field of current research. Different approaches have been conducted to increase the number of entangled particles and to analyze the produced state.

In this chapter, we present an entanglement method in which the collective nature of the cavity measurement enables the generation of comparably large entangled states. We use this method, based on a weak collective excitation, followed by a collective QND measurement to create W states. In section 4.2, we explain the principle of the entanglement scheme and give the experimental parameters.

Furthermore, we show that we can use the internal state detection with the cavity to characterize the created state. More precisely, we perform quantum tomography by directly measuring the state's Husimi Q function. In section 4.3, we introduce the Q function and explain how it can be measured with our experimental system. We then give experimental results on the generation and tomography of W states of up to 41 atoms.

After its creation, the W state is subject to decoherence. In an additional measurement, we use the Q function to measure the temporal evolution of this decoherence. We compare it to a model assuming a hot atomic cloud in a dipole trap and infer the cloud temperature.

4.1. Dicke states and Coherent spin states

We want to create entanglement in an ensemble of N particles. In our case, the particles can be approximated as two-level systems with the states $|0\rangle$ and $|1\rangle$ encoded in the hyperfine ground level structure of ^{87}Rb (see figure 1.5). To describe the state of the ensemble and the tomography technique, we first introduce two classes of N particle states: Dicke states and Coherent spin states.

Dicke states

We consider a system composed of N two-level atoms with levels $|0\rangle$ and $|1\rangle$. It can be described by a total spin vector $\mathbf{J} = \sum_{j=1}^{N} \mathbf{J}^{(j)}$ that is the sum over the spins $\mathbf{J}_i$ of the spin-$^1/_2$ atoms. The eigenstates $\{|J, J_z\rangle\}$ of the operators

$$\begin{aligned} J^2 &= J_x^2 + J_y^2 + J_z^2 \qquad \text{and} \\ J_z &= \sum_{j=1}^{N} J_z^{(j)} \end{aligned} \tag{4.1}$$

form a convenient basis of the system. We describe a part of the Hilbert space in more detail: The subspace $\mathcal{H}_s$, formed by the states which are symmetric under particle

exchange. A system which is initially prepared in this subspace (e.g. by putting all atoms in the state $|0\rangle$) stays there as long as only operations are performed that act on all atoms in the same way.

All states in $\mathcal{H}_s$ have a maximal total spin $J = N/2$. The so-called "Dicke states" [21]

$$\left\{|n_N\rangle \equiv \left|J = \frac{N}{2}, J_z = -\frac{N}{2} + n\right\rangle\right\} \qquad n = 0, 1, \ldots, N \tag{4.2}$$

form a basis of $\mathcal{H}_s$. Figure 4.1 shows the level scheme for a system of N two-level atoms with the Dicke states in the top row.

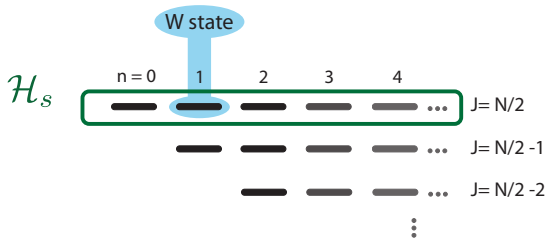

Figure 4.1.: The level scheme of a system of N two-level atoms. The subspace $\mathcal{H}_s$ of symmetric states is spanned by the Dicke states. The W state is the Dicke state of first order $|1_N\rangle$.

The spin in z direction of the Dicke state $|n_N\rangle$ is $J_z = -\frac{N}{2} + n$, which means that n atoms are in the state $|0\rangle$, while $N - n$ atoms are in the state $|1\rangle$. The Dicke state $|n_N\rangle$ can therefore be regarded as the atomic counterpart of the optical Fock state $|n\rangle$, which describes n excitations of a given mode of the electromagnetic field. Mathematically, the Dicke states translate into the Fock states in the limit $N \to \infty$ via the Holstein-Primakoff transformation [85, 86].

In the experiment presented in this chapter, we want to create the Dicke state of first order $|1_N\rangle$, which is also known as "W state" [87]. It consists of one excitation, which is symmetrically shared by N atoms. The nature of the state becomes clear when we write it in the qubit basis [1]:

$$|1_N\rangle = \frac{1}{\sqrt{N}}\left[|10\ldots0\rangle + |010\ldots0\rangle + \cdots + |00\ldots1\rangle\right] \tag{4.3}$$

This state contains N-particle entanglement [2] and has therefore risen interest in diverse fields of quantum mechanics such as quantum information [88] or quantum metrology [30, 89]. It has already been realized in different physical systems such as ions [33], neutral atoms [90], superconducting qubits [91] or photons [92].

1. We have already briefly mentioned Dicke states in chapter 1, where a single *optical* excitation was shared by the atoms. In contrast, here the excitation consists of an atom in $|1\rangle$, corresponding to the long-living hyperfine ground state $F = 2$.
2. We comment on the entanglement properties of the W state in more detail in section 5.3.3.

Coherent spin states
Another important class of states in the symmetric subspace are the "coherent spin states" $|\theta, \phi\rangle$ (CSS). They are the superposition of all atoms in the same spin state:

$$|\theta, \phi\rangle = [\cos(\theta/2)|0\rangle + \sin(\theta/2)e^{i\phi}|1\rangle]^{\otimes N} \tag{4.4}$$

These states are classical, in the sense that there are no quantum correlations between the individual atoms. They can be regarded as the atomic counterpart of optical coherent states. Just as optical coherent states can be created by applying the displacement operator on the vacuum state, the CSS can be created by applying the rotation operator $R_{\theta,\phi}$ on the state $|0_N\rangle$ [93, 86]:

$$|\theta, \phi\rangle = R_{\theta,\phi}|0_N\rangle \tag{4.5}$$

In further analogy to optical coherent states, the CSS form an overcomplete set in the symmetric subspace $\mathcal{H}_s$:

$$\frac{N+1}{4\pi}\int |\theta, \phi\rangle\langle\theta, \phi| \, d\Omega = 1 \qquad d\Omega = \sin\theta d\theta d\phi \tag{4.6}$$

and they are not orthogonal:

$$\langle\theta = 0, \phi = 0|\theta, \phi\rangle = \cos(\theta/2)^N \tag{4.7}$$

Naturally, the CSS can be expressed in the Dicke state basis [94]:

$$|\theta, \phi\rangle = \sum_{n=0}^{N} \cos(\theta/2)^{N-n} \sin(\theta/2)^n e^{i\phi} \left[\frac{N!}{(N-n)!\,(n)!}\right]^{1/2} |n_N\rangle \tag{4.8}$$

4.2. Generation of the W state

4.2.1. Principle of the state generation

Our technique for generation of entanglement does not rely on the interaction between the particles, but on the collective coupling of all particles to a single mode of the electromagnetic field.

The scheme makes use of two unique features of our experimental setup:

- We are able to couple many atoms equally to the cavity mode:
  The high gradient, strongly confining magnetic potentials of the atom chip allow us to evaporatively cool an ensemble of approx. 100 atoms down below or near quantum degeneracy and to load it into a single antinode of the standing wave dipole trap mediated by the cavity. This means that the only variation in the coupling strength g arises from the finite size of the atomic cloud. As we have already discussed in section 1.4.3, a symmetric measurement can be realized as long as the cloud temperature is below $\Theta_{\max} = 5\,\mathrm{mK}$. We will find in section 4.4 that the cloud temperature in our experiments is approximately 0.5 mK.
- We are able to perform a QND measurement:
  In section 1.4, we have shown that in the regime of weak probing, we can infer if all the atoms in an ensemble are in the state $F = 1$ without spontaneous emission of a photon.

These two features allow us to generate multiparticle entangled states. Our method consists of two consecutive steps: Weak excitation and a projective measurement.

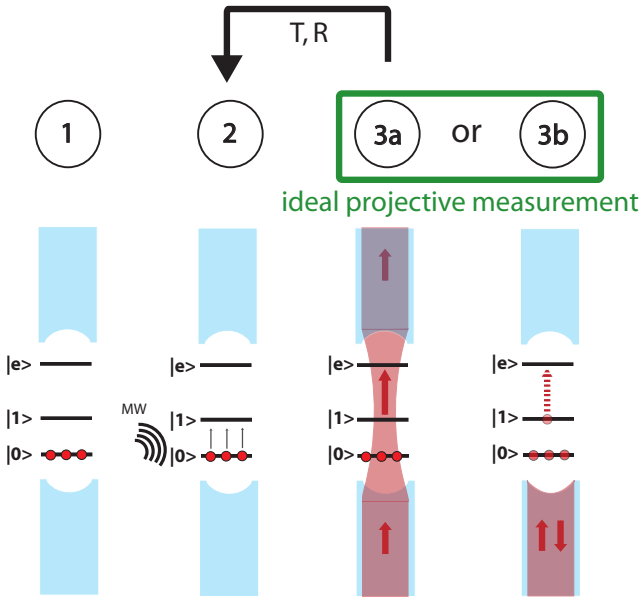

Figure 4.2.: Our experimental principle to create multiparticle entangled states. The individual steps are described in the text.

The principle of the method is shown in figure 4.2. The cavity and the probe light are resonant to the transition $|1\rangle \rightarrow |e\rangle$. We load a well-defined number of atoms into the cavity and prepare them in the state $|0_N\rangle$ (1). We then excite the ensemble with a MW pulse which couples the states $|0\rangle$ and $|1\rangle$. If the probability p to excite an atom is small, this prepares the state $|\Psi\rangle = \sqrt{1-p}|0_N\rangle + \sqrt{p}|1_N\rangle$ (2). We then measure $|\Psi\rangle$ in a QND state detection measurement. Hereby, the state is either projected onto $|0_N\rangle$ in which case we repeat the MW excitation pulse (3a) or it is projected onto the desired state $|1_N\rangle$ (3b). We detect the outcome of the measurement by monitoring the cavity transmission T and reflection R. If we see high T and low R, we assume that the ensemble is in state $|0_N\rangle$ and repeat the MW pulse until we finally detect low T and high R, indicating that the target state $|1_N\rangle$ is prepared.

4.2.2. Experimental realization

We prepare a well-defined atom number in the state $|0\rangle$ with the method presented in section 3.1. We then adjust the cavity to be resonant with the $|1\rangle \rightarrow |e\rangle$ transition, taking into account the presence of the other atoms in the $F = 1$ manifold. The probe power is set so that the mean count rate in reflection (transmission) is on average 180 kHz (95 kHz) if all atoms are in in $|0\rangle$ and 350 kHz (1 kHz) if at least one atom is in $|1\rangle$. We probe the cavity transmission during 25 µs in order to make sure that all the atoms are in $|0\rangle$ with a probability of at least 98%. We then apply the preparation sequence, which consists in a MW pulse followed by a QND cavity measurement. The

probability that the MW pulse transfers one atom to $|1\rangle$ is set to $p = 0.27, 0.23, 0.33$ [3] (depending on the prepared atom number). The cavity measurement consists in sending on average 20 photons onto the cavity over 20 µs and monitoring the counts in reflection R and transmission T. The scattering probability for an atom in $|1\rangle$ can be inferred from the solution of the master equation to be approximately 20% (see figure 1.7). We consider that the MW pulse transferred at least one atom if $T = 0$ and $R \geq 4$, otherwise the sequence is repeated. The two detection errors corresponding to this choice, $\epsilon_{01}^{\text{prep}}$ ($\epsilon_{10}^{\text{prep}}$), are respectively defined as the probability to measure all atoms in $F = 1$ (at least one atom in $F = 2$) if at least one atom is in $F = 2$ (all the atoms are in $F = 1$). They can be calculated from the mean number of counts during 20 µs, T_{mean} and R_{mean}:

$$\begin{aligned} \epsilon_{01}^{\text{prep}} &= \left(1 - \exp[-T_{\text{mean}}^{\text{F2}}]\right) + \exp[-T_{\text{mean}}^{\text{F2}}] \cdot \sum_{k=0}^{3} \text{Pois}(R_{\text{mean}}^{\text{F2}}, k) = 0.01 \\ \epsilon_{10}^{\text{prep}} &= \exp[-T_{\text{mean}}^{\text{F1}}] \cdot \sum_{k=4}^{\infty} \text{Pois}(R_{\text{mean}}^{\text{F1}}, k) = 0.07 \end{aligned} \tag{4.9}$$

The asymmetric choice of the detection error makes sure that we do not exclude runs where a W state is prepared. In addition, after the measurement, we can discard runs where $T = 0$ and $R \geq 4$ but where R is below an additional threshold R_{prep}. The influence of the parameter R_{prep} on the state fidelity is shown in section 5.2. The preparation sequence is repeated at most 20 times. If no W state is prepared after 20 repetitions, the experimental run is discarded. Figure 4.3 shows a histogram of the reflection counts of the successful preparations. In this case, the transmission counts are always 0.

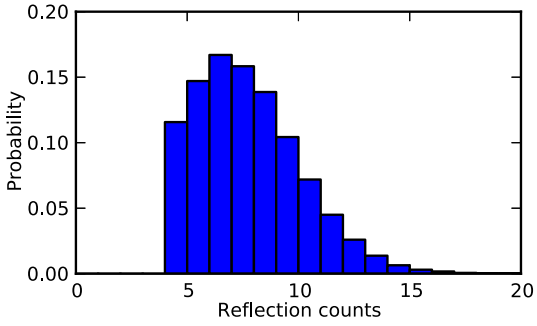

Figure 4.3.: Histogram of the reflection counts during the preparation measurement in the case of a successful preparation. There are no counts for $R < 4$ because in this case, the preparation sequence is repeated.

After a QND measurement with successful outcome, the W state is prepared and can be analyzed via quantum state tomography.

3. The Rabi frequency of the $|0\rangle \rightarrow |1\rangle$ transition is set to 104 kHz and we apply a pulse of length $\Delta t = 0.3\,\mu\text{s}, 0.35\,\mu\text{s}, 0.675\,\mu\text{s}$.

4.3. Tomography of the W state

A way to characterize a multiparticle quantum state is to determine the quantum state of each participating particle individually. This is done e.g. in ion experiments [32, 33, 38]. The method, however, is not applicable if the particles cannot be individually addressed.

Another possibility is to measure a quasi-probability distribution. An example of such a distribution is the Wigner function [95], which has e.g. been obtained from Stern-Gerlach type experiments [42, 96, 97]. Another example is the Husimi Q function, which we introduce in the following. As we will see, our experimental setup is well-suited to measure it directly, giving us access to the symmetric part of the state's density matrix.

4.3.1. The Husimi Q function

The Husimi Q function [98, 99] is a quasiprobability function which measures the overlap of the state (represented by its density matrix ρ) with the coherent state $|\theta,\phi\rangle$:

$$Q(\theta,\phi) = \frac{N+1}{4\pi}\langle\theta,\phi|\rho|\theta,\phi\rangle = \frac{N+1}{4\pi}\langle 0_N|R_{\theta,\phi}\rho R^\dagger_{\theta,\phi}|0_N\rangle \tag{4.10}$$

We directly see from (4.10) that the Q function is always positive[4], bounded and normalized:

$$0 \leq Q(\theta,\phi) \leq \frac{N+1}{4\pi} \tag{4.11}$$

$$\int Q(\theta,\phi)\,\mathrm{d}\Omega = 1 \qquad \mathrm{d}\Omega = \sin\theta \mathrm{d}\theta\mathrm{d}\phi \tag{4.12}$$

As the CSS form an overcomplete basis, the Q function is equivalent to the density matrix ρ, i.e. the Q function holds the full information of a state in the symmetric subspace.

$$\rho = \int Q(\theta,\phi)|\theta,\phi\rangle\langle\theta,\phi|\,\mathrm{d}\Omega \qquad \mathrm{d}\Omega = \sin\theta\mathrm{d}\theta\mathrm{d}\phi \tag{4.13}$$

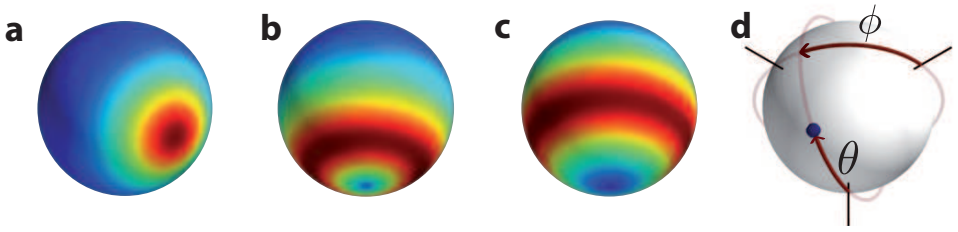

Figure 4.4.: Representation of the Q function on the multiparticle Bloch sphere for different states. a) CSS $|\theta = 0.8, \phi = 0\rangle$ containing 20 atoms. b) Dicke state $|n = 2_{N=20}\rangle$. c) Dicke state $|n = 5_{N=20}\rangle$. d) Coordinate system used in a), b) and c). This representation is also used in all the following drawings of a multiparticle Bloch sphere.

4. This is an important difference with respect to the Wigner function, which takes negative values or entangled states.

The Q function can be graphically expressed on the surface of a sphere, the "multi-particle Bloch sphere". In close analogy to the single-particle Bloch sphere, this sphere has a radius $J = {}^{N}/_{2}$ and its south pole ($\theta = 0$) corresponds to the state $|0_N\rangle$, while its north pole ($\theta = \pi$) corresponds to the state $|1_N\rangle$. Figure 4.4a) shows the Q function of the coherent state $|\theta = 0.8, \phi = 0\rangle$ containing 20 atoms. Since the coherent states are not orthogonal, the Q function is not point like, but has a finite radius around its mean spin direction. Figure 4.4b) depicts the Q function of the Dicke state $|n = 2_{N=20}\rangle$. It forms a ring on the Bloch sphere, which illustrates that while the z component of the spin is well defined, the spin components in the other directions - being the conjugate variables - are completely undefined. Comparison of the images b) and c) show that the Q function of two orthogonal states (such as the two represented Dicke states) can have an overlap. The Q function thus violates the third probability axiom [100], which is the reason why it is considered a quasiprobability function [101].

4.3.2. Measuring the Husimi Q function using a cavity

As seen in the previous section, the Q function at the angle (θ, ϕ) is the measurement of the overlap between a state ρ and the coherent state $|\theta, \phi\rangle$. Such a measurement can be realized with the help of our cavity.

We consider a well defined number of N atoms in the cavity. As already pointed out in section 1.4, the cavity can distinguish either if all the atoms are in the state $(|0\rangle)^{\otimes N} \equiv |0_N\rangle$ (high transmission / low reflection) or if at least one atom is in the state $|1\rangle$ (low transmission / high reflection).

The probability $p(|0_N\rangle)$ of the measurement outcome $|0_N\rangle$ gives directly the value of the Q function at the angle $\theta = 0$:

$$Q(\theta = 0) = \frac{N+1}{4\pi}\langle\theta = 0|\rho|\theta = 0\rangle = \frac{N+1}{4\pi}p(|0_N\rangle) \tag{4.14}$$

We can measure the Q function at other angles by rotating the state ρ prior to the measurement:

$$Q(\theta, \phi) = \frac{N+1}{4\pi}\langle\theta = 0|R_{\theta,\phi}\rho R^{\dagger}_{\theta,\phi}|\theta = 0\rangle \tag{4.15}$$

Since our states $|0\rangle$ and $|1\rangle$ correspond to the hyperfine ground states $|F = 1, m_F = 1\rangle$ and $|F = 2, m_F = 2\rangle$ of ^{87}Rb, the rotation $R_{\theta,\phi}$ can be realized using a resonant MW pulse.

Figure 4.5 shows the consecutive steps of a Q function measurement with the help of the cavity.

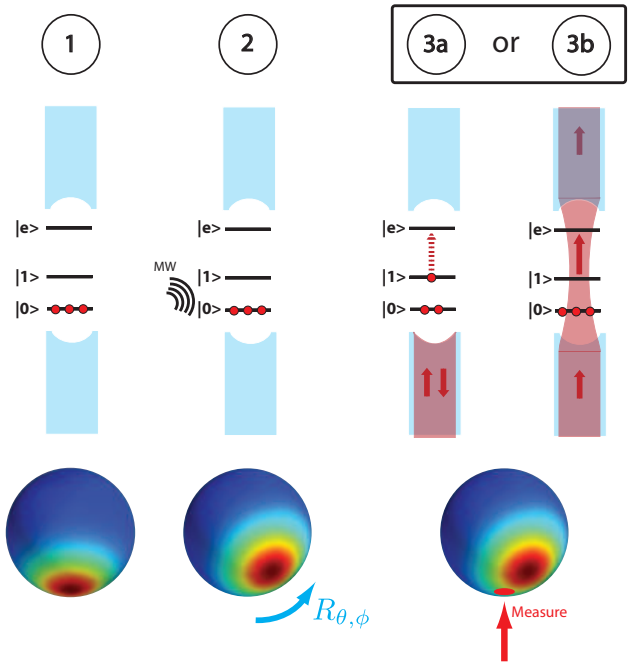

Figure 4.5.: The steps to realize a measurement of the Q function at the angle (θ, ϕ) with our cavity. The first row indicates the consecutive time steps. The second row shows the state in the cavity, and the third row shows a representation of the state on the multiparticle Bloch sphere. As an example, the tomography measurement is performed on the state $|0_N\rangle$ (1). We use a MW pulse of well-defined length and phase to rotate the state by the angle (θ, ϕ) (2) and perform a state detection measurement (3). In the last step, either event (3a) or (3b) is realized. The probability for the outcome (3a) is $p(|0_N\rangle) = \langle 0_N|R_{\theta,\phi}\rho R^\dagger_{\theta,\phi}|0_N\rangle = \frac{4\pi}{N+1}Q(\theta,\phi)$. Therefore, the average of several measurements at the same tomography angle allows to infer the value of $Q(\theta, \phi)$.

One single measurement realization can only yield the result 1 or 0. We therefore only obtain one bit of information per measurement and have to repeat the measurement at one angle (θ, ϕ) several times to obtain the expectation value $\langle\theta, \phi|\rho|\theta, \phi\rangle$, which corresponds to $Q(\theta, \phi)$.

What happens if the state ρ in the cavity is not (entirely) in the symmetric subspace? We can decompose ρ in the part ρ_{sym} which lies in the symmetric subspace $\mathcal{H}_s$ and the remaining part $\rho_{\text{n.sym}}$:

We define P as the projector on the subspace $\mathcal{H}_s$ and $\bar{P}$ as $\bar{P} = \mathbb{1} - P$. We can thus write ρ as:

$$\rho = P\rho P + \bar{P}\rho\bar{P} + \bar{P}\rho P + P\rho\bar{P} \tag{4.16}$$

with $\rho_{\text{sym}} = P\rho P$. The coherent state $|\theta, \phi\rangle$ lies entirely in the symmetric subspace and thus $\bar{P}\,|\theta, \phi\rangle = 0$. When we insert (4.16) in (4.10), we therefore obtain:

$$Q(\theta, \phi) = \frac{N+1}{4\pi}\,\langle\theta, \phi|\,P\rho P\,|\theta, \phi\rangle = \frac{N+1}{4\pi}\,\langle\theta, \phi|\,\rho_{\text{sym}}\,|\theta, \phi\rangle \tag{4.17}$$

This proves that the cavity measurement is a direct measurement of the Q function of

the symmetric part of the density matrix. Figure 4.6 shows the possible values of the Q function for a level scheme of N two-level systems.

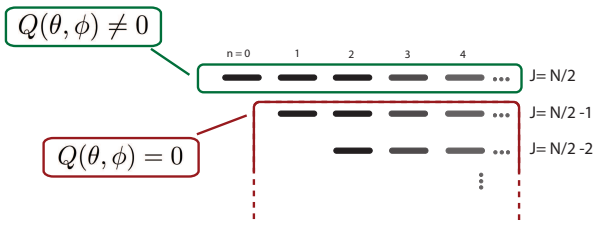

Figure 4.6.: Level scheme of a system of N two-level systems. The symmetric states ($J = {}^{N}/_{2}$) are the only states that can contribute to the Q function and are marked in green. The states in the nonsymmetric subspace ($J < {}^{N}/_{2}$) do not contribute to the Q function and are marked in red.

To illustrate the result of (4.17), we determine the value of the Q function of the state $|\psi_{\mathrm{sc}}\rangle$, which describes one well defined atom in $|1\rangle$ while all the other atoms are in $|0\rangle$. In the single spin basis, the state reads (cf. (4.3)):

$$|\psi_{\mathrm{sc}}\rangle = |10\ldots0\rangle \tag{4.18}$$

This state is particularly interesting in our case, since it occurs if the external state of the atom in $|1\rangle$ is revealed to the environment, due to e.g. a scattering event. In the basis $\{|J, J_z\rangle\}$, it is composed of the state $|1_N\rangle$ and of states that do not lie in the symmetric subspace [5]:

$$|\psi_{\mathrm{sc}}\rangle = \frac{1}{\sqrt{N}}|1_N\rangle + \frac{1}{\sqrt{N}}\sum_{i=1}^{N-1}|J = {}^{N}/_{2} - 1, m = -{}^{N}/_{2} + 1\rangle_i \tag{4.19}$$

From (4.17), we see that only the first term of $|\psi_{\mathrm{sc}}\rangle$ can contribute to a non-zero Q function. The state $|\psi_{\mathrm{sc}}\rangle$ therefore gives the same Q function as $|1_N\rangle$ with an amplitude reduced by the factor ${}^{1}/_{N}$. This example shows that a non-normalized Q function allows to infer a states' population in the symmetric subspace.

4.3.3. Experimental realization

After the state preparation, we apply a MW pulse with adjustable duration and phase that performs the rotation $R_{\theta,\phi}$ required for the tomography. We then measure the cavity transmission and reflection for 120 μs in order to determine the Q function $Q(\theta, \phi)$ as described in section 4.3.2.

In order to minimize the error of the tomography state detection, we do not simply compare the number of counted photons to a threshold. Instead, we analyze the full, time-resolved transmission and reflection traces and use a maximum likelihood algorithm to calculate the probability for a trace to be caused by either a state $|0_N\rangle$ or by a state

5. The state $|J = {}^{N}/_{2} - 1, m = -{}^{N}/_{2} + 1\rangle_i$ is $(N-1)$-fold degenerate. We denote the different states with the index i.

with at least one atom in $|1\rangle$. In this calculation, we also account for the possible occurrence of jumps in the cavity signal from high transmission to low transmission or vice versa. The state detection therefore not only depends on the count rates during 120 µs, but also on the lifetimes τ_0, τ_1 of the states $|0_N\rangle$ and "at least one atom in $|1\rangle$", respectively. These lifetimes are proportional to the number of atoms in $|0\rangle$ and $|1\rangle$ and therefore depend on the atom number N of the state and the tomography angle θ of the state detection. We have obtained the lifetimes in an independent measurement for each atom number and each tomography angle (see figure 4.7a). For high tomography angles, the atoms are predominantly in $F = 2$. Therefore, there are very few traces that start in the state $|0_N\rangle$, which means that we cannot assign a lifetime τ_0. Furthermore, the lifetime τ_1 gets bigger than our measurement time and we cannot assign a value either. This is why for $\theta > 0.7$, we assign the lifetime of the highest tomography angle for which we still obtain a result. Moreover, we assume that the lifetimes are independent of the sign of the tomography angle θ, $\tau(\theta) = \tau(-\theta)$ [6].

From the maximum likelihood calculation, we can infer the detection error $\epsilon_{10}^{\text{tom}}$ ($\epsilon_{01}^{\text{tom}}$) to assess the measurement to the state $|0_N\rangle$ ("at least one atom in $|1\rangle$") even though the system is in the state "at least one atom in $|1\rangle$ ($|0_N\rangle$). As for the lifetimes, we obtain a different error for each each tomography angle. The errors are always below 5% (see figure 4.7b).

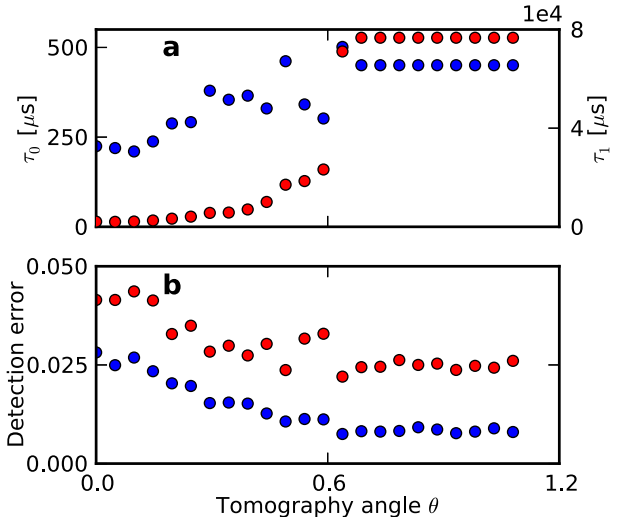

Figure 4.7.: Lifetimes and detection errors for a state containing $N = 41$ atoms. a) Measurement of the lifetimes τ_0 (blue dots, left y axis) and τ_1 (red dots, right y axis) in dependence of the tomography angle θ. For $\theta > 0.7$ we cannot obtain any lifetimes from the measurement traces and therefore assign the lifetime of the highest θ for which we still obtain a result. b) Detection error $\epsilon_{10}^{\text{tom}}$ (blue dots) and $\epsilon_{01}^{\text{tom}}$ (red dots). We assume that the lifetimes and detection errors are symmetric around $\theta = 0$.

6. We show in section 5.1.3 that we expect a symmetric Q function $Q(\theta, \phi) = Q(-\theta, \phi)$. We therefore also expect symmetric lifetimes.

4.3.4. Experimental results

With the method described in the last section, we have created entangled states of three different atom numbers and measured their Q function on 45 points along a cut through the pole of the Bloch sphere (see figure 4.8). The results of these measurements are presented in the following.

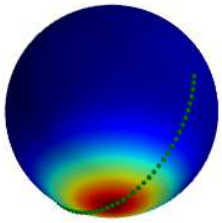

Figure 4.8.: Measurement points of the Q function on the Bloch sphere. We measure the Q function at 45 different angles $(\theta, \phi = 0)$ along one polar cut. The distance $\Delta\theta$ between the measurement points is varied according to the atom number of the state. The state in this image contains $N = 12$ atoms, for which $\Delta\theta = 0.13$.

4.3.4.a. Q function of the Coherent spin state

Every fifth experimental cycle, the W state preparation is omitted and the tomography is performed directly after the 25 µs light pulse that verifies if all the atoms are in $|0\rangle$. This way, we perform a tomography on a coherent state, which we can use to infer the number of atoms in the corresponding W state.

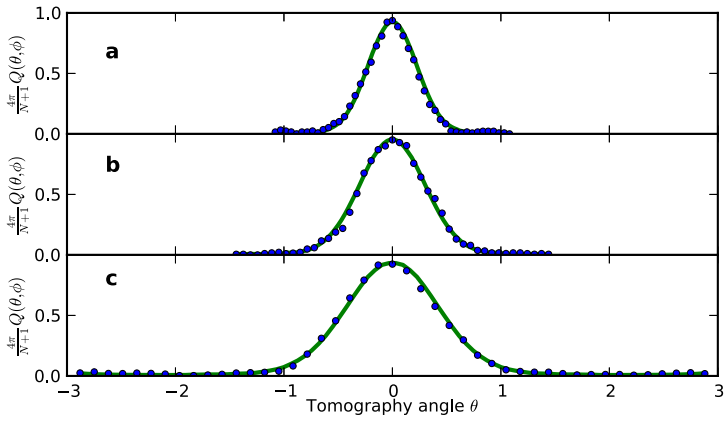

Figure 4.9.: Measured Q function of the prepared coherent states (blue points) and a fit from which we infer the atom number (green curve). We find that a)b)c) correspond to a mean atom number $N = 41, 23, 12$.

Figure 4.9 shows the tomography of the three prepared coherent states. Each data point corresponds to approximately 75 measurements. The curves fit well to the expected $\cos(\theta/2)^{2N}$ function, which gives us the mean atom number $N = 41, 23, 12$ (green curve). While it is easy to infer the mean atom number, the curves contain very little information on the spread of the atom number. However, we can deduce it from the way the atom number is prepared: In a worst case assumption, we assume that due to the many scattering events during the atom number preparation, the total atom number N_{tot} is spread over all three Zeeman levels in the $F = 1$ manifold. In this process, the population ratio of the Zeeman levels depends on the polarization of the probe and dipole beam and the magnetic field in the cavity. It is therefore difficult to calculate, but we can obtain it directly for the state $|0\rangle$ as $p = N/N_{\mathrm{tot}}$. This means that we can assume that the atom number of the state N_k follows a Binomial distribution

$$\mathcal{B}(N_k; N_{\mathrm{tot}}, p) = \binom{N_{\mathrm{tot}}}{N_k} p^{N_k} (1-p)^{N_{\mathrm{tot}}-N_k} \tag{4.20}$$

The standard deviation of $\mathcal{B}(N_k; N_{\mathrm{tot}}, p)$ is $\sigma = \sqrt{N_{\mathrm{tot}}\, p\, (1-p)}$ and we therefore obtain $\sigma = 4.2, 3.6, 2.8$ for the mean atom numbers $N = 41, 23, 12$.

4.3.4.b. Q function of the W state

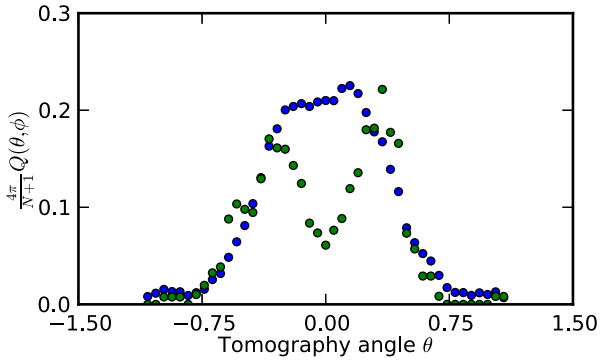

Figure 4.10.: Measured Q function of the prepared W state for $N = 41$. The blue points show all successful experimental runs, while the green points only show runs for which $R \geq 11$.

Figure 4.10 shows the tomography of the W state for $N = 41$. The blue points are obtained using every successful run (i.e. every run where $T = 0$, $R \geq 4$) while the green points only show experimental runs where the counts in reflection lie above a higher threshold $R_{\mathrm{prep}} = 11$. In these curves, the characteristic dip at $Q(\theta = 0)$ for the W state becomes visible.

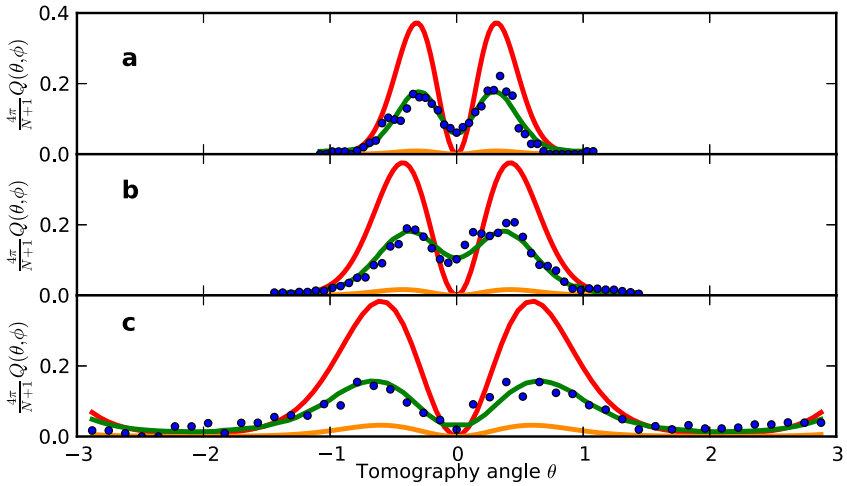

Figure 4.11.: Measured Q function of the prepared W states (blue points) and the Q function from the reconstructed density matrices (green curve, see section 5.1.3). The additional curves are the calculated Q functions of the state $|1_N\rangle$ (red curve) and of the state $|\psi_{\mathrm{sc}}\rangle$ (orange curve). The curves in a)b)c) correspond to a mean atom number N = 41, 23, 12.

Figure 4.11 shows the tomography curves for the W states with N = 41, 23, 12 and a threshold R_{prep} = 11, 10, 12 which maximizes the fidelity [7]. For comparison, we also plot the Q function of the perfect W state $|1_N\rangle$ (red curve) and of the state $|\psi_{\mathrm{sc}}\rangle$ (orange curve, cf. (4.18)) with the same atom number. We see that the contrast of the experimental data is reduced with respect to the red curve. This is due to imperfect preparation of the ensemble, scattering events during the state preparation and decoherence [8]. Furthermore, the dip of the Q function does not go down to zero. We can directly read out the contribution of the initial coherent state $|0_N\rangle$ to the prepared state as the amplitude of the Q function at $\theta = 0$. Nonetheless, the experimental data can be clearly distinguished from the Q function of a state where the atom in $|1\rangle$ is well-defined.

We also want to compare the results of the tomography measurement to the Q function we expect due to our state preparation method, which is not exactly the Q function of the state $|1_N\rangle$. We therefore revisit the W state preparation scheme and depict the Q function of the atomic state during the different experimental stages (see figure 4.12):

7. The influence of R_{prep} on the fidelity as well as the selection criterion for a specific value of R_{prep} are presented in section 5.2

8. The fidelity limiting factors are discussed in detail in section 5.2.

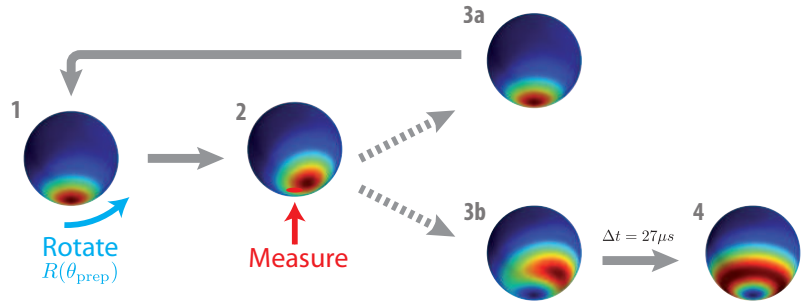

Figure 4.12.: The Q function of the atomic state during the consecutive steps of the W state preparation in the case of $N = 12$ atoms. The details are described in the main text.

The atoms are initially in $|0_N\rangle$, which corresponds to a Q function centered around the south pole (1). A microwave pulse $R(\theta_{\text{prep}})$ weakly excites the ensemble, which rotates the coherent state on the Bloch sphere by the angle θ_{prep}. The following QND measurement (2) either projects the state back to $|0_N\rangle$, in which case we repeat the preparation sequence (3a) or onto the state $|\xi\rangle$:

$$|\xi\rangle \equiv c(\mathbb{1} - |0_N\rangle\langle 0_N|)\,|\theta_{\text{prep}}\rangle \tag{4.21}$$

where c is a normalization factor and $|\theta_{\text{prep}}\rangle \equiv R(\theta_{\text{prep}})\,|0_N\rangle$ the state after the MW rotation. This results in a ring-shaped structure which has a big overlap with the W state. However, the created state is highly asymmetric due to coherent contributions of higher order Dicke states, which have also been populated by the MW pulse[9] (3b).

In contrary to the expected Q function, the experimental curves are all rotationally symmetric: $Q(\theta,\phi) = Q(-\theta,\phi)$. We attribute this to homogeneous dephasing of the atomic spins with respect to the MW due to an unstable magnetic field. The field drifts by more than 20 mG during the acquisition time of the experiment (several weeks). As we encode our qubit states $|0\rangle$ and $|1\rangle$ in the magnetically sensitive states $|F = 1, m_F = 1\rangle$ and $|F = 2, m_F = 2\rangle$, this leads to a drift of the transition frequency by

$$\Delta\omega_{\text{HF}} > 2\pi \cdot 2.1^{\text{MHz}}/_{\text{G}} \cdot 20\,\text{mG} = 42\,\text{kHz} \tag{4.22}$$

During the time Δt between the state creation and its tomography, the state evolves freely. In the Bloch sphere picture, it precesses around the z axis with the angular frequency $\Delta\omega_{\text{HF}}$. In our case, $\Delta t = 27\,\mu\text{s}$, and the state can therefore undergo a complete circle, which averages out the information on the angle ϕ in the measurement of the Q function. As a result, we only measure Q functions which are symmetric around $\theta = 0$ (see figure 4.12 step 4).

We have confirmed this expectation by measuring the Q function $Q(\theta, \phi = \pi/2)$ along the orthogonal axis, which gives similar results (see figure 4.13). However, due to unstable experimental conditions and bad calibration, the contrast in these curves is reduced with respect to the first measurement shown in figure 4.11. This can for example be seen in the higher amplitude $Q(\theta = 0, \phi = \pi/2)$. Because of the dephasing, the measurement

9. A quantitative analysis of these contributions is given in section 5.2.

along the orthogonal axis $Q(\theta, \phi = \pi/2)$ does not contain any additional information and we do not consider it in the fidelity estimation.

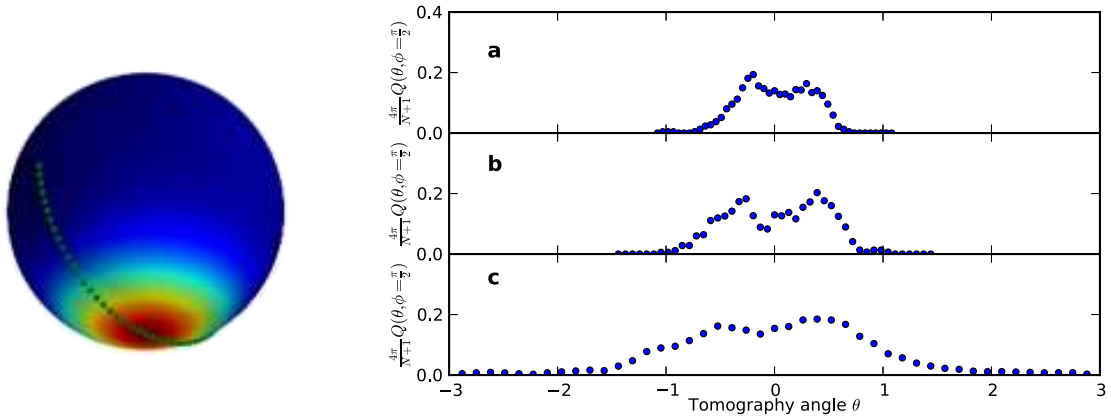

Figure 4.13.: Q function measurement on the orthogonal axis $(\theta, \phi = \pi/2)$. The image on the left shows the measurement points on the Bloch sphere. The curves a) b) c) on the right show the measured Q function for the mean atom numbers $N = 41, 23, 12$. This measurement, as well as the measurement on the orthogonal axis $(\theta, \phi = 0)$ shows a high degree of symmetry around $\theta = 0$.

4.4. Decoherence

After the target state has been prepared, it is subject to decoherence and the population in the state $|1_N\rangle$ decreases. We investigate the temporal evolution of this decoherence in an independent measurement and compare it to the predictions of a model which takes into account the differential light shift of the two qubit states in the optical dipole trap.

We measure the evolution of the Q function at the angles $(\pm\theta_{\max}, \phi = 0)$ as a function of τ, the time elapsed after the state is prepared. Precisely, we define τ as the time interval between the start of the preparation light pulse to the start of the tomography light pulse. τ is varied from $\tau_{\min} = 27\,\mu s$ [10] to $\tau = 177\,\mu s$. The measurement angles are $\theta_{\max} = 0.29, 0.39, 0.65$ for $N = 41, 23, 12$, which corresponds to the maxima of the Q function shown in figure 4.11. As for the measurements in section 4.3.4, we assume the Q function to be rotationally symmetric and we depict the average of the Q function at positive and negative angle $\overline{Q}(\theta_{\max}) = 1/2[Q(-\theta_{\max}) + Q(\theta_{\max})]$. At $\tau_{\min}$, we also measure $Q(\theta = 0)$, from which we can infer the state's population in the coherent state $|0_N\rangle$. Figure 4.14 shows the result of this measurement for different atom numbers. We see that the contrast of the Q function is halved at approximately $\tau = 80\,\mu s$.

10. This is the minimum time interval possible with our setup. It is comprised of the cavity measurement for the state preparation with a duration of 20 µs and the real-time controller calculation time of 7 µs.

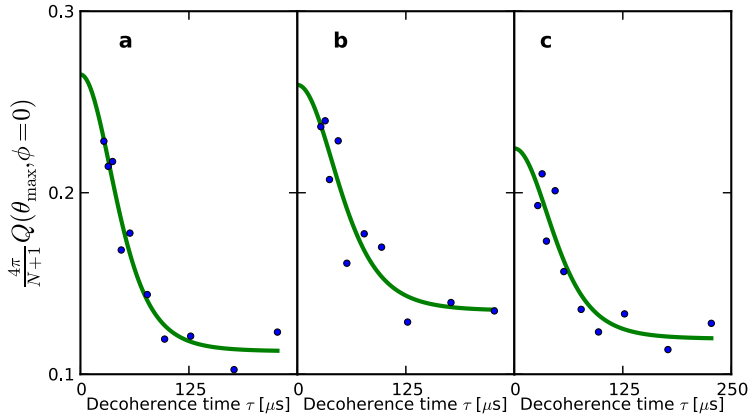

Figure 4.14.: Decoherence measurement of the W state. a)b)c) show the reduction of the Q function for $N = 41, 23, 12$, respectively. The green curve is a fit to the data, based on a model taking into account the finite temperature in the trap.

This effect can be explained as a consequence of the finite temperature of the atomic ensemble in the optical dipole trap. Our calculations follow [102]:

The potential of the dipole trap is the light shift experienced by the atoms in the ground state $5\,^2S_{1/2}$ and proportional to the detuning between the light and the atomic transition Δ and the light intensity I:

$$U_0(\Delta, I) = \frac{\hbar\Gamma^2}{8I_0}\frac{I}{\Delta} \tag{4.23}$$

where $\Gamma = 2\pi \cdot 6\,\mathrm{MHz}$ is the natural linewidth of the D_2 line and $I_0 = 3.6\,\mathrm{mW/cm^2}$ is the corresponding saturation intensity. The atoms in $|0\rangle$ and $|1\rangle$ are detuned by the hyperfine splitting $\Delta_{HF} = 6.8\,\mathrm{GHz}$ and therefore experience a slightly different light shift. When we consider an effective detuning Δ_{eff} with $\Delta_{\mathrm{eff}}^{-1} = (\Delta_1^{-1} + 2\Delta_2^{-1})/3$ with Δ_1 (Δ_2) being the detuning from the D_1 (D_2) line, we can approximate the differential light shift between the atoms in $|0\rangle$ and $|1\rangle$ as

$$\hbar\delta = U_0(\Delta_{\mathrm{eff}}) - U_0(\Delta_{\mathrm{eff}} + \Delta_{\mathrm{HF}}). \tag{4.24}$$

Since $\Delta_{\mathrm{HF}} \ll \Delta_{\mathrm{eff}}$, we can assume that the differential light shift is proportional to the total light shift:

$$\hbar\delta = \eta U_0 \qquad \eta = \frac{\Delta_{\mathrm{HF}}}{\Delta_{\mathrm{eff}}} \tag{4.25}$$

On average, an atom with higher energy E experiences a lower dipole light intensity and thus a lower differential light shift. Two atoms with different energies therefore have a different detuning with respect to the MW and accumulate a phase difference when they precess on the Bloch sphere. We approximate the dipole trap by an harmonic potential, for which the virial theorem states that the potential energy U_0 is on average half the total energy E. The phase difference then becomes

$$\Delta\phi = \eta\frac{\Delta U_0}{\hbar}t = \eta\frac{\Delta E}{2\hbar}t \tag{4.26}$$

What is the influence of this phase spread on the population of the W state?

A perfect W state is characterized by the fact that there is a fixed phase relation between all the terms of the superposition (cf. (4.3)). After time τ, the atoms in $|1\rangle$ have accumulated a phase $\phi_\tau(E)$ dependent on their energy in the trap:

$$|1_N(\tau)\rangle = \frac{1}{\sqrt{N}}(\mathrm{e}^{-i\phi_\tau(E_1)}|10\ldots0\rangle + \mathrm{e}^{-i\phi_\tau(E_2)}|010\ldots0\rangle + \ldots + \mathrm{e}^{-i\phi_\tau(E_N)}|00\ldots1\rangle) \quad (4.27)$$

The overlap with the initial state therefore evolves as:

$$|\langle 1_N|1_N(\tau)\rangle|^2 = |\frac{1}{N}\sum_{j=1}^{N}\mathrm{e}^{-i\phi_\tau(E_j)}|^2 \quad (4.28)$$

The average evolution of the overlap then is:

$$\begin{aligned}\langle|\langle 1_N|1_N(\tau)\rangle|^2\rangle &= \langle|\frac{1}{N}\sum_{l=1}^{N}\mathrm{e}^{-i\phi_\tau(E_l)}|^2\rangle \\ &= \frac{1}{N} + \frac{1}{N^2}\sum_{k,l}\langle\mathrm{e}^{i(\phi_\tau(E_k)-\phi_\tau(E_l))}\rangle \\ &= \frac{1}{N} + \frac{N(N-1)}{N^2}\langle\mathrm{e}^{i(\phi_\tau(E_1)-\phi_\tau(E_2))}\rangle \\ &= \frac{1}{N} + \frac{N(N-1)}{N^2}|\langle\mathrm{e}^{i(\phi_\tau(E_1))}\rangle|^2 \equiv \frac{1}{N} + c(\tau)\end{aligned} \quad (4.29)$$

The phase spread of an ensemble of atoms reflects the energy distribution of the atoms in the trap. In our case, this is a three-dimensional Boltzmann distribution with probability density [102]

$$p(E) = \frac{\beta^3 E^2}{2}\exp[-\beta E] \qquad \beta = \frac{1}{k_B T}. \quad (4.30)$$

The average phase is thus calculated by iterating over the trap energy, weighted by the energy population:

$$\begin{aligned}|\langle\mathrm{e}^{i\phi_\tau(E_1)}\rangle|^2 &= |\int_0^\infty \mathrm{e}^{-i\frac{\eta E}{2\hbar}\tau}\frac{\beta^3}{2}E^2\mathrm{e}^{\beta E}\mathrm{d}E|^2 \\ &= \left|\frac{\beta^3}{(\beta + \frac{i\tau\eta}{2\hbar})^3}\right|^2 \\ &= \frac{64\beta^6\hbar^6}{(4\beta^2\hbar^2 + \eta^2\tau^2)^3}\end{aligned} \quad (4.31)$$

We see that for long times, the overlap drops to $1/N$, which reflects the fact that the initial W state decoheres into the statistical mixture $\{|100\ldots\rangle, |010\ldots\rangle, \ldots\}$ with one localized excitation.

We can infer the trap temperature from the decoherence measurement by fitting the result of (4.29) to our data. We model the decoherence using a state ρ_{fit} which only

has populations in the coherent state ρ_{00}, the W state ρ_{11} and the non-symmetric subspace [11]. The population ρ_{00} does not decay and the population ρ_{11} decoheres according to (4.29):

$$\rho_{11}(\tau) = \left(\frac{1}{\mathcal{N}} + c(\tau)\right) \rho_{11}(0) \tag{4.32}$$

We compute the expected value of the Q function at angle $\theta_{\max}$

$$Q(\theta_{\max})|_\tau = \frac{N+1}{4\pi} \langle \theta_{\max}| \rho_{\text{fit}}(\tau) |\theta_{\max}\rangle \tag{4.33}$$

and fit it to the data with the following fit parameters:

- $\rho_{11}(0)$, the initial population in the $|1_N\rangle$ state
- β, the temperature
- $\frac{1}{\mathcal{N}}$, the remaining population in $|1_N\rangle$ for $\tau \to \infty$

The green curves in figure 4.14 show the fit and figure 4.15 shows the offset $1/\mathcal{N}$ obtained from the fit, compared to the expected $1/N$ dependence. We see that the model reproduces well the trend of the data. From the fit, we obtain a trap temperature $k_B T = U/6$, which is the expected order of magnitude for an atomic ensemble heated up in a finite depth trap.

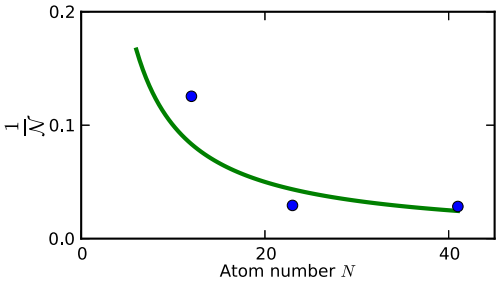

Figure 4.15.: Remnant fidelity $\frac{1}{\mathcal{N}}$ at $\tau \to \infty$ for the W states with three different atom numbers. The values are obtained from the fit to the decoherence measurement shown in figure 4.14. The green curve shows the expected $1/N$ dependence.

The fit also allows us to infer the upper limit of the population ρ_{11} due to decoherence. We find that for $\tau_{\min} = 27\,\mu\text{s}$, we are limited to $\rho_{11} = 0.78, 0.85, 0.91$ for $N = 41, 23, 12$. There are several ways to increase this limit: A straight-forward approach consists in reducing $\tau_{\min}$. This can be done by using a faster real-time controller system or by increasing the probe light intensity to allow for a shorter detection time t_{prep}. However, a technical limit is reached at $t_{\text{prep}} = 2\,\mu\text{s}$ when the counter efficiencies of the SPCMs start to decrease because of too high count rates. Another approach is to increase the decoherence time. This can be done by decreasing the differential light shift (e.g. by choosing a longer trapping wavelength) or by decreasing the trap temperature (e.g. by using a more shallow dipole trap).

11. We do not assume any populations in the higher-order Dicke states $|n_N\rangle, n \geq 2$. We will see in chapter 5 that this assumption is justified.

4.5. Conclusion

In this chapter, we have presented a novel method for the generation of W states, based on weak collective excitation and a QND measurement. We have also introduced the direct measurement of the Husimi Q function as a technique for the full characterization of a multiparticle state with the help of a cavity. We have shown that this tomography measurement gives access to the symmetric part of the states' density matrix.

With these two methods, we have generated W states with atom numbers $N = 41, 23, 12$ and have measured out their Husimi Q function along two orthogonal polar cuts of the Bloch sphere. The atom number has been inferred in a tomography measurement of the corresponding coherent spin states.

Furthermore, we have analyzed the state decoherence. The temporal evolution of the prepared state can be well explained by a model assuming an atomic cloud of finite temperature in a dipole trap.

5. State reconstruction and verification of entanglement

In the last chapter, we have measured the Q function of experimentally created states. In principle, this is sufficient to completely characterize them. However, there are interesting properties that we cannot directly obtain from the Q function, such as the fidelity $\mathcal{F}$, being defined as the overlap of the created state with the target state $|1_N\rangle$:

$$\mathcal{F} = \langle 1_N | \rho | 1_N \rangle \tag{5.1}$$

We therefore present methods to retrieve a state's density matrix from the measured Q function. This allows us to obtain $\mathcal{F}$ and to quantitatively study the fidelity limiting factors of our entanglement scheme. Finally, we introduce an entanglement criterion based on the state's populations in $|0_N\rangle$ and $|1_N\rangle$ and show that our experimentally created state with the highest fidelity contains at least 13 entangled atoms.

5.1. Quantum state reconstruction

The laws of quantum mechanics pose some difficulties on the reconstruction of the state of a quantum system (described by its density matrix ρ). A measurement performed on the state in general modifies the state itself [103] and the no-cloning theorem forbids to generate copies of a quantum state [104].

To reconstruct the density matrix despite these constraints, an experimenter would prepare N samples of the system in the same state ρ and would perform M measurements $|y_i\rangle\langle y_i|, i = 1, ..., M$ on them. The state ρ can be found in $|y_i\rangle$ with probability p_j:

$$p_j = \langle y_i | \rho | y_i \rangle \tag{5.2}$$

If the M measurements were complete

$$\sum |y_i\rangle\langle y_i| = \mathbb{1} \tag{5.3}$$

and if the number of measurements was high enough to infer the probabilities p_j with sufficient precision, ρ could be calculated by inverting the linear relation (5.2) for all i. In our experimental situation, this would correspond to measuring $Q(\theta, \phi)$ at every angle (θ, ϕ) on the Bloch sphere and to perform an infinite number of measurements at each angle to obtain the expectation value $\langle \theta, \phi | \rho | \theta, \phi \rangle$. This, of course, is practically impossible. In reality, we have to infer the density matrix from insufficient data via some form of reconstruction algorithm [105, 106]. In the following, we introduce two of the most common techniques, the "Maximum Likelihood" reconstruction (ML) [107] and the "Maximum Entropy" reconstruction (ME) [108]. We also describe an additional reconstruction technique, which takes into account some characteristics of our experimental situation. As an example, we use the different methods to reconstruct the experimental dataset with $N = 41$ and a threshold of the reflection counts in the state

preparation measurement $R_{\text{prep}} \geq 11$. We will find that this is the dataset with the highest population in the target state $|1_N\rangle$.

5.1.1. Maximum Likelihood reconstruction

Principle

The maximum likelihood reconstruction (ML) aims at answering the question "What quantum state seems to be most likely, given the outcome of the measurements?". Any density matrix ρ assigns probabilities for a given measurement on the basis of (5.2). It is therefore possible to assign an overall probability for a given density matrix to reproduce the ensemble of measurement outcomes $\{n_j\}$:

$$\mathcal{L}'(\rho) = \frac{N!}{\prod_i n_i!} \prod_j \langle y_j|\rho|y_j\rangle^{n_j} \tag{5.4}$$

with n_j being the number of detections of a particular outcome $|y_j\rangle$. In the case of our Q function measurement, for each tomography angle there are only two possible experimental outcomes: 1, corresponding to high transmission, or 0, corresponding to low transmission. The different observables $|y_j\rangle\langle y_j|$ therefore correspond to measurements $|\theta_j,\phi_j\rangle\langle\theta_j,\phi_j|$ $(1-|\theta_j,\phi_j\rangle\langle\theta_j,\phi_j|)$ of the Q function at different angles (θ_j,ϕ_j) and we obtain n_j^1 (n_j^0) times the outcome 1 (0). The forefactor in (5.4) can be omitted, since it does not alter the result. The ML therefore amounts to maximizing the likelihood functional $\mathcal{L}(\rho)$:

$$\mathcal{L}(\rho) = \prod_j \langle\theta_j,\phi_j|\rho|\theta_j,\phi_j\rangle^{f_j^1} \cdot (1-\langle\theta_j,\phi_j|\rho|\theta_j,\phi_j\rangle)^{f_j^0} \tag{5.5}$$

with $f_j^k = {}^{n_j^k}/_N$.

The density matrix ρ_m for which (5.5) is maximal can be found in an iterative algorithm:

We introduce the operator $M(\rho)$ [106]:

$$M(\rho) = \sum_j \frac{f_j^1}{p_j^1}|\theta_j,\phi_j\rangle\langle\theta_j,\phi_j| + \frac{f_j^0}{p_j^0}(1-|\theta_j,\phi_j\rangle\langle\theta_j,\phi_j|). \tag{5.6}$$

For the density matrix ρ_m, which is most likely to reproduce the given results, we know that $f_j^k \propto p_j^k$ and therefore

$$M(\rho_m)\rho_m M(\rho_m) \propto \rho_m \tag{5.7}$$

We can thus start with a density matrix $\rho = {}^{\mathbb{1}}/_{\text{Tr}[\mathbb{1}]}$ and calculate consecutive matrices via the iterative step

$$\rho^{(k+1)} = \mathcal{N}[M(\rho^{(k)})\rho^{(k)}M(\rho^{(k)})] \tag{5.8}$$

where $\mathcal{N}[]$ denotes the normalization to a unitary trace. In each iteration step, the likelihood monotonically increases and the density matrix asymptotically approaches ρ_m.

Reconstruction of the experimental data

The result of the reconstruction shows that the population in the higher order Dicke states $|n_N\rangle$ with $N \geq 3$ is negligible and we therefore omit them in the following (this is also true for the other reconstruction techniques). This means that the symmetric part of the quantum state is fully described by the matrix

$$\rho = \begin{pmatrix} \rho_{00} & \rho_{01} & \rho_{02} \\ \rho_{10} & \rho_{11} & \rho_{12} \\ \rho_{20} & \rho_{21} & \rho_{22} \end{pmatrix} \tag{5.9}$$

containing the Dicke states $|0_N\rangle$, $|1_N\rangle$, $|2_N\rangle$, and coherences between them. The matrix ρ^{ML} with the highest likelihood is:

$$\rho^{\mathrm{ML}} = \begin{pmatrix} 0.03 & -0.02i & -0.01i \\ 0.02i & 0.43 & 0.11 + 0.02i \\ 0.01i & 0.11 - 0.02i & 0.03 \end{pmatrix} \tag{5.10}$$

We see that the trace $\mathrm{Tr}[\rho^{\mathrm{ML}}] = 0.49$ is smaller than 1. This means that the rest of the population is in the non-symmetric subspace. Figure 5.1 shows the Q function of ρ^{ML} depicted on the Bloch sphere as well as along one polar cut, together with the experimental data.

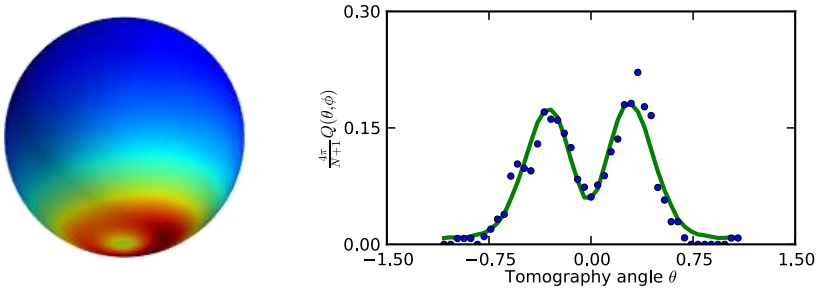

Figure 5.1.: Result of the state reconstruction with the ML method. The matrix ρ^{ML} is depicted on the Bloch sphere (left) and along a the polar cut $Q(\theta, \phi = 0)$ (green curve), together with the experimental data (blue dots).

5.1.2. Maximum Entropy reconstruction

Principle

We consider the case where we have measured the Q function along k different angles (θ_j, ϕ_j), $j = 1, \ldots k$, which means that we have obtained the expectation values $\langle j \rangle$ of a set of observables $\hat{j} \equiv |\theta_j, \phi_j\rangle \langle \theta_j, \phi_j|$. We know that the actual density matrix ρ_0 which was responsible for the measurement outcomes, fulfills the equations

$$\begin{aligned} \mathrm{Tr}[\rho_0] &= \mathbb{1} \\ \langle j \rangle &= \mathrm{Tr}[\rho_0 \hat{j}] \end{aligned} \tag{5.11}$$

However, there might be a lot of density matrices $\{\rho\}$ which fulfil (5.11). We therefore have to choose one matrix from the ensemble $\{\rho\}$ in an unbiased manner. One possibility would be to choose the matrix which reflects our level of observation (i.e. our degree of knowledge on the system) without supposing any additional knowledge. This corresponds to choosing the density matrix ρ_m with the highest entropy $S(\rho_m)$ out of $\{\rho\}$ [108]. The entropy is defined as

$$S(\rho) = -\mathrm{Tr}[\rho \ln(\rho)] \tag{5.12}$$

In order to find the matrix ρ_m, for which (5.12) is maximized, we can use the method of Lagrange multipliers [109]:

We define the functional

$$\mathcal{L}(\rho, \lambda_i) = -\mathrm{Tr}[\rho \ln(\rho)] + \sum_j \lambda_j (\mathrm{Tr}[\rho \hat{j}] - \langle j \rangle) + \lambda_0 (\mathrm{Tr}[\rho] - 1) \tag{5.13}$$

and find its extremum by finding the zero crossings of the partial derivatives

$$\frac{\partial \mathcal{L}}{\partial \rho} = 0 \tag{5.14}$$

$$\frac{\partial \mathcal{L}}{\partial \lambda_i} = 0 \tag{5.15}$$

The solution of (5.14) simply is

$$\rho_m = \frac{1}{Z} \exp[-\sum_j \lambda_j \hat{j}] \qquad Z = \mathrm{Tr}[\mathrm{e}^{-\sum_j \lambda_j \hat{j}}] \tag{5.16}$$

Putting (5.16) in (5.13) and solving (5.15) gives:

$$\mathrm{Tr}[\rho_m \hat{j}] - \langle j \rangle = 0 \qquad \forall j \tag{5.17}$$

In our case, the number of measurements per tomography angle (θ_j, ϕ_j) is not sufficient to precisely infer the expectation values $\langle j \rangle$. (5.17) is therefore altered to minimize the difference χ between the measurement outcomes p_j and the expectation values $\langle j \rangle$:

$$\chi^2 = \sum_j \left(\mathrm{Tr}[\rho_m \hat{j}] - \langle j \rangle \right)^2 \tag{5.18}$$

The fact that we maximize the entropy of the density matrix means that we do not assume any knowledge about observables that have not been measured. The ME method is therefore a good choice for experiments where measurements have been performed only on an incomplete set of observables. This is certainly the case in our Q function measurement, where we infer the density matrix from a single polar cut on the Bloch sphere. We therefore expect the ME method to reconstruct the density matrix of our state more faithfully than the ML method.

Reconstruction of the experimental data
From the reconstruction with the ME method, we obtain:

$$\rho^{\mathrm{ME}} = \begin{pmatrix} 0.03 & -0.01i & 0.00 \\ 0.01i & 0.46 & 0.12 - 0.01i \\ 0.00 & 0.12 + 0.01i & 0.03 \end{pmatrix} \tag{5.19}$$

The ME method gives a slightly higher fidelity of the W state with respect to the ML method. When we plot the Q function of ρ^{ME} on the Bloch sphere (see figure 5.2), we see that both reconstruction methods agree remarkably well. This increases our confidence in the reconstruction result, since it means that the most likely density matrix is close to the one with the highest entropy.

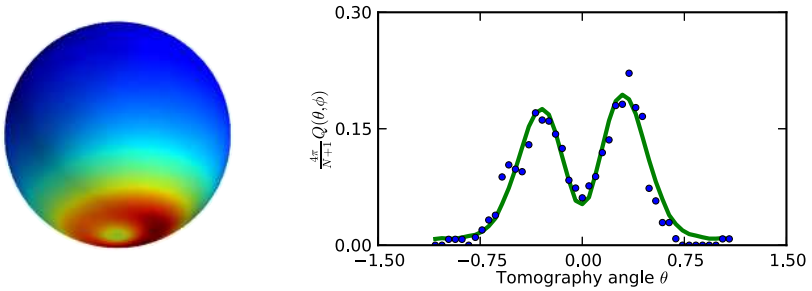

Figure 5.2.: Result of the experimental state reconstruction with the ME method. The matrix ρ^{ME} is depicted on the Bloch sphere (left) and along a the polar cut $Q(\theta, \phi = 0)$ (green curve), together with the experimental data (blue dots).

5.1.3. Reconstruction of a diagonal density matrix

The states reconstructed with the ME and ML method show a rotational asymmetry. However, as we have already mentioned in section 4.3.4.b, we expect a rotationally symmetric Q function: During the time Δt between the state creation and its tomography, the atoms are exposed to a fluctuating magnetic field, which shifts the transition frequency between the states $|0\rangle$ and $|1\rangle$. Thus, after having been created, the multiparticle state precesses on the multiparticle Bloch sphere with the detuning frequency $\Delta\omega_{\mathrm{HF}}$ between the atomic levels and the microwave. In our case, $\Delta\omega_{\mathrm{HF}} > {}^{2\pi}/_{\Delta t}$ and we therefore measure a rotationally symmetric Q function, averaged over the azimuth angle ϕ.

This rotation has a consequence on the density matrix of the state. When we write the Q function in terms of the entries of ρ and express ρ in the basis of Dicke states [99], we see that a rotationally symmetric Q function is equivalent to a density matrix

ρ without off-diagonal elements:

$$\begin{aligned} Q(\theta) &\equiv \int Q(\theta,\phi)\,\mathrm{d}\phi \\ &= \int \sum_k \sum_l \rho_{kl} \cos(\theta/2)^{N-k-l} \sin(\theta/2)^{N+k+l} \mathrm{e}^{-i(k-l)\phi} \binom{N}{k}^{1/2} \binom{N}{l}^{1/2} \mathrm{d}\phi \\ &= \sum_k \rho_{kk} \cos(\theta/2)^{N-2k} \sin(\theta/2)^{N+2k} \binom{N}{k} \end{aligned} \tag{5.20}$$

This means that the B-field fluctuations cause the coherences between the basis states to disappear.

Principle

Based on this experimental fact, we use a third reconstruction method that only infers diagonal density matrices. The reconstruction thus simplifies considerably and is reduced to a "linear and positive" (LP) problem, which we can solve in a Maximum Likelihood approach [110, 105]:

In the experiment, we perform measurements at k different angles (θ_j, ϕ_j), $j = 1 \ldots k$ and obtain n_j^0 (n_j^1) times the measurement outcome 0 (1). For a given population in the Dicke state $|i_N\rangle = \rho_{ii}$ and a given angle (θ_j, ϕ_j), we calculate the probability $p_i^1 = \tilde{M}_j^i \rho_{ii}$ to obtain the outcome 1 and maximize the (log-) likelihood function

$$\mathcal{L}(\boldsymbol{\rho}) = \sum_{j=1}^{k} n_j^1 \log \tilde{M}_j^i \rho_{ii} + n_j^0 \log(1 - \tilde{M}_j^i \rho_{ii}) \tag{5.21}$$

in the iterative algorithm [111]

$$\rho_{ii}^{(n)} = \rho_{ii}^{(n-1)} \sum_{j=1}^{k} \frac{\tilde{M}_j^i n_j^1}{p_j^1} + \frac{1 - \tilde{M}_j^i n_j^1}{1 - p_j^1} \tag{5.22}$$

As a result, we obtain a "density vector" $\boldsymbol{\rho}$, consisting only of the diagonal elements of the density matrix ρ. This reconstruction technique reflects the physical situation in our experiment and comprises aspects of both the ME and ML method: On the one hand, the resulting diagonal density matrix is obtained in maximizing a likelihood function and on the other hand, it has maximum entropy compared to density matrices with the same state population.

Another advantage of this technique is the reduced number of elements, which have to be obtained from the dataset. The reconstruction technique is therefore very robust.

Reconstruction of the experimental data

The matrix with the highest likelihood to reproduce the given dataset is

$$\rho^{LP} = \begin{pmatrix} 0.03 & 0 & 0 \\ 0 & 0.42 & 0 \\ 0 & 0 & 0 \end{pmatrix} \tag{5.23}$$

This means that the symmetric part of the quantum state is fully described by the vector $\boldsymbol{\rho} = [\rho_{00}, \rho_{11}, \rho_{11}] = [0.03, 0.42, 0.00]$ containing the population in the Dicke states [$|0_{41}\rangle$, $|1_{41}\rangle$, $|2_{41}\rangle$]. The rest of the population is in the non-symmetric subspace, $\mathrm{Tr}[\rho_{\mathrm{n.sym.}}] = 1 - 0.03 - 0.42 = 0.55$. Figure 5.3 shows the expected Q function from the reconstructed density matrix ρ^{LP}. Since the LP technique assumes no coherence between the Dicke states, the reconstructed state is rotationally symmetric on the Bloch sphere.

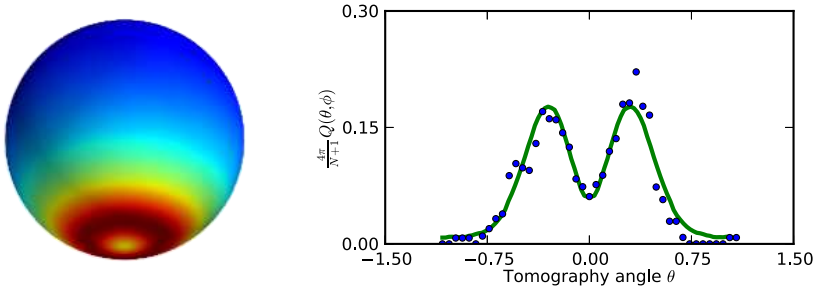

Figure 5.3.: Result of the experimental state reconstruction with the LP method. The matrix ρ^{LP} is depicted on the Bloch sphere (left) and along a the polar cut $Q(\theta, \phi = 0)$ (green curve), together with the experimental data (blue dots).

5.1.4. Error estimation of the state reconstruction

We would like to estimate the errors of our state reconstruction. We can identify different error sources that all the three different reconstruction techniques have in common: Errors due to the finite number of measurements per tomography angle, due to the detection error of the tomography measurement and due to the fact that we only consider a single, well-defined atom number in the reconstruction. For the LP technique, we have to take into account an additional error which stems from the fact that we neglect off-diagonal matrix elements.

Finite number of measurements and detection error

We estimate this error using a bootstrapping method [112]: We compute "artificial" datasets of Q function measurements with the probability distribution given by the measured values of the Q function and the same number of measurements as in the experimental dataset. We then reconstruct these datasets and obtain a distribution for each entry of the density matrix with a certain mean and spread.

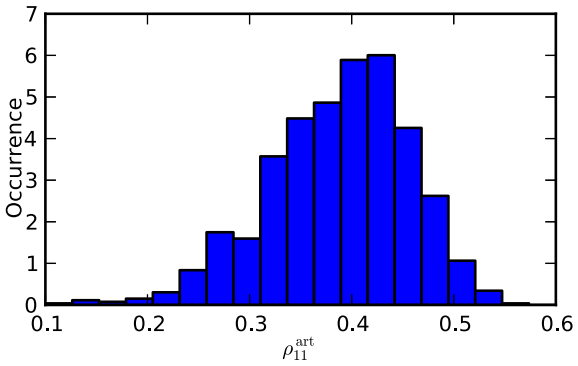

Figure 5.4.: Distribution of the fidelity ρ_{11} from a reconstruction with the LP method of 1000 artificial datasets with a probability distribution given by the measured values of the Q function. We obtain such distributions also for the populations ρ_{00} and ρ_{22} and can assign a systematic error and a standard deviation for ρ^{LP}.

As an example, figure 5.4 shows the population in the $|1_{41}\rangle$ state for 1000 artificial datasets, reconstructed with the LP method. The systematic error is calculated as the difference between the mean of this distribution and the population ρ_{11}, inferred from the experimental dataset. The (asymmetric) statistical error is calculated as the standard deviation of the spread of the distribution.

Reconstruction with a single atom number

The experimentally created state has a certain atom number distribution $\sigma(N)$, which has been calculated in a worst case assumption in section 4.3.4.a. However, our state reconstruction assumes only a single atom number. To obtain the resulting systematic error, we calculate the Q function of a density matrix ρ_m, given by a statistical mixture of density matrices ρ_k, all with the same state populations but with different atom number. We assume a binomially distributed atom number N_k with mean N and standard deviation $\sigma(N)$. Figure 5.5 shows such a Q function for $N = 41$ and $\sigma(N) = 4.2$ (green "+" markers). We can compare it with the tomography curve calculated from the same state populations, but composed of only one atom number $N = 41$ (blue "x" markers). The two Q functions only differ slightly. When we reconstruct the green dataset with our reconstruction methods (supposing only one atom number), we find that the result is almost identical. For example, the population ρ_{11} is underestimated by less than 1%.

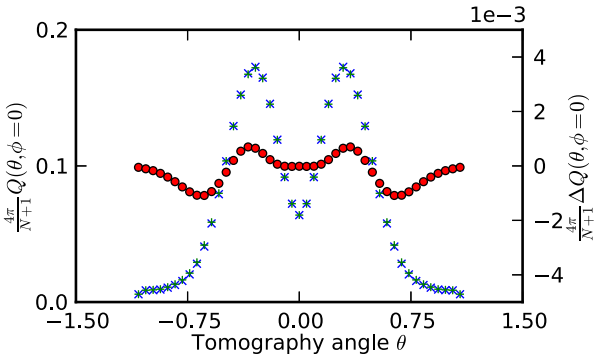

Figure 5.5.: Q function of a state with density matrix ρ^{LP} (see (5.23)) and a fixed atom number N=41 (blue "x" markers), compared to the Q function of a state with the same density matrix, but with a binomial distributed atom number with mean $N = 41$ and $\sigma = 4.2$ (green "+" markers). The two curves almost perfectly overlap. The red dots on the second y-axis show the difference between the two signals. It is always below $2 \cdot 10^{-3}$, which is well below the error of the tomography measurement.

Omission of off-diagonal matrix elements

The statistical error through the omission of off-diagonal elements only applies to matrices reconstructed with the LP method. We estimate it by creating random (3×3) density matrices $\{\rho_{\mathrm{rand}}\}$ with off-diagonal elements, representing the population in the states $|0_N\rangle$, $|1_N\rangle$ and $|2_N\rangle$ and coherences between them. For each ρ_{rand}, the likelihood to reproduce the experimental dataset is calculated. The mean populations and their spread is analyzed for the ensemble of density matrices with a likelihood that is higher than the one from ρ^{LP}. We obtain that we underestimate the population ρ_{11} by 4%. The deviation of the population ρ_{00} from the actual value is too small to assign an error.

Summary

Using the methods presented above, we assign systematic and statistical errors to the matrices ρ^{LP}, ρ^{ML} and ρ^{ME}, reconstructed with the three different reconstruction techniques. Here, we give the results for the dataset with the highest atom number and highest fidelity ($N = 41$, $R_{\mathrm{prep}} \geq 11$): The dominating error contribution is statistical

Method	ρ_{00}	ρ_{11}	ρ_{22}
LP	$0.03 - 0.01^{+0.02}_{-0.02}$	$0.42 + 0.01^{+0.06}_{-0.06}$	$0.00 + 0.00^{+0.06}_{-0.00}$
ML	$0.03 - 0.01^{+0.02}_{-0.02}$	$0.43 + 0.01^{+0.05}_{-0.04}$	$0.03 - 0.01^{+0.02}_{-0.01}$
ME	$0.03 + 0.00^{+0.02}_{-0.02}$	$0.46 + 0.03^{+0.07}_{-0.06}$	$0.03 - 0.03^{+0.07}_{-0.03}$

Table 5.1.: Dicke state populations and errors of the created state with $N = 41$, $R_{\mathrm{prep}} \geq 11$ for different reconstruction methods.

error due to a finite number of measurement points per tomography angle. The standard

deviation is 6% for the population in the target state $|1_N\rangle$.

We would like to stress the fact that the statistical error of any reconstruction method always leads to an underestimation of the population ρ_{11} and an overestimation of ρ_{00}. This ensures that we do not overestimate the degree of entanglement present in the system (see section 5.3.3).

In general, the results of the three different reconstruction methods agree very well. The LP technique gives the most conservative estimate of the population in the $|1_N\rangle$ state. We therefore only use this reconstruction method to analyze the experimentally created states with different atom numbers.

5.1.5. Results for different atom numbers

We analyze the data for the other atom numbers using the LP technique and also vary the reflection threshold R_{prep} of the preparation sequence. Figure 4.11 shows the Q function of the datasets for an R_{prep} which maximizes the population in the $|1_N\rangle$ state. We obtain R_{prep} = 11, 10, 12 for N = 41, 23, 12. It is dependent on the atom number, since the count rates T and R vary slightly with N. The populations in the Dicke states and the errors are given in table 5.2.

atom number	ρ_{00}	ρ_{11}	ρ_{22}
41	$0.03 - 0.01^{+0.02}_{-0.02}$	$0.42 + 0.01^{+0.06}_{-0.06}$	$0.00 + 0.00^{+0.06}_{-0.00}$
23	$0.08 - 0.02^{+0.02}_{-0.02}$	$0.37 + 0.03^{+0.04}_{-0.04}$	$0.00 + 0.00^{+0.04}_{-0.00}$
12	$0.00 + 0.00^{+0.02}_{-0.00}$	$0.31 + 0.02^{+0.09}_{-0.08}$	$0.14 - 0.01^{+0.07}_{-0.07}$

Table 5.2.: Dicke state populations and errors of the created states for different atom numbers.

The high populations in ρ_{22} for the state with 12 atoms indicate that - in contrary to the states with higher atom numbers - higher order Dicke states $|n_N\rangle$, $n > 2$ have to be taken into account in the reconstruction. We attribute this behavior to the fact that the Q functions of different Dicke states have higher overlap for a state containing less atoms.

Table 5.3 shows the result of the state reconstruction of the state with 12 atoms using different numbers of Dicke states. Indeed, we see that the populations are differently distributed when higher order Dicke states can contribute to the state. The state fidelity is the comparable to the fidelity obtained for higher order Dicke states. This shows that our entanglement scheme based on collective measurement is independent of N [1].

1. There is a fidelity limiting factor which scales linearly with the number of atoms (see section 5.2), but it is small compared to other effects.

No. of Dicke states	ρ_{00}	ρ_{11}	ρ_{22}	ρ_{33}	ρ_{44}	ρ_{55}
3	0.00	0.31	0.14			
4	0.00	0.36	0.00	0.08		
5	0.00	0.38	0.00	0.00	0.06	
6	0.00	0.38	0.00	0.03	0.00	0.04

Table 5.3.: Dicke state populations of the state with 12 atoms for a different number of Dicke states contributing to the state reconstruction.

5.2. Preparation errors and limits to the fidelity

In the following, we list the known effects that degrade the fidelity of the target state $|1_N\rangle$ and give a quantitative analysis for the state consisting of 41 atoms.

- The initial state is not in $|0_N\rangle$:
  When we start the W state preparation sequence with an initial state that is not in the symmetric subspace, we cannot obtain the final state $|1_N\rangle$. To make sure that the system is initially in the state $|0_N\rangle$, we probe the cavity during 25 µs and only continue if the measurement indicates that the system is in $|0_N\rangle$ with a probability $p > 0.98$. However, this measurement naturally has a detection error and we can infer the actual $p(|0_N\rangle)$ from the subsequent tomography of the coherent state. The amplitude of the Q function at the angle $\theta = 0$ gives directly $p(|0_N\rangle) = 0.94$ (cf. figure 4.9).

- Scattering of an atom in $|1\rangle$ during the state preparation:
  After the MW pulse $R(\theta_{\text{prep}})$, we probe the cavity during 20 µs to decide whether an atom was prepared in $|1\rangle$ or not. In order to obtain a symmetric state, this measurement must be of quantum non-destructive nature. However, there is a small probability that the atom in $|1\rangle$ scatters a photon, whereby its external state is revealed to the environment. The ensemble carrying a shared excitation $|1_N\rangle$ therefore is transformed into a classical state $|10\ldots\rangle$ with one distinct excitation. The probability for such a scattering event p_{sc} has been calculated in section 1.3 and we find $p_{\text{sc}} = 0.2$ at the pump rate used in the experiment. Note that this probability is only dependent on the number of atoms in $|1\rangle$ and thus independent of the total atom number of the prepared state.

- Scattering of an atom in $|0\rangle$ during the state preparation:
  Analog to the case above, it is also possible for an atom in $|0\rangle$ to off-resonantly scatter a photon and to fall back into the $F = 2$ manifold. This means that not the MW (which collectively act on all atoms) but the detection light itself creates the excitation in the system. As above, this produces the classical state $|10\ldots\rangle$ with one distinct excitation. The probability for such an event can be deduced from the lifetime measurement of the state $|0_N\rangle$. For 41 atoms, we obtain a lifetime $\tau_{|0_N\rangle} = 560\,\mu\text{s}$, which gives a scattering probability $p_{\text{sc}} = 0.04$ for a 20 µs detection

pulse. The lifetime $\tau_{|0_N\rangle}$ scales inversely proportional to the atom number and we see that we can still increase the atom number by a factor of 2 until this effect becomes comparable to the other error sources.

- Preparation of higher order Dicke states:
  The MW pulse has a probability $p_{\text{prep}}(|1_N\rangle) = 0.27$ to excite exactly one atom. Naturally, there is a finite probability $p_{\text{prep}}(|n_N\rangle)$ to excite $n \geq 2$ atoms, which leads to (undesired) contributions of higher order Dicke states. This probability in our case is

$$\begin{aligned} p_{\text{prep}}(|n_N\rangle) &= 1 - p(|0_N\rangle) - p(|1_N\rangle) \\ &= 1 - \cos(\theta_{\text{prep}}/2)^{2N} - N\cos(\theta_{\text{prep}}/2)^{2N-2}\sin(\theta_{\text{prep}}/2)^2 = 0.06 \end{aligned} \tag{5.24}$$

  We only stop the preparation sequence if we measure low transmission, which eliminates the contribution of the coherent state $|0_N\rangle$. The contribution of higher order Dicke states to the prepared state therefore is:

$$\frac{p_{\text{prep}}(|n_N\rangle)}{p_{\text{prep}}(|1_N\rangle)} = 0.23. \tag{5.25}$$

  This means that a W state cannot be prepared with a fidelity higher than $1 - 0.23 = 0.77$. Of course, this error can be made arbitrarily small by choosing a smaller θ_{prep} and repeating the preparation sequence if the measurement result shows high transmission. However, this increases the number of repetitions of the preparation sequence, leading to an increase in the other limiting effects (see above). Our choice of $\theta_{\text{prep}} = 0.27$ is a tradeoff to minimize the total preparation error.
  The high portion in (5.25) of higher order Dicke states rises the question why we do not obtain such a high population in the result of our state reconstruction. Let us consider for example the state $|2_N\rangle$. Its contribution to the prepared state is expected to be

$$\frac{p_{\text{prep}}(|2_N\rangle)}{p_{\text{prep}}(|1_N\rangle)} = 0.20. \tag{5.26}$$

  However, the state $|2_N\rangle$ is subject to the same fidelity degrading effects as the state $|1_N\rangle$. Particularly the effects that are proportional to the atom number in $|1\rangle$, such as decoherence and the scattering of an atom in $|1\rangle$ (see above) lead to a quadratic decrease of the population in the state $|2_N\rangle$. We therefore expect a contribution of $|2_N\rangle$ to the final state of

$$\frac{p_{\text{prep}}(|2_N\rangle)}{p_{\text{prep}}(|1_N\rangle)} \cdot c_{\text{init}} \cdot c_{\text{sc},|1\rangle}^2 \cdot c_{\text{sc},|0\rangle} \cdot c_{\text{dec}}^2 \overset{\text{N=41}}{=} 0.2 \cdot 0.96 \cdot 0.85^2 \cdot 0.94 \cdot 0.7^2 = 0.06 \tag{5.27}$$

  where the c denote the fidelity degrading factors from the effects mentioned above and the decoherence. The expected value lies within 1σ of the obtained one (see table 5.2). The remaining discrepancy between the expected and the obtained population ρ_{22} is subject to further investigation and might be attributed to an additional loss channel such as light-induced collisions with two atoms in $|1\rangle$.

- Detection error during the preparation sequence:
  In the state preparation sequence, we perform a QND measurement and deduce its outcome on the basis of the counts in transmission T and reflection R. A major source of error is the wrongly assumption that the MW pulse has transferred an atom to $|1\rangle$ while in fact all atoms are still in $|0\rangle$. It is quantitatively given by $\epsilon_{10}^{\text{prep}}$ (see (4.9)) and increases the prepared state's population in $|0_N\rangle$. However, we can drastically reduce $\epsilon_{10}^{\text{prep}}$ in postselection by choosing only experimental runs with $R \geq R_{\text{prep}}$. We hereby remove runs where the result of the preparation sequence is ambiguous but we also reduce the number of measurements, which increases the statistical error of the state reconstruction. Figure 5.6a) shows the fidelity of the state with $N = 41$ when the threshold R_{prep} is varied from $R_{\text{prep}} = 4$ (the default value of the sequence) to $R_{\text{prep}} = 11$, which is the value used to obtain the datasets presented in section 5.1. Figure 5.6b) shows the number of measurements corresponding to each threshold. When choosing an R_{prep} which maximizes the fidelity, we limit ourselves to datasets with at least 1500 runs to keep the reconstruction error below 10%. For $R_{\text{prep}} = 11$, the fraction of successful runs is 9%.

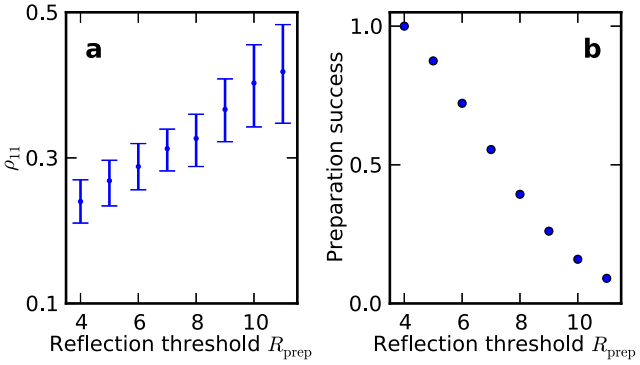

Figure 5.6.: Influence of the threshold R_{prep} on the fidelity and the number of measurements. a) Population in ρ_{11} for increasing threshold. The fidelity rises, as well as the statistical error of the reconstruction method. b) Number of successful runs for an increasing threshold.

- Decoherence:
  The reason for decoherence in our system as well as the effect on the fidelity were presented in section 4.4. We obtained that the fidelity is reduced to 0.78 for a state containing 41 atoms.

Table 5.4 summarizes all limitations listed above and gives an estimate of the expected fidelity. We see that it agrees well with the obtained result.

Except for the decoherence, all the limitations can be reduced by the use of a cavity of higher finesse. The consequences would be two-fold: On the one hand, the hyperfine state detection error would be reduced, improving the initial coherent state preparation and the tomography. On the other hand, less photons would be needed to infer the atomic state, putting the experimental system further in the regime of a QND measurement. This would allow to reduce the angle θ_{prep} and the portion of higher order Dicke states to the prepared states. Simulations show that a cavity with a finesse of 120000

Effect	Decrease in fidelity
Initial state preparation	0.94
Scattering of an atom in $\|1\rangle$	0.8
Scattering of an atom in $\|0\rangle$	0.96
Preparation of higher order Dicke states	0.77
$\epsilon_{10}^{\text{prep}}(R_{\text{prep}} = 11)$	≈ 1
Decoherence	0.78
Expected fidelity	0.43
Obtained fidelity	0.42

Table 5.4.: Fidelity limiting factors and expected fidelity for a state with N=41.

(as already available [79]) could produce states with a fidelity exceeding 0.9.

5.3. Verification of multiparticle entanglement

Our target state $|1_N\rangle$ constitutes a famous example of an entangled state. In this section, we briefly introduce its properties and devise a criterion to quantify the degree of multiparticle entanglement that is present in our experimentally created state.

5.3.1. Introduction

The concept of entanglement is a purely quantum mechanical feature. In general, it is not possible to describe a quantum system composed of N particles by describing the state of each of the individual particles alone [113, 22]. The famous quote of the Greek philosopher Aristotle "The whole is greater than the sum of its parts" [114] becomes literally true in the world of quantum physics.

In the following, we consider only pure states for simplification. In the spirit of the quote above, we define for a system composed of N particles [115]:

> Any N-partite pure state $|\varphi_{A,\ldots,N}\rangle \in \mathcal{H}_{A,\ldots,N} = \mathcal{H}_A \otimes \ldots \otimes \mathcal{H}_N$ is called fully separable (entangled), if it can (cannot) be written in the form
>
> $$|\varphi_{A,\ldots,N}\rangle = |\varphi_A\rangle \otimes \ldots \otimes |\varphi_N\rangle \qquad |\varphi_A\rangle \in \mathcal{H}_A, \ldots, |\varphi_N\rangle \in \mathcal{H}_N \tag{5.28}$$

This straight-forward definition conceals the fact that the concept of entanglement is very rich and complex. Let us consider e.g. the three-particle case in the Hilbert-space $\mathcal{H}_{A,B,C} = \mathcal{H}_A \otimes \mathcal{H}_B \otimes \mathcal{H}_C$. According to the definition (5.28), both the following states

are entangled:

$$|\mathrm{GHZ}\rangle = \frac{1}{\sqrt{2}}\left[|000\rangle + |111\rangle\right] \tag{5.29}$$

$$|\varphi_{\mathrm{par}}\rangle = \frac{1}{\sqrt{2}}\left[|10\rangle + |01\rangle\right] \otimes |0\rangle \tag{5.30}$$

We intuitively see that the state $|\varphi_{\mathrm{par}}\rangle$ must be "less" entangled than the state $|\mathrm{GHZ}\rangle$ [116], since unlike $|\mathrm{GHZ}\rangle$, it can be seen as a product state of an entangled state "living" in $\mathcal{H}_{A,B}$ and a pure state in $\mathcal{H}_C$.

This leads to the definition of "partial entanglement" [115]:

> Any N-particle pure state $|\varphi_{A,\ldots,N}\rangle \in \mathcal{H}_{A,\ldots,N} = \mathcal{H}_A \otimes \ldots \otimes \mathcal{H}_N$ is called n-particle entangled ($(n-1)$-separable) if it cannot (can) be written in the form
>
> $$|\varphi_{A,\ldots,N}\rangle = |\varphi_1\rangle \otimes \cdots \otimes |\varphi_k\rangle \tag{5.31}$$
>
> where the indices $1,\ldots,k$ denote the partitions $\{I_1,\ldots,I_k\}$ that each contain less than n particles.

A fully (N-particle) entangled state is therefore a state that cannot even be written as the product of two states $|\varphi_{A,\ldots,N}\rangle = |\varphi_{\mathcal{A}}\rangle \otimes |\varphi_{\mathcal{B}}\rangle$, where $\mathcal{A}$ and $\mathcal{B}$ denote disjoint subsets of $\{A,\ldots,N\}$. If we describe the state $|\varphi_{A,\ldots,N}\rangle$ via a density matrix ρ, this statement is equivalent to saying that all bipartite partitions of ρ produce mixed reduced density matrices. For $N = 3$, a famous example of such a fully entangled state is the state $|\mathrm{GHZ}\rangle$ from (5.29).

Another example is the W state $|1_{N=3}\rangle$ [87]:

$$|1_{N=3}\rangle = \frac{1}{\sqrt{3}}\left[|100\rangle + |010\rangle + |001\rangle\right] \tag{5.32}$$

The definitions above indicate that the states $|\mathrm{GHZ}\rangle$ and $|1_{N=3}\rangle$ both are fully entangled. Yet their properties are very different: Tracing out one particle leads to a fully separable two-particle state for $|\mathrm{GHZ}\rangle$, but preserves the maximal possible entanglement for $|1_{N=3}\rangle$ [87, 115].

The interesting properties of the 3-particle case persist for the W state $|1_N\rangle$ containing N particles: The state is fully entangled and the entanglement is robust under particle loss.

5.3.2. A convenient entanglement criterion in the vicinity of the W state

We want to quantify the presence of multiparticle entanglement in our experimentally created state. We have obtained the density matrix from the state reconstruction, which in principle contains all the information about the state. However, it is not trivial to extract the degree of entanglement from the populations of the density matrix. For example, fully separable states (FSSs) can also have a non-zero population in entangled states. This can be illustrated by describing a coherent (and therefore fully separable)

state $|\theta,\phi\rangle$ in the basis of Dicke states (see (4.8)). Depending on θ, $|\theta,\phi\rangle$ can have a non-zero population in the first Dicke state:

$$\mathcal{F} = |\langle 1_N|\theta,\phi\rangle|^2 = N\cos(\theta/2)^{2N-2}\sin(\theta/2)^2 \tag{5.33}$$

which corresponds to the probability to excite exactly one atom in a rotation R_θ. In the case $N \to \infty$, the maximal population is 0.37. This shows that we need a more subtle way to quantify entanglement than just the fidelity $\mathcal{F}$.

We have therefore devised a criterion to detect entanglement as well as n-particle entanglement from a states' population in the states $|0_N\rangle$ and $|1_N\rangle$.

In the following, we present the proof of this criterion. We first distinguish a FSS from an entangled state, before we extend the criterion to states with at least n entangled atoms.

Criterion for entanglement

The principle of the criterion is as follows: For a FSS, we find an upper bound for the population ρ_{11} in the state $|1_N\rangle$, as a function of the population ρ_{00} in the state $|0_N\rangle$. This means, we demonstrate that for a FSS, the population in $|1_N\rangle$ can only attain a certain value $\rho_{11,\max}$. If a state has a higher population than $\rho_{11,\max}$, it must be entangled.

A pure FSS of N two-level systems can be written as:

$$|\varphi_{A,\ldots,N}\rangle = |\varphi_1\rangle \otimes \ldots \otimes |\varphi_N\rangle \tag{5.34}$$

with $|\varphi_i\rangle = \alpha_i|0\rangle + \beta_i|1\rangle$, $|\alpha_i|^2 + |\beta_i|^2 = 1$. The populations ρ_{00} (ρ_{11}) in the $|0_N\rangle$ ($|1_N\rangle$) state are:

$$\rho_{00} = |\langle 0_N|\varphi_{A,\ldots,N}\rangle|^2 = \prod_{i=1}^{N}|\alpha_i|^2 \tag{5.35}$$

$$\begin{aligned}\rho_{11} &= |\langle 1_N|\varphi_{A,\ldots,N}\rangle|^2 \\ &= \left|\frac{1}{\sqrt{N}}\sum_{i=1}^{N}\left(\langle 0|\varphi_1\rangle\ldots\langle 1|\varphi_i\rangle\ldots\langle 0|\varphi_N\rangle\right)\right|^2 \\ &= \frac{1}{N}\left|\sum_{i=1}^{N}\left(\beta_i\prod_{j=0,j\neq i}^{N}\alpha_j\right)\right|^2\end{aligned} \tag{5.36}$$

We want to maximize ρ_{11}. The value of ρ_{11} only depends on the absolute value of α_i, β_i. We can therefore assume α_i, $\beta_i \in [0,1]$.

We first consider the case $\rho_{00} = 0$:

In this case, at least one α_i is zero. We set $\alpha_1 = 0$. ρ_{11} therefore is:

$$\rho_{11} = \frac{1}{N}\left|\prod_{j=2}^{N}\alpha_j\right|^2 \tag{5.37}$$

Expression (5.37) is maximal for all $\alpha_j = 1$ and therefore:

$$\operatorname*{Max}_{\rho_{00}=0}[\rho_{11}] = \frac{1}{N} \tag{5.38}$$

We now consider the case $\rho_{00} \neq 0$:
In this case, all α_i are non-zero and (5.36) becomes:

$$\rho_{11} = \frac{1}{N}\left\{\left(\prod_{j=1}^{N}\alpha_j\right)\left(\sum_{i=1}^{N}\frac{\beta_i}{\alpha_i}\right)\right\}^2 = \frac{\rho_{00}}{N}\left\{\sum_{i=1}^{N}\frac{\sqrt{1-\alpha_i^2}}{\alpha_i}\right\}^2 \tag{5.39}$$

Expression (5.39) results in a maximization problem of the function $F_N(\alpha_1, ..., \alpha_N) = \sum_{i=1}^{N}\frac{\sqrt{1-\alpha_i^2}}{\alpha_i}$ under the constraint $\prod_{i=1}^{N}\alpha_i^2 = \rho_{00}$. Such a problem can be solved using Lagrange multipliers. The calculation can be found in appendix B. Here, we only state the result in a graphical representation (see figure 5.7). For large atom numbers, $\mathrm{Max}[\rho_{11}]$ is reached for $\alpha_1 = ... = \alpha_N = \rho_{00}^{1/(2N)}$. This physically corresponds to a coherent spin state.

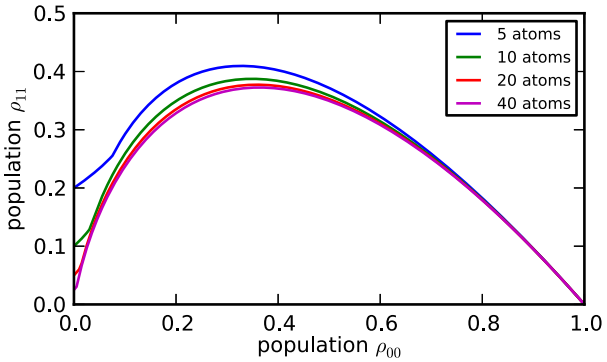

Figure 5.7.: The entanglement criterion for pure states and different atom numbers.

However, the above result applies only to pure states. The statement can be extended to mixed states by making the function $\mathrm{Max}[\rho_{11}]$ concave. This is done by linearly interpolating between the values $\rho_{11}(\rho_{00} = 0) = \frac{1}{N}$ and $\rho_{11}\left(\rho_{00} > N^{\frac{N}{1-N}}\right) = N\rho_{00}(\rho_{00}^{-\frac{1}{N}} - 1)$. We obtain the function $\mathcal{C}(\rho_{00})$:

$$\mathcal{C}(\rho_{00}) = \begin{cases} N\rho_{00}(\rho_{00}^{-\frac{1}{N}} - 1), & \text{if } \rho_{00} \geq N^{\frac{N}{1-N}}. \\ \frac{1}{N} + \rho_{00}\left[\frac{N\rho_{00}(\rho_{00}^{-\frac{1}{N}}-1)-\frac{1}{N}}{N^{\frac{N}{1-N}}}\right], & \text{if } \rho_{00} < N^{\frac{N}{1-N}}. \end{cases} \tag{5.40}$$

A state $|\varphi_{A,...,N}\rangle$ with $\rho_{11,\varphi} = |\langle 1_N|\varphi_{A,...,N}\rangle|^2$ and $\rho_{00,\varphi} = |\langle 0_N|\varphi_{A,...,N}\rangle|^2$ is therefore entangled if:

$$\rho_{11,\varphi} > \mathcal{C}(\rho_{00,\varphi}) \tag{5.41}$$

The function $\mathcal{C}(\rho_{00,\varphi})$ is graphically depicted in figure 5.8.

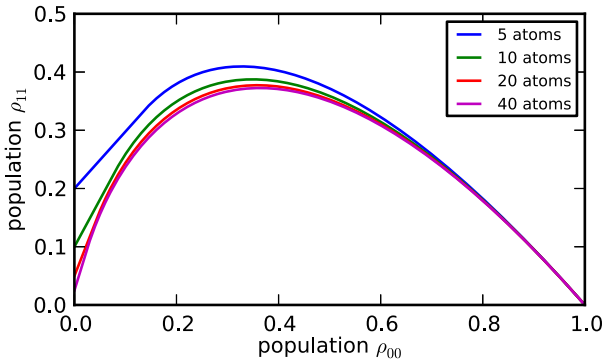

Figure 5.8.: The entanglement criterion from figure 5.7 extended to mixed states. The populations ρ_{00} and ρ_{11} of a separable state with a certain atom number - mixed or pure - can only lie in the area below the corresponding threshold. If a state has populations above the threshold, it must be entangled.

Criterion for n entangled atoms

In analogy to the case above, we now derive a criterion to distinguish an $(n-1)$-separable state form a state containing at least n entangled atoms. We first consider only pure states $|\varphi_{A,\ldots,N}\rangle$ with:

$$|\varphi_{A,\ldots,N}\rangle = |\varphi_1^{1,\ldots,n}\rangle \otimes |\varphi_2^{n+1,\ldots,2n}\rangle \otimes \ldots \otimes |\varphi_k^{(k-1)n+1,\ldots,N}\rangle \tag{5.42}$$

In (5.42), each of the k blocks $|\varphi_i\rangle$ corresponds to at most n entangled atoms ($n' = N-n(k-1)$ entangled atoms for $|\varphi_k\rangle$) and can be expanded in the basis of Dicke states $|J,m\rangle$:

$$\begin{aligned} |\varphi_i^n\rangle &\equiv |\varphi_i^{(i-1)n,\ldots,in}\rangle \\ &= a_i \left|J=\frac{n}{2},-\frac{n}{2}\right\rangle + b_i \left|J=\frac{n}{2},-\frac{n}{2}+1\right\rangle + \ldots \\ &= a_i|0_n\rangle + b_i|1_n\rangle + \ldots \end{aligned} \tag{5.43}$$

Then, we can write in analogy to the pure FSS state (see expressions (5.35) and (5.36)):

$$\widetilde{\rho}_{00} = |\langle 0_N|\varphi_{A,\ldots,N}\rangle|^2 = \prod_{i=1}^{N} |a_i|^2 \tag{5.44}$$

$$\begin{aligned} \widetilde{\rho}_{11} &= |\langle 1_N|\varphi_{A,\ldots,N}\rangle|^2 \\ &= \frac{1}{N}\left|\sum_{i=1}^{N}\langle 0,\ldots,i:1,\ldots,0|\varphi_1^n\otimes\varphi_2^n\otimes\ldots\otimes\varphi_k^{n'}\rangle\right|^2 \\ &= \frac{1}{N}\left|\sum_{i=1}^{k}\left(\sum_{j=(i-1)n+1}^{in\ (\text{or } N)}\langle 0,\ldots,j:1,\ldots,0|\varphi_1^n\otimes\ldots\otimes\varphi_k^{n'}\rangle\right)\right|^2 \\ &= \frac{1}{N}\left|\sum_{i=1}^{k}\left(\sqrt{n_i}b_i\prod_{j=1,j\neq i}^{k}a_i\right)\right|^2 \end{aligned} \tag{5.45}$$

where $n_{1,\ldots,k-1} = n$ and $n_k = n'$.
For a given set of b_i, $\widetilde{\rho}_{11}$ is maximal when the $|a_i|$ are maximal[2]. We can therefore assume as above $|a_i|^2 + |b_i|^2 = 1$ and $a_i, b_i \in [0,1]$.
In the case $\widetilde{\rho}_{00} = 0$, expression (5.45) becomes:

$$\underset{\widetilde{P}_0=0}{\mathrm{Max}}[\widetilde{\rho}_{11}] = \frac{1}{N}\left|\sqrt{n}\prod_{j=2}^{N} a_j\right|^2 = \frac{n}{N} \tag{5.46}$$

In the case $\widetilde{\rho}_{00} \neq 0$, we can rewrite expression (5.45) as

$$\widetilde{\rho}_{11} = \frac{\widetilde{\rho}_{00}}{N}\left\{\sqrt{n}F_{k-1}(a_1,\ldots,a_{k-1}) + \sqrt{n'}F_1(a_k)\right\}^2 \tag{5.47}$$

Maximizing (5.47) is a problem similar to maximizing expression (5.39).
To also account for mixed states, the function $\mathrm{Max}[\widetilde{\rho}_{11}]$ (in analogy to $\mathrm{Max}[\rho_{11}]$) has to be made concave. We note that for a block size of $n = 1$, we recover the bipartite entanglement criterion of expression (5.40). Figure 5.9 shows $\mathrm{Max}[\widetilde{\rho}_{11}]$ (including mixed states) for different numbers of entangled particles.

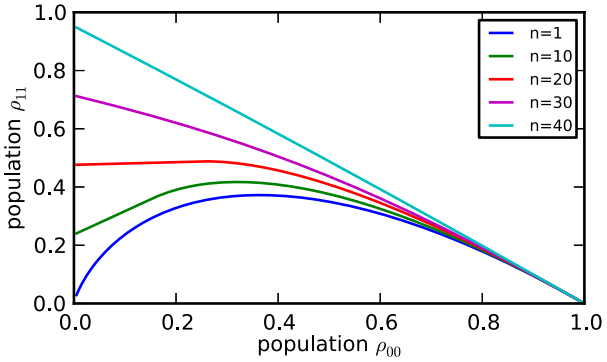

Figure 5.9.: The thresholds indicating n-particle entanglement in a state with a total atom number N=41. The number of entangled particles n is indicated in the legend.

5.3.3. Entanglement in the experimentally created state

We use the entanglement criterion to infer the degree of multiparticle entanglement present in our state. We obtain ρ_{00} and ρ_{11} from the state reconstruction and compare it to the bound $C(\rho_{00})$ for FSS (see (5.40)) and its analogon for $(n-1)$-separable states.

2. This has been verified numerically.

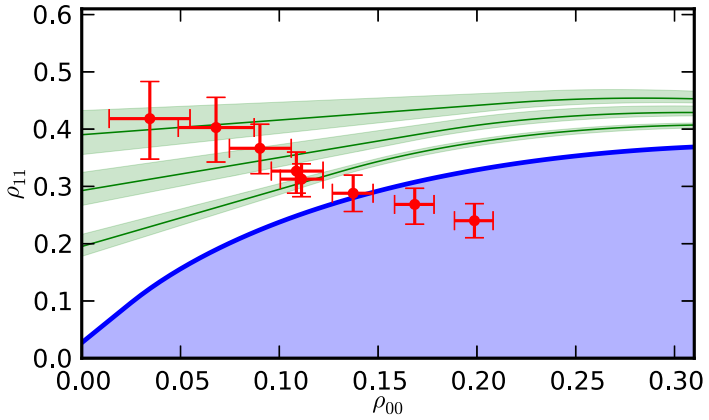

Figure 5.10.: Multiparticle entanglement for the created W state with $N = 41$. Fully separable states lie within the blue shaded area. From bottom to top, the green curves show the bound for a $(n-1)$-separable state with $n = 9, 13, 17$. The green shaded areas limit the bounds when varying the atom number from 37 to 45, which corresponds to 1σ of the atom number distribution. The red points are the same data shown in figure 5.6.

Figure 5.10 shows the populations ρ_{00} and ρ_{11} for the state with $N = 41$ for different values of R_{prep} (these are the same datasets as in figure 5.6). In the same plot, we depict the bound $C(\rho_{00})$ (thick blue line). Any state outside the blue shaded area contains at least 2-particle entanglement. The green lines from bottom to top show the bound for $(n-1)$-separable states with $n = 9, 13, 17$. Any state above the bound contains at least n entangled particles. We see that for increasing R_{prep}, the number of entangled particles in the state increases. For $R_{\mathrm{prep}} = 11$, we are more than 1σ above the bound for a 12-separable state, showing that the state contains at least 13 entangled particles.

5.4. Conclusion

In this chapter, we have analyzed the data obtained in the W state generation experiment. We have reconstructed the density matrix in the symmetric subspace using three different reconstruction techniques and have given error estimates on the populations in the different Dicke states. The best result yields a fidelity of 0.42 for a state containing 41 atoms.

Furthermore, we have investigated the other fidelity-limiting factors of our state generation method and have compared them to the fidelity obtained in the experiment.

Finally, we have studied the entanglement properties of the created state. We have devised a criterion to quantify multiparticle entanglement and have found that the experimentally created state with the highest fidelity contains at least 13 entangled particles.

6. Creation of entangled states via quantum Zeno dynamics

Zeno of Elea was a Greek philosopher who puzzled his contemporaries with a number of paradoxa which mainly dealt with the concepts of infinity and infinite divisibility.

One of his most famous paradoxa was phrased by Aristotle in his "Physics" [117] as follows:

> "If everything when it occupies an equal space is at rest, and if that which is in locomotion is always occupying such a space at any moment, the flying arrow is therefore motionless."

To solve, or better circumvent this paradox, mathematicians in the 19th century developed the concept of continuous functions, which made it possible to deal with infinite processes. The paradox seemed solved, but Zeno experienced a revival in the field of physics in the 1970s, when Misra and Sudarshan introduced the idea that constantly observing a quantum system would slow or even freeze its evolution if the measurement projects onto one eigenstate of the measured observable [118]. Of course, this is not a paradox, but a mathematical consequence of the solution of the Schrödinger equation at short times [119]. The phenomenon was therefore named "Quantum Zeno Effect" (QZE). It has already been experimentally realized in different physical systems [120, 121, 122, 123, 124].

A different situation is obtained if the quantum Zeno measurement yields the same outcome for multiple eigenstates. In this case, it only projects the system onto a subspace of the total Hilbert space. The evolution of the system is not frozen, but restricted to the projected subspace. This phenomenon is known as "Quantum Zeno Dynamics" (QZD) [125, 126, 127]. It has not yet been experimentally demonstrated until very recently [128]. We introduce its principle in section 6.1 and demonstrate how it can be used to create entangled multiparticle states.

In section 6.2, we propose a scheme to create a W state in our experimental system with the help of the QZD. We focus on some experimental challenges, estimate an upper bound for the expected fidelity and give preliminary results.

6.1. The Quantum Zeno Dynamics

We shortly introduce the principle of the QZD. Our reasoning follows [129]. We consider a system with density matrix ρ_0 in the m-dimensional Hilbert space $\mathcal{H}$, subject to a Hamiltonian H. It is probed by a measurement P, for which several states yield the same measurement outcome. P then only projects the system into a subspace. We assume that P probes if the system is in the s-dimensional subspace $P\mathcal{H} = \mathcal{H}_p$, with $s < m$.

Let the system initially be in the subspace $\mathcal{H}_p$:

$$\rho_0 = P\rho_0 P \tag{6.1}$$

After a short time τ, the state evolves into

$$\rho(\tau) = U(\tau)\rho_0 U^\dagger(\tau) \tag{6.2}$$

with $U(\tau) = \mathrm{e}^{-iH\tau} = 1 - iH\tau + \mathcal{O}(\tau^2)$.

If we measure P after time τ, the result is positive with a probability

$$\begin{aligned} p(\tau) &= \mathrm{Tr}\left[U(\tau)\rho_0 U^\dagger(\tau)P\right] && (6.3)\\ &= \mathrm{Tr}\left[PU(\tau)P\rho_0 PU^\dagger(\tau)P\right] && (6.4)\\ &= \mathrm{Tr}\left[V(\tau)\rho_0 V^\dagger(\tau)\right] && (6.5) \end{aligned}$$

with $V(\tau) = PU(\tau)P$.

The state then becomes

$$\rho_0 \to P\rho(\tau)P = PU(\tau)\rho_0 U^\dagger(\tau)P = PU(\tau)P\rho_0 PU^\dagger(\tau)P = V(\tau)\rho_0 V^\dagger(\tau) \tag{6.6}$$

In analogy to the QZE, we now consider N measurements during the time t and study the case $N \to \infty$:

$$\begin{aligned} \rho^{(N)}(t) &= \left[PU(t/N)P\right]^N \rho_0 \left[PU^\dagger(t/N)P\right]^N && (6.7)\\ &\equiv V_N(t)\rho_0 V_N^\dagger(t) \qquad V_N = \left[PU(t/N)P\right]^N && (6.8) \end{aligned}$$

For $N \to \infty$, $V_N(t)$ becomes

$$\begin{aligned} \lim_{N\to\infty} V_N(t) &= \lim_{N\to\infty}\left[P\mathrm{e}^{-iHt/N}P\right]^N \\ &= \lim_{N\to\infty}\left[P(1 - iHt/N)P\right]^N \\ &= \lim_{N\to\infty} P(1 - iPHPt/N) \\ &= P\mathrm{e}^{-iPHPt} \quad \equiv U_z(t) \end{aligned} \tag{6.9}$$

The probability to find the system in $\mathcal{H}_p$ after time t is

$$\lim_{N\to\infty} p^N(t) = \mathrm{Tr}\left[U_z(t)\rho_0 U_z(t)\right] = 1 \tag{6.10}$$

(6.9) shows that the evolution of the system is unitary in the subspace $\mathcal{H}_p$, defined by the projection of H on P:

$$H_z = PHP \tag{6.11}$$

6.2. Proposition for the generation of W states via Quantum Zeno Dynamics

The situation described in section 6.1 can be realized with our cavity setup. We consider the same experimental configuration as in chapter 4, i.e. N atoms equally coupled to the cavity, with the cavity and the probe light resonant to the $F = 2 \rightarrow F' = 3$ transition. The Quantum Zeno Dynamics (QZD) is induced by the fact that by probing the cavity, we can distinguish if all the atoms are in $|0\rangle$ or if at least one atom is in the state $|1\rangle$ in the QND regime. The operator P corresponding to this measurement therefore projects the collective state of the atomic ensemble onto the subspace $\mathcal{H}_P$ spanned by the Dicke states $\{|n_N\rangle\}$, $n \geq 1$ if the measurement outcome is 1, and onto the state $|0_N\rangle$ if the outcome is 0.

A microwave field drives Rabi-oscillations between $|0\rangle$ and $|1\rangle$ with a frequency Ω. The corresponding Hamilton operator is $H_R = \Omega J_x$ and reads in the basis of Dicke states:

$$H_R = \frac{1}{2}\Omega \begin{pmatrix} 0 & \sqrt{-n^2+Nn+n} & 0 & \cdots \\ \sqrt{-n^2+n(N-1)+N} & 0 & \ddots & \\ 0 & \ddots & \ddots & \\ \vdots & & & \end{pmatrix} \tag{6.12}$$

Under the influence of continuous observation, realized by the operator P, the system evolves under the modified Hamiltonian H_Z:

$$H_Z = PH_RP = \frac{1}{2}\Omega \begin{pmatrix} 0 & 0 & \cdots & & \\ 0 & 0 & \sqrt{-n^2+Nn+n} & 0 & \cdots \\ \vdots & \sqrt{-n^2+n(N-1)+N} & 0 & \ddots & \\ & 0 & \ddots & \ddots & \\ & \vdots & & & \end{pmatrix} \tag{6.13}$$

with

$$P = \begin{pmatrix} 0 & 0 & \cdots \\ 0 & 1 & \\ \vdots & & \ddots \end{pmatrix} \tag{6.14}$$

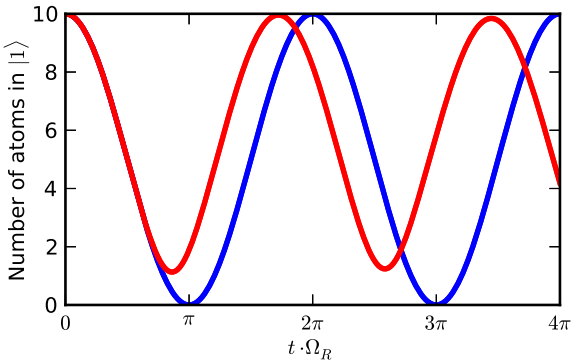

Figure 6.1.: Rabi oscillations for a state with 10 atoms. The blue curve shows the unperturbed oscillation, and the red curve shows the oscillation restricted to the subspace $\mathcal{H}_P$. The Rabi frequency is increased, and there is always at least one atom in $|1\rangle$.

Figure 6.1 compares the evolution under the Hamiltonian H_R and H_Z. We see that the QZD blocks the evolution into the state $|0_N\rangle$, which results in a coherent oscillation with an increased Rabi frequency Ω_Z.

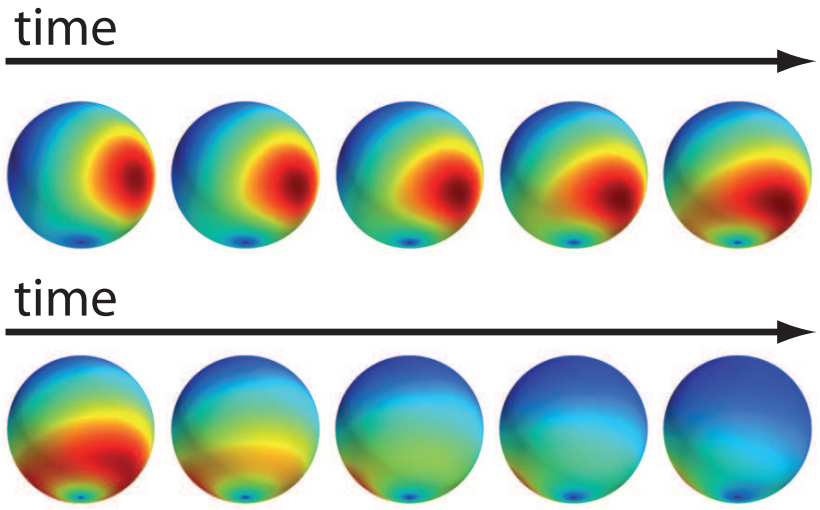

Figure 6.2.: The evolution of the state from figure 6.1 (red curve) on the Bloch sphere. The south pole is never populated, because the constant measurement prevents the occupation of the state $|0_N\rangle$. When the (initially coherent) state approaches the south pole, it splits and encircles it. At $t = \pi/\Omega_Z$ (first image, second row), the overlap with the W state is maximal.

Figure 6.2 shows the evolution of the state on the multiparticle Bloch sphere. After the time $t_\pi = \pi/\Omega_Z$, the system has a high overlap with the Dicke state containing one excitation $|1_N\rangle$.

This means that by letting the state evolve in a QZD environment for a fixed time t_π, the system will evolve into an entangled state. The difference with respect to the experiments of chapter 4 is that this scheme is deterministic, in the sense that the

entangled state is created regardless of the outcome of any (macroscopic) measurement.

6.2.1. Experimental parameters

We would like to know in which parameter range we should perform the experiment to obtain a maximal fidelity. The pumped cavity is an open quantum system, which renders it difficult to answer this question analytically. We therefore use a simulation which consists in solving the master equation of a Hamiltonian introduced in the following:

We consider N three-level atoms (with levels $|0\rangle$, $|1\rangle$ and $|\mathrm{e}\rangle$), coupled to a single mode of a cavity with linewidth $\kappa = 2\pi \cdot 53\,\mathrm{MHz}$, which is pumped at a rate η. The cavity and the pump light are both resonant to the $|1\rangle \to |\mathrm{e}\rangle$ transition. The atoms in $|1\rangle$ ($|0\rangle$) couple to the light mode with $g_1 = {}^1/\sqrt{2}\, g_{\max} = 2\pi \cdot 170\,\mathrm{MHz}$ ($g_0 = \sqrt{{}^2/3}\, g_{\max} = 2\pi \cdot 196\,\mathrm{MHz}$). Furthermore, the levels $|0\rangle$ and $|1\rangle$ have a frequency difference of $\Delta_{\mathrm{HF}} = 2\pi \cdot 6.8\,\mathrm{GHz}$ and are coupled by a resonant MW with Rabi frequency Ω. Since we are in the weak probing limit (${}^{\eta^2}/_{g^2} \ll 1$), we can limit the photonic part of the Hilbert space to 0, 1 and 2 photons. Furthermore, we limit the atomic subspace to fully symmetric states and we only consider either zero or one atom in the excited state $|\mathrm{e}\rangle$. This means that for N atoms, the atomic subspace is comprised of the states

$$\{|N-n,n,0\rangle\,,\ |N-n-1,n,1\rangle\,,\ |0,N,0\rangle\} \qquad n = 0,\ldots,N-1 \tag{6.15}$$

where $|n_0, n_1, n_\mathrm{e}\rangle$ denotes a symmetric state with n_0 atoms in $|0\rangle$, n_1 atoms in $|1\rangle$ and n_e atoms in $|\mathrm{e}\rangle$.

The Hamiltonian H,

$$H = H_{\mathrm{JC}} + H_R + H_{\mathrm{LS}} + H_P \tag{6.16}$$

is comprised of a Jaynes-Cummings part (where we only allow for atoms in $|1\rangle$ to optically couple to $|\mathrm{e}\rangle$)

$$\begin{aligned} H_{\mathrm{JC}} &= -ig(a\sigma^+ + a^\dagger\sigma^-) \\ \sigma^+ &= |N-n-1,n+1,0\rangle\langle N-n-1,n,1| \\ \sigma^- &= |N-n-1,n,1\rangle\langle N-n-1,n+1,0|\ , \end{aligned} \tag{6.17}$$

a Rabi part coupling the states $|0\rangle$ and $|1\rangle$

$$H_R = \Omega J_x, \tag{6.18}$$

a part taking into account the light shift

$$H_{\mathrm{LS}} = -\frac{g^2}{\Delta_{\mathrm{HF}}} N_0, \tag{6.19}$$

and a pump term

$$H_P = -i\eta(a - a^\dagger). \tag{6.20}$$

We numerically solve the master equation

$$\begin{aligned} \frac{\partial\rho}{\partial t} &= \mathcal{L}\rho \\ \mathcal{L}\rho &= -\frac{i}{\hbar}[H,\rho] \ +\ \kappa(2a\rho a^\dagger - \{\rho, a^\dagger a\}), \end{aligned} \tag{6.21}$$

which takes into account the photon loss from the cavity. We do not include spontaneous emission events in the simulation, because they cause the state of the atomic ensemble to leave the symmetric subspace, which greatly enhances the dimensions of the density matrix. Instead, we compute the number N_{sc} of spontaneous emission events from the population p_{e} in the state $|\mathrm{e}\rangle$ as

$$N_{\mathrm{sc}} = 2\gamma p_{\mathrm{e}} \tag{6.22}$$

with the spontaneous emission rate $\gamma = 2\pi \cdot 3\,\mathrm{MHz}$. Due to computational limitations, we can solve the simulation for a maximal number of $N = 10$ atoms, which corresponds to a (63×63) density matrix.

We note that this is a simplified model, which does not take into account important properties of our experimental setup such as the multilevel structure of the atoms and the second mode of the cavity. We therefore do not use it to predict the exact temporal evolution of the system, but to find the optimal range of parameters and to give an upper bound on the attainable fidelity.

Figure 6.3 shows the temporal evolution of the atomic ensemble as the result of the simulation. We initiate the system in the state $|0, N, 0\rangle$ and drive a Rabi oscillation at the frequency Ω_R. While the blue curve for a pump rate $\eta = 0$ matches the prediction of the analytic model (blue line in figure 6.1), the red curve for a finite pump rate is substantially different (cf. red line in figure 6.1): The amplitude of the Zeno-enhanced Rabi oscillation decreases. This is due to the pump light field, which entangles the number of atoms in $|1\rangle$ with the cavity transmission, leading to a loss of coherence and a damping of the Rabi oscillation.

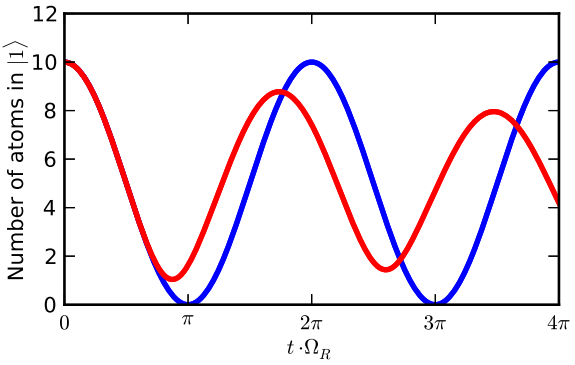

Figure 6.3.: Temporal evolution of a collective state of 10 atoms as the result of the simulation. For a pump rate $\eta = 0$, the system undergoes unperturbed Rabi oscillations. If the pump light is turned on ($\eta = \sqrt{30\kappa\Omega}$, red curve), the evolution is restricted to the subspace $\mathcal{H}_P$ with at least one atom in $|1\rangle$. The amplitude of the Zeno-enhanced Rabi oscillation decreases because of decoherence induced by the probe light.

We use the simulation to infer the optimal ratio $\mathcal{R} = \eta^2/\kappa\Omega$ between the incoming photon rate on the cavity η^2/κ and the Rabi frequency Ω. If $\mathcal{R}$ is too small, the system can evolute into the state $|0_N\rangle$, if $\mathcal{R}$ is too big, the number of scattering events is too high. We obtain the fidelity ρ_{11} and the scattering probability p_{sc} as a function of $\mathcal{R}$ from the simulation and choose the optimum ratio $\mathcal{R}_{\mathrm{opt}}$ as the one which maximizes

the product $\rho_{11} \cdot (1 - p_{sc})$. Figure 6.4 shows that the optimal ratio is $\mathcal{R}_{opt} = 12.1$ for our experimental setup and an atom number of 10. At this point, we can obtain the state $|1_N\rangle$ with a maximal fidelity of 0.71 .

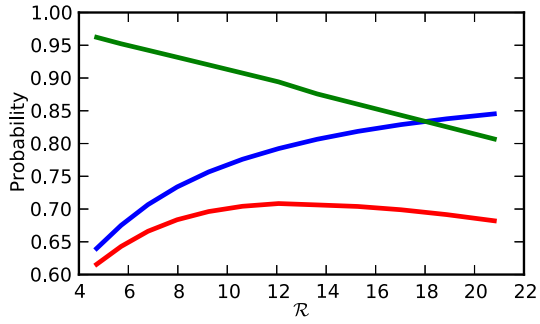

Figure 6.4.: The Fidelity ρ_{11} (blue curve) and the probability for no scattering events $(1 - p_{sc})$ during the W state preparation (green curve) in dependence of $\mathcal{R}$ for N=10 atoms. The red curve shows the product $\rho_{11} \cdot (1 - p_{sc})$. It is maximal for $\mathcal{R} = 12.1$.

Figure 6.5 shows how $\mathcal{R}_{opt}$ and the maximal fidelity scale with the atom number N. We are not able to provide results for $N > 10$, since the computational effort increases exponentially, but the results for $N \leq 10$ allow to extrapolate the accessible fidelity for higher atom numbers.

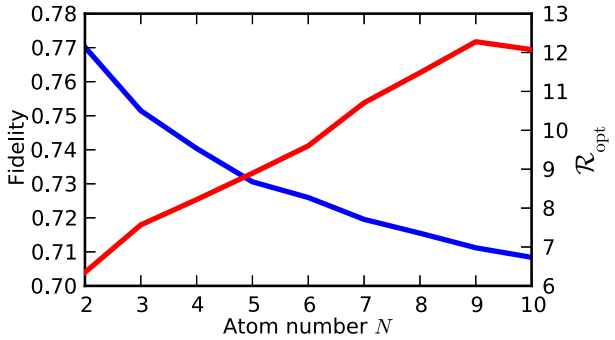

Figure 6.5.: The maximal fidelity (blue curve) and the corresponding optimal ratio $\mathcal{R}_{opt}$ (red curve, second y axis) for different atom numbers.

Another source of error stems from the fact that we do not prepare the same atom number in every experimental run. As mentioned in section 4.3.4.a, our atom number preparation scheme generates an atom number with binomial distribution. Naturally, we choose a pulse length t_{opt} for the MW pulse which maximizes the fidelity for the mean atom number N_{mean}. If a different atom number is prepared, the fidelity is reduced. We have estimated the corresponding error by averaging the fidelities at t_{opt} for different atom numbers, weighted by a binomial distribution $\mathcal{B}$ with $N_{mean} = 10$ and standard deviation $\sigma = 2.8$ (the same σ as in the atom number preparation for $N = 12$, see section

4.3.4.a) and found that it is below 1%.

6.2.2. Preliminary results

In this section, we present preliminary data indicating the preparation of an entangled state through the QZD. The principle of the experiment is described in figure 6.6. We prepare an ensemble with well-defined in the state $|0_N\rangle$ using the same technique as described in section 3.1 (1). The system is transferred to the state $|N_N\rangle$ by a π-pulse from a resonant MW (2). Then the probe light is turned on and a MW pulse of length $t = \pi/2\Omega_Z$ transfers the system into the state $|1_N\rangle$ (3). The state is then ready for tomography.

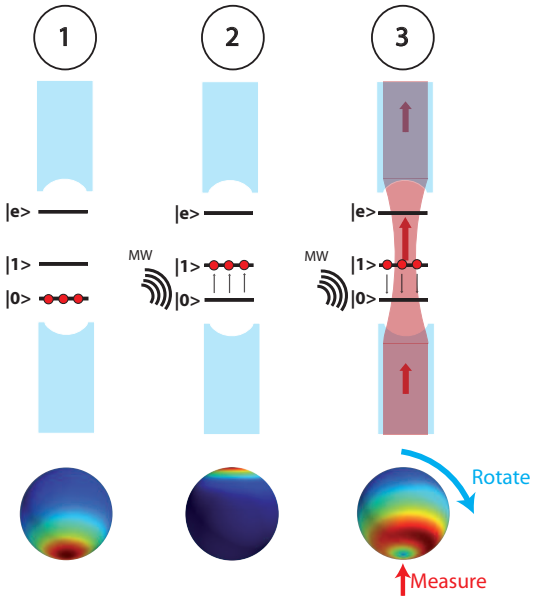

Figure 6.6.: The principle of the W state generation via the QZD. The consecutive steps are explained in the main text.

Figure 6.7 shows tomography curves of such a state for different probe intensities η. At low η, the system is not measured and can freely evolve into the state $|0_N\rangle$. The tomography therefore just shows a coherent state (blue curve). For intermediate η, the evolution to $|0_N\rangle$ is prohibited and the system evolves into the state $|1_N\rangle$. In the tomography, the characteristic dip of the W state becomes visible (green curve). If η is further increased, spontaneous emission becomes the dominant source of error and the contrast of the tomography signal is reduced (red curve).

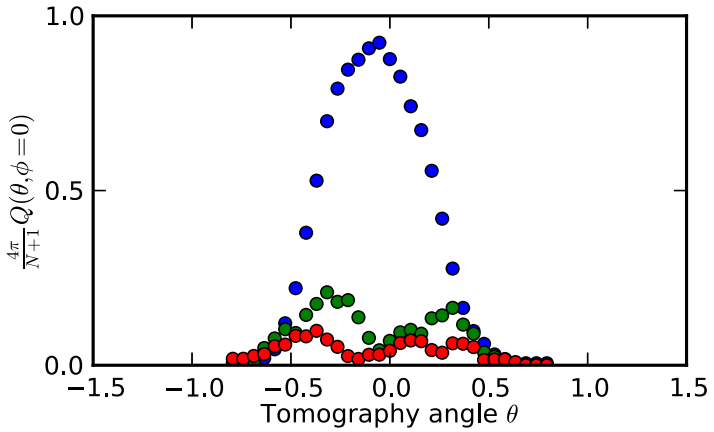

Figure 6.7.: Tomography of a W state, generated via QZD. The different curves show the created state for increasing pump rate η from blue to green and red.

The data presented here are preliminary. In particular the state detection for the tomography measurement is not yet well-calibrated, which can be seen in the distorted shape of the Q function of the coherent state. Nonetheless, the hitherto existing data are promising. Figure 6.8 shows the Q function of a state with $N = 33$ atoms, prepared at the optimum probe power (green curve in figure 6.7), together with the Q function obtained from quantum state reconstruction (using the ML technique, see section 5.1.1). The populations ρ_{nn} in the first three Dicke states $|n_N\rangle$, $n = 0, 1, 2$ read

$$[\rho_{00}, \rho_{11}, \rho_{22}] = [0.05, 0.54, 0.03] \tag{6.23}$$

This corresponds to 17 entangled particles. We would like to stress the fact that this result was obtained in an unconditional measurement without any postselection. The state is indeed prepared in every experimental run.

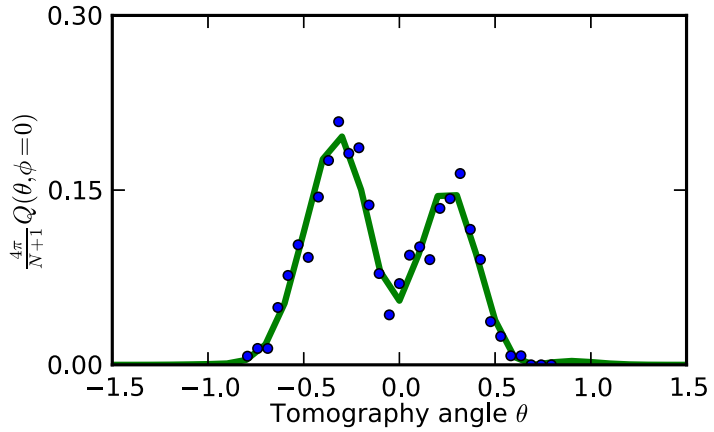

Figure 6.8.: Tomography of a W state, generated via QZD (blue points) and the expected Q function from the quantum state reconstruciton (green curve).

6.3. Conclusion

In this chapter, we have shown that our experimental setup can be used to generate multiparticle entanglement via QZD. Under constant realization of cavity measurements, the intracavity state can freely evolve in the subspace with at least one atom in $F = 2$. Based on this effect, we have presented a proposition to create W states. Furthermore, we have performed simulations to give optimal experimental parameters and an upper bound for the attainable fidelity.

Finally, we have shown preliminary measurements which yield promising results.

7. Conclusion

In this thesis, we have presented a comprehensive toolbox for the creation and characterization of multiparticle entangled states: We have demonstrated a method to prepare a well-defined number of atoms up to $N = 73$ inside an optical resonator. We have created multiparticle entanglement in an entanglement scheme based on weak excitation and a collective, quantum non-destructive measurement. Finally, the states have been analyzed using a new tomography method, which consists in a direct measurement of the Husimi Q function.

These three building blocks enabled us to create W states in an ensemble of up to 41 atoms and to infer the states' density matrix in the symmetric subspace. Further analysis of the tomography has shown that the state with highest atom number $N = 41$ and highest fidelity 0.42 contains at least 13 entangled particles despite all experimental imperfections.

Our tomography method realizes the first direct measurement of a quasiprobability distribution for material particles. It is conceptually simple and only relies on collective rotation of the state and a measurement of its overlap with a coherent state. It can therefore be transposed to other physical systems, notably to experiments featuring a cavity, such as recent ion experiments [130] or experiments combining superconducting qubits with stripline MW cavities [91]. Our tomography technique is a convenient tool to characterize systems where the Hilbert space is too big to allow for a full tomography but where characterization at the single particle level is nonetheless required.

Possible applications for both the entanglement and characterization method can be found in quantum metrology, where testing of different entanglement schemes with regard to their metrological gain requires the possibility of analysis at the single particle level. Such a precision is difficult to obtain for large entangled states due to the scaling of the phase sensitivity with atom number. Instead, an entanglement scheme could be tested by producing a state of mesoscopic atom number which then could be fully characterized using our tomography technique.

Some suggestions for future experiments with our experimental setup have already been given in the course of this thesis: We proposed a method to count the atom number in the QND regime, which could open up the possibility to create other entangled states such as higher-order Dicke states.

We have presented preliminary results on an experiment investigating the creation of multiparticle entanglement via QZD. Our tomography method could be used to retrace the temporal evolution of the atomic ensemble in a subspace defined by the cavity measurement.

Changes in the setup can further increase the performance and versatility of our experimental system and enable the study of different physical phenomena. By using fibre cavities with state of the art mirror coatings, the finesse could be increased by a factor of 4, which reduces the scattering probability and the error of the internal state detection. This could e.g. enable us to extend the QZD to other subspaces by choosing different cavity measurement parameters. The reduction of the scattering probability could make it possible to create entangled states in QZD schemes that only arise after longer evolution times. Alternatively, successive steps of state rotation and QND detection could be combined to create a large range of entangled states. Furthermore, we are currently investigating the possibility to fabricate cavities with high finesse for two different wavelengths, namely for light at $\lambda_p = 780\,\text{nm}$ and the double wavelength $\lambda_d = 1560\,\text{nm}$. Figure 7.1 depicts the envisaged experimental system.

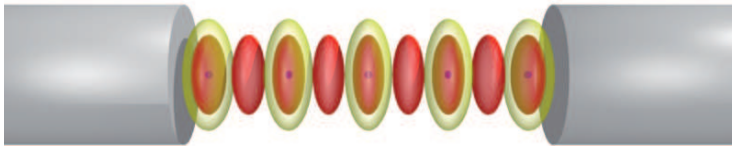

Figure 7.1.: Schematic of a cavity with high finesse at λ_p and λ_d. The standing-wave pattern of the probe light perfectly overlaps with the one of the dipole light (yellow). The atom number in each trapping site can be forced to be either 1 or 0 by inducing a loss process due to light-assisted collisions. All atoms are maximally coupled to the cavity mode. (Image by Claire Lebouteiller)

The light at $\lambda_d = 1560\,\text{nm}$ serves as a dipole trap. The antinodes of the standing-wave patterns for the different wavelengths perfectly overlap, ensuring maximum coupling to the cavity mode at every trapping site. The sites can be loaded directly from a MOT and a loss process due to light assisted collisions assures that either one or no atom is trapped in one site. The distance between the trapping sites is big enough to address individual atoms with a focused light beam perpendicular to the cavity axis.

Such an experimental system allows for the state readout and manipulation of single particles and at the same time enables the techniques based on collective measurement presented in this thesis. The possibility to excite the atoms with light beams perpendicular to the cavity axis gives the possibility to drive Raman transitions and makes the system a well-suited tool to study the creation of entanglement via reservoir engineering [131, 132] or the occurrence of entanglement in the vicinity of the Dicke quantum phase transition [25].

Appendix A.

Chip fabrication

A.1. Electroplating

The chip fabrication closely follows the fabrication recipe described in the appendix C.2 of [74] and we therefore only report the changes that were made with respect to this fabrication recipe. The numbering also follows [74].

Substrate preparation

Since we use 2" x 2" AlN-wavers instead of Si-wavers, we do not need to cleave or oxidize the substrate.

After [4. Clean substrate], the substrate is heated on a hot plate for >2h and is put into the plasma cleaner without delay.

Lower gold layer

1. Deposit gold seed layer

We use a thermal evaporation chamber instead of an e-beam evaporation chamber. Therefore, the deposition speed of Ti cannot be well controlled. It is nonetheless important to keep the Ti-layer as thin as possible (preferably at 2 nm) so that it can be easily removed afterwards.

The immediate deposition of gold after the start of the evaporation process can lead to droplike bumps of a thickness of ≈3 µm and width of ≈10 µm. To avoid this, evaporate ≈20 nm of gold before opening the shutter.

2. Spin on photo resist

For the FFP-chips, we need wire structures of a height of 7 µm and therefore cannot use the spinning values proposed in [74]. We calibrated the thickness of the photoresist with respect to the spinning velocity in an independent measurement.

We were spinning 6 s at 800 rpm and 41 s at v rpm.

v [rpm]	thickness photoresist ma-P 1240 [μm]
900	7.3
1100	6.6
1300	6.4
1500	6.3

For our chip production, the configuration “6s @ 800rpm, 41s @ 900rpm” is used.

3. Resist exposure and development

The exposure time depends on the intensity of the lamp and of the structure size compared to the substrate size (Due to surface tension effects, the photoresist is thicker at the edges of the substrate. That is why for a given substrate size, longer exposure times have to be used for bigger structures). We expose for 83 s for the base chip and for 78 s for the science chip.

The developer ma-D 336 used in [74] is not sold anymore. We therefore use undiluted ma-D 331 and develop for approx. 47 s.

4. Electroplating

Due to the bigger surface of the wire structures compared to [74], we use a higher voltage of $U = 16\,\mathrm{V}$ (for a corresponding current of $I = 16\,\mathrm{mA}$). The time to electroplate the gold layer to a thickness of $7\mu\mathrm{m}$ is ≈70 min for the base chip and ≈55 min for the science chip.

5. Remove photoresist and etch seed layer

The bath of aqua regia does not fully remove the Ti-layer. We therefore add a phase of dry etching (≈ 30 s in plasma SF_6) after the bath of aqua regia.

A.2. Glueing

All glues are degassed for 30 minutes in the plasma cleaner at $\approx 1 \cdot 10^{-2}\,\mathrm{mbar}$.

EpoTek 353ND is used to glue the dielectric coating to the science chip. We put four drops on the chip with the help of a thin wire ($\varnothing = 0.5\,\mathrm{mm}$). Then the transfer coating is put on top and pressed down by a 100 g weight. The glue is *not* brought in a trapezoid form before putting on the coating, since this introduces air bubbles. The ensemble chip/coating is then degassed in the plasma cleaner and heated on a hot plate for 1½ hours at 90°C plus 20 minutes at 120°C.
After transfer, the dielectric coating shows small stains. They are not air bubbles but probably residues from the transfer coating and do not explode in vacuum or otherwise affect the mirror properties.

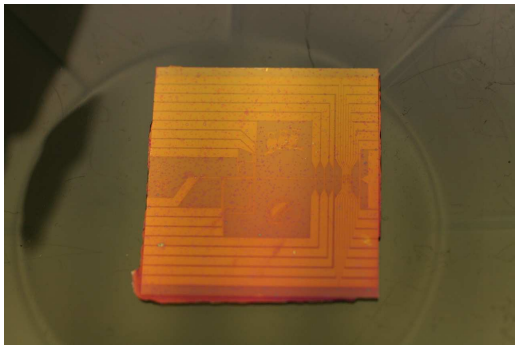

Figure A.1.: Stains on the transfer coating, visible as dark spots. They can easily be distinguished from air bubbles which have a brighter color (an air bubble can for example be found on the lower left of Minerva's head).

The thickness of the glue and coating layer is determined with a stylus profilometer to be around 15±5 µm, depending on the amount of glue. The thickness of the coating layer is 2.5 µm.

EpoTek H77 is used to glue the base chip to the science chip. 12 drops are placed on the science chip using a toothpick and the glue is brought into a trapezoid form. Then the base chip is placed on top and pressed down by a 100 g weight. The ensemble is *not* degassed after assembly, as this introduces small air bubbles for viscous glues. The assembly is heated on a hot plate for 1hour at 100°C plus 2hours at 125°C. During the curing of the glue, the position of the science chip on the base substrate is monitored with a USB microscope (Veho VMS-001), which enables alignment with a precision of 50 µm.

Two microscope slides were glued together to measure the thickness of the glue layer. The thickness was determined with an optical microscope to be 70±5 µm.

Probably due to the mismatch of the different thermal expansion coefficients, small cracks are visible in the dielectric coating after the heating process (see figure A.2). This feature has been observed in all previous experiments and does not significantly affect the performance of the mirror [133].

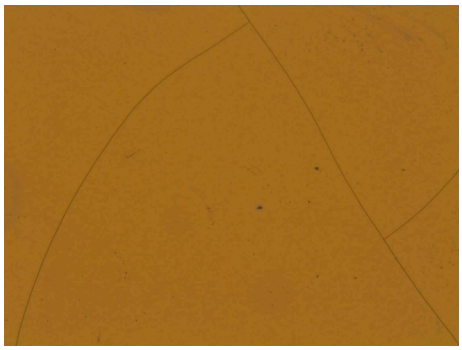

Figure A.2.: After heating of the glue, cracks are visible in the coating.

A.3. Bonding

The dielectric coating is removed in a small region on the border of the science chip (≈1 mm) with a scalpel. The science chip is then connected to the base chip with 14 bond wires (Au, ∅ = 25 µm) per connection.

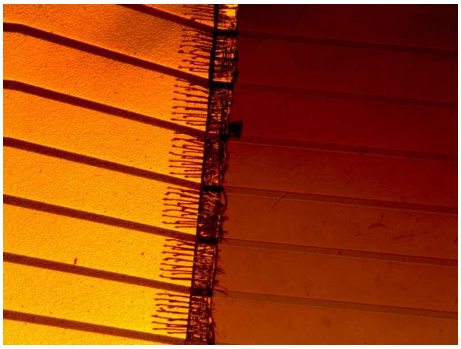

Figure A.3.: Electric connection between the base chip (left) and the science chip (right) with 14 bonding wires per chip wire.

A.4. Beveling of the chip edges

We found that the AlN base chip could not be easily plugged into the PCI-connectors which we use for the electrical connection of the chip in the experiment. We therefore beveled the chip edges with abrasive paper (grain size p80). To reduce dust generation, we soaked the paper in isopropanol prior to abrading. Afterwards, the thin film of dust around the beveled edge was removed with isopropanol.

This method was used on the fully glued and bonded chip assembly. The chips were then inspected with a microscope to ensure that no dust was deposited on the chip and that the bonding wires were not damaged.

For future chip productions, we recommend to bevel the edges of the substrate before processing the chip.

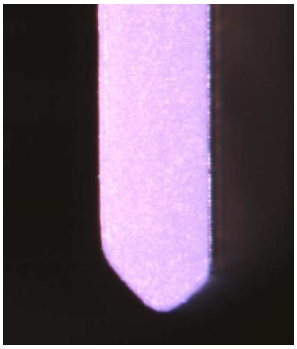

Figure A.4.: The edge of the base chip after beveling. The chip can now be easily plugged into a PCI-connector.

A.5. Tests

Testing the optical properties Collimated light at 780nm was sent onto chip surface at an angle of 45° and the reflection was inspected in the near field with an IR viewer. The pattern of the wires is always visible in the reflected image of the chip (we also took a picture with a "uEye" camera, but the pattern of the wires is not well visible with this imaging technique, see figure A.5).

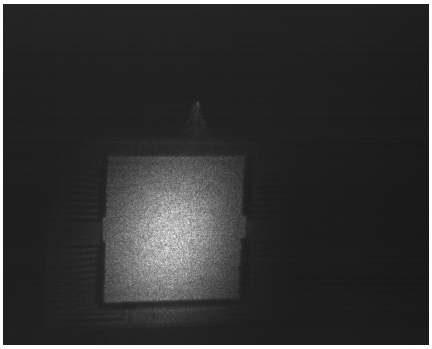

Figure A.5.: Camera image of laser light reflected by the chip mirror. The wire structure is better visible with an IR viewer.

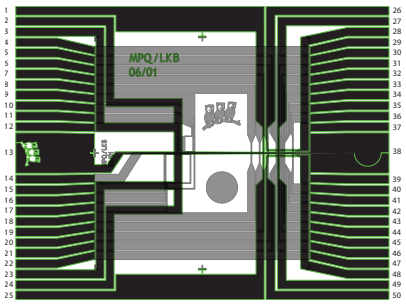

Figure A.6.: The numbering of the chip connections.

Testing the electrical properties The chip was electronically connected to a test board with a a PCI-connector and dip-switches. The resistance of selected wires was then measured with a Multimeter [1] in a two-point measurement (this means that the resistance of the ensemble chip-wire + connector + cable was measured). The insulation between the wires on the science chip was verified by measuring the resistance between the p-Mot wire and adjacent wires.

Bad adhesion of the gold layer to the chip surface could degrade the thermal conductance, leading to heating and even burn-out of the gold wires. We therefore also measured the time resolved resistance for high currents: We sent up to 3 A through the

1. Keithley 2701

wires and measured the voltage drop during 10 s, which largely exceeds the requirements on the wires in a normal experimental run. The increase in relative resistance was at most 12% for the wire with the highest resistance (MIWG, connections 14-39).

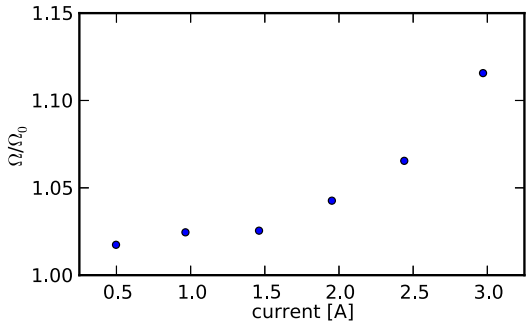

Figure A.7.: Relative resistance of the MIWG wire in dependence of the current after 10 s.

A.6. Remarks and propositions for future chip productions

- After the deposition of the gold seed layer, there are sometimes bumps of gold with a thickness of ≈3 µm and expansion of ≈10 µm on the substrates. There are two possible reasons for this:
  - Due to an increased temperature in the evaporation chamber, water is outgassing from the AlN substrate.
  - The gold is heated to be evaporated and deposited on the substrate. In the beginning, it is boiling and releases huge droplets of gold.

  To fight this problem, we outgassed the chips for >2h on a hot plate before evaporation and deposited an initial layer of gold onto the closed shutter. After these actions, we could observe much less bumps on the substrates. However, since we only had a limited number of substrates, we could not determine which of the possible mechanisms is the reason for the bumps. This could be further investigated.
- There is dirt somewhere in the optical path of the mask aligner, creating a stain on the exposed structure. Even after opening the instrument and cleaning the accessible mirrors, it could not be removed. The mask pattern therefore has to be exposed on a test sample first and the mask has to be aligned so that the shadow of the stain falls onto the chrome.
- Since the bath of aqua regia could not totally remove the Ti-layer, we used dry etching with a SF_6 plasma to remove the Ti traces. This plasma etches 0,5nm/s and contrary to the aqua regia, it reduces the surface roughness. It could therefore be investigated if the wet etching can be replaced by dry etching.
- As in previous fabrication processes, we used the photo resist ma-P 1240 by MicroResist. According to the datasheet, the resist ma-P 1275 is much better suited for wire structures of a thickness of ≈7 µm.

Appendix B.

Details on the derivation of the entanglement criterion

We want to maximize the function

$$F_N(\alpha_1, \ldots, \alpha_N) = \sum_{i=1}^{N} \frac{\sqrt{1-\alpha_i^2}}{\alpha_i} \tag{B.1}$$

with $\alpha_i \in]0,1]$ under the constraint $\prod_{i=1}^{N} \alpha_i^2 = \rho_{00}$. We introduce $N \geq n > 0$, such that $\alpha_{n+1} = \cdots = \alpha_N = 1$ and replace the constraint by

$$\sum_{i=1}^{n} \alpha_i = \ln C \tag{B.2}$$

with $C = \sqrt{\rho_{00}}$. We then introduce the Lagrange multiplier λ and study the Lagrange function

$$\Lambda(\alpha_1, \ldots, \alpha_n, \lambda) = \sum_{i=1}^{n} \frac{\sqrt{1-\alpha_i^2}}{\alpha_i} - \lambda[\sum_{i=1}^{n} \ln \alpha_i - \ln C] \tag{B.3}$$

$$= \sum_{i=1}^{n} f(\alpha_i) - \lambda[\sum_{i=1}^{n} \ln \alpha_i - \ln C] \tag{B.4}$$

with $f(\alpha_i) = \frac{\sqrt{1-\alpha_i^2}}{\alpha_i}$.

To find the stationary point of Λ, we solve $\frac{\partial}{\partial \alpha_i} \Lambda(\alpha_1, \ldots, \alpha_n, \lambda) = 0$, which leads to the set of n equations

$$f'(\alpha_i) = \frac{\lambda}{\alpha_i} \,. \tag{B.5}$$

From $\alpha_i f'(\alpha_i) = \frac{1}{\sqrt{\alpha_i^2 - \alpha_i^4}}$, we obtain the equation

$$-\frac{1}{\sqrt{\alpha^2 - \alpha^4}} = \lambda \,, \tag{B.6}$$

which contains two possible solutions α_1 and α_2, with $\alpha_2 = \sqrt{1-\alpha_1^2}$.

An extremum of Λ is therefore reached when n_1 of the α_i are equal to α_1 and n_2 of the α_i are equal to α_2.

The α_i still have to fulfill the constraint (B.2):

$$C = \alpha_1^{n_1} \alpha_2^{n_2} \tag{B.7}$$

$$= \alpha_1^{n_1} \left(\sqrt{1-\alpha_1^2}\right)^{n_2}, \qquad n_1 + n_2 = n \tag{B.8}$$

To find the maximum of $F_N(\alpha_1, \ldots, \alpha_N)$ for a given C, we can now distinguish between two different cases:

1. $n_1 = 0$ or $n_2 = 0$:
   Then all α_i with $i = 1, \ldots, n$ are equal and it follows
   $$\mathrm{Max}[F_N(\alpha_1, \ldots, \alpha_N)] = n\, f(C^{1/n}) \tag{B.9}$$

2. $n_1 > 1$ and $n_2 > 1$:
   From (B.8), we obtain that the maximum attainable C is
   $$C_{\max} = \frac{n_1^{n_1/2} n_2^{n_2/2}}{(n_1 + n_2)^{(n_1+n_2)/2}}, \tag{B.10}$$
   reached for $\alpha_1 = \sqrt{n_1/(n_1+n_2)}$. For $C = C_{\max}$, the maximum of $F_N(\alpha_1, \ldots, \alpha_N)$ therefore is:
   $$\mathrm{Max}[F_N(\alpha_1, \ldots, \alpha_N)] = n_1\, f(\sqrt{\frac{n_1}{n_1+n_2}}) + n_2\, f(\sqrt{\frac{n_2}{n_1+n_2}}) \tag{B.11}$$
   For a given $C < C_{\max}$, there exist two solutions to (B.8): α_- and α_+, where
   $$\alpha_+ > \sqrt{\frac{n_1}{n_1+n_2}} > \alpha_- \tag{B.12}$$
   In this case, the maximum of $F_N(\alpha_1, \ldots, \alpha_N)$ is
   $$\begin{aligned}\mathrm{Max}[F_N(\alpha_1, \ldots, \alpha_N)] = \mathrm{Max}[&n_1\, f(\alpha_+) + n_2\, f(\sqrt{1-\alpha_+^2}),\\ &n_1\, f(\alpha_-) + n_2\, f(\sqrt{1-\alpha_-^2})]\end{aligned} \tag{B.13}$$

This leads to the following algorithm to find $\mathrm{Max}[F_N(\alpha_1, \ldots, \alpha_N)]$ for a given C:

- Loop over n_1 from 1 to N
  - Calculate $r_{n_1,0} = n\, f(C^{1/n_1})$
  - Loop over n_2 from 1 to $N - n_1$
    - If $C = C_{\max}$:
      Calculate $r_{n_1,n_2} = n_1\, f(\sqrt{\frac{n_1}{n_1+n_2}}) + n_2\, f(\sqrt{\frac{n_2}{n_1+n_2}})$
    - If $C < C_{\max}$:
      Calculate α_- and α_+ from (B.8)
      Calculate $r_{n_1,n_2} = \mathrm{Max}[n_1\, f(\alpha_+) + n_2\, f(\sqrt{1-\alpha_+^2}),$
      $n_1\, f(\alpha_-) + n_2\, f(\sqrt{1-\alpha_-^2})]$

The maximum of $F_N(\alpha_1, \ldots, \alpha_N)$ is then obtained as

$$\mathrm{Max}[F_N(\alpha_1, \ldots, \alpha_N)] = \mathrm{Max}\left[\{r_{n_1,0}, r_{n_1,n_2}\}\right] \tag{B.14}$$

This means that for a pure FSS, the population ρ_{11} in the state $|1_N\rangle$ fulfills the inequation (cf. (5.39)):

$$\rho_{11} \leq \frac{\rho_{00}}{N} \left(\mathrm{Max}[F_N(\alpha_1, \ldots, \alpha_N)]\right)^2 \tag{B.15}$$

Bibliography

[1] E. Schrödinger, "Are there quantum jumps ?" British Journal for the Philosophy of Science **3**, 233–242 (1952).

[2] C. Cohen-Tannoudji and A. Kastler, "I optical pumping," (Elsevier, 1966), pp. 1–81.

[3] W. D. Phillips and H. Metcalf, "Laser deceleration of an atomic beam," Phys. Rev. Lett. **48**, 596–599 (1982).

[4] P. D. Lett, R. N. Watts, C. I. Westbrook, W. D. Phillips, P. L. Gould, and H. J. Metcalf, "Observation of atoms laser cooled below the doppler limit," Phys. Rev. Lett. **61**, 169– (1988).

[5] E. L. Raab, M. Prentiss, A. Cable, S. Chu, and D. E. Pritchard, "Trapping of neutral sodium atoms with radiation pressure," Phys. Rev. Lett. **59**, 2631–2634 (1987).

[6] A. Ashkin, J. M. Dziedzic, J. E. Bjorkholm, and S. Chu, "Observation of a single-beam gradient force optical trap for dielectric particles," Opt. Lett. **11**, 288–290 (1986).

[7] J. P. Gordon and A. Ashkin, "Motion of atoms in a radiation trap," Phys. Rev. A **21**, 1606– (1980).

[8] M. H. Anderson, J. R. Ensher, M. R. Matthews, C. E. Wieman, and E. A. Cornell, "Observation of bose-einstein condensation in a dilute atomic vapor," Science **269**, 198–201 (1995).

[9] K. B. Davis, "Bose-einstein condensation in a gas of sodium atoms." Phys. Rev. Lett. **75**, 3969–3973 (1995).

[10] J. Klaers, J. Schmitt, F. Vewinger, and M. Weitz, "Bose-einstein condensation of photons in an optical microcavity," Nature **468**, 545–548 (2010).

[11] E. M. Purcell, "Spontaneous emission probabilities at radio frequencies," Phys. Rev. **69,**, 681– (1946).

[12] E. Jaynes and F. Cummings, "Comparison of quantum and semiclassical radiation theories with application to the beam maser," Proc. IEEE **51**, 89–109 (1963).

[13] S. Deleglise, I. Dotsenko, C. Sayrin, J. Bernu, M. Brune, J.-M. Raimond, and S. Haroche, "Reconstruction of non-classical cavity field states with snapshots of their decoherence," Nature **455**, 510–514 (2008).

[14] M. Muecke, E. Figueroa, J. Bochmann, C. Hahn, K. Murr, S. Ritter, C. J. Villas-Boas, and G. Rempe, "Electromagnetically induced transparency with single atoms in a cavity," Nature **465**, 755–758 (2010).

[15] C. Sayrin, I. Dotsenko, X. Zhou, B. Peaudecerf, T. Rybarczyk, S. Gleyzes, P. Rouchon, M. Mirrahimi, H. Amini, M. Brune, J.-M. Raimond, and S. Haroche, "Real-time quantum feedback prepares and stabilizes photon number states," Nature **477**, 73–77 (2011).

[16] Y. Kaluzny, P. Goy, M. Gross, J. M. Raimond, and S. Haroche, "Observation of self-induced rabi oscillations in two-level atoms excited inside a resonant cavity: The ringing regime of superradiance," Phys. Rev. Lett. **51**, 1175–1178 (1983).

[17] D. Meschede, H. Walther, and G. Mueller, "One-atom maser," Physical review letters **54**, 551–554 (1985).

[18] R. J. Thompson, G. Rempe, and H. J. Kimble, "Observation of normal-mode splitting for an atom in an optical cavity," Phys. Rev. Lett. **68**, 1132–1135 (1992).

[19] A. Wallraff, D. I. Schuster, A. Blais, L. Frunzio, R.-S. Huang, J. Majer, S. Kumar, S. M. Girvin, and R. J. Schoelkopf, "Strong coupling of a single photon to a superconducting qubit using circuit quantum electrodynamics," Nature **431**, 162–167 (2004).

[20] J. P. Reithmaier, G. Sek, A. Loffler, C. Hofmann, S. Kuhn, S. Reitzenstein, L. V. Keldysh, V. D. Kulakovskii, T. L. Reinecke, and A. Forchel, "Strong coupling in a single quantum dot-semiconductor microcavity system," Nature **432**, 197–200 (2004).

[21] R. H. Dicke, "Coherence in spontaneous radiation processes," Phys. Rev. **93**, 99–110 (1954).

[22] E. Schrödinger, "Discussion of probability relations between separated systems," Mathematical Proceedings of the Cambridge Philosophical Society **31**, 555–563 (1935).

[23] Y. Colombe, T. Steinmetz, G. Dubois, F. Linke, D. Hunger, and J. Reichel, "Strong atom-field coupling for Bose-Einstein condensates in an optical cavity on a chip," Nature **450**, 272–276 (2007).

[24] J. G. Bohnet, Z. Chen, J. M. Weiner, D. Meiser, M. J. Holland, and J. K. Thompson, "A steady-state superradiant laser with less than one intracavity photon," Nature **484**, 78–81 (2012).

[25] K. Baumann, C. Guerlin, F. Brennecke, and T. Esslinger, "Dicke quantum phase transition with a superfluid gas in an optical cavity," Nature **464**, 1301–1306 (2010).

[26] C. H. Bennett and D. P. DiVincenzo, "Quantum information and computation," Nature **404**, 247–255 (2000).

[27] P. Zoller, T. Beth, D. Binosi, R. Blatt, H. Briegel, D. Bruss, T. Calarco, J. I. Cirac, D. Deutsch, J. Eisert, A. Ekert, C. Fabre, N. Gisin, P. Grangiere, M. Grassl, S. Haroche, A. Imamoglu, A. Karlson, J. Kempe, L. Kouwenhoven, S. Kröll, G. Leuchs, M. Lewenstein, D. Loss, N. Lütkenhaus, S. Massar, J. E. Mooij, M. B. Plenio, E. Polzik, S. Popescu, G. Rempe, A. Sergienko, D. Suter, J. Twamley, G. Wendin, R. Werner, A. Winter, J. Wrachtrup, and A. Zeilinger, "Quantum information processing and communication," The European Physical Journal D - Atomic, Molecular, Optical and Plasma Physics **36**, 203–228 (2005).

[28] H.-J. Briegel, W. Dür, J. I. Cirac, and P. Zoller, "Quantum repeaters: The role of imperfect local operations in quantum communication," Phys. Rev. Lett. **81**, 5932– (1998).

[29] V. Giovannetti, S. Lloyd, and L. Maccone, "Quantum-enhanced measurements: Beating the standard quantum limit," Science **306**, 1330–1336 (2004).

[30] L. Pezze and A. Smerzi, "Entanglement, nonlinear dynamics, and the heisenberg limit," Phys. Rev. Lett. **102**, 100401– (2009).

[31] C. A. Sackett, "Experimental entanglement of four particles." Nature **404**, 256–259 (2000).

[32] D. Leibfried, E. Knill, S. Seidelin, J. Britton, R. B. Blakestad, J. Chiaverini, D. B. Hume, W. M. Itano, J. D. Jost, C. Langer, R. Ozeri, R. Reichle, and D. J. Wineland, "Creation of a six-atom /'schrodinger cat/' state," Nature **438**, 639–642 (2005).

[33] H. Häffner, W. Hänsel, C. F. Roos, J. Benhelm, D. Chek-al kar, M. Chwalla, T. Körber, U. D. Rapol, M. Riebe, P. O. Schmidt, C. Becher, O. Gühne, W. Dür, and R. Blatt, "Scalable multiparticle entanglement of trapped ions," Nature **438**, 643–646 (2005).

[34] L. DiCarlo, M. D. Reed, L. Sun, B. R. Johnson, J. M. Chow, J. M. Gambetta, L. Frunzio, S. M. Girvin, M. H. Devoret, and R. J. Schoelkopf, "Preparation and measurement of three-qubit entanglement in a superconducting circuit," Nature **467**, 574–578 (2010).

[35] M. Baur, A. Fedorov, L. Steffen, S. Filipp, M. P. da Silva, and A. Wallraff, "Benchmarking a quantum teleportation protocol in superconducting circuits using tomography and an entanglement witness," Phys. Rev. Lett. **108**, 040502– (2012).

[36] A. Fedorov, L. Steffen, M. Baur, M. P. da Silva, and A. Wallraff, "Implementation of a toffoli gate with superconducting circuits," Nature **481**, 170–172 (2012).

[37] R. Blatt and D. J. Wineland, "Entangled states of trapped atomic ions," Nature **453**, 1008–1014 (2008).

[38] T. Monz, P. Schindler, J. T. Barreiro, M. Chwalla, D. Nigg, W. A. Coish, M. Harlander, W. Hänsel, M. Hennrich, and R. Blatt, "14-qubit entanglement: Creation and coherence," Phys. Rev. Lett. **106**, 130506– (2011).

[39] I. D. Leroux, M. H. Schleier-Smith, and V. Vuletić, "Implementation of cavity squeezing of a collective atomic spin," Phys. Rev. Lett. **104**, 073602– (2010).

[40] M. H. Schleier-Smith, I. D. Leroux, and V. Vuletić, "States of an ensemble of two-level atoms with reduced quantum uncertainty," Phys. Rev. Lett. **104**, 073604– (2010).

[41] C. Gross, T. Zibold, E. Nicklas, J. Estève, and M. K. Oberthaler, "Nonlinear atom interferometer surpasses classical precision limit," Nature **464**, 1165–1169 (2010).

[42] M. F. Riedel, P. Böhi, Y. Li, T. W. Hänsch, A. Sinatra, and P. Treutlein, "Atom-chip-based generation of entanglement for quantum metrology," Nature **464**, 1170–1173 (2010).

[43] C. W. Chou, H. de Riedmatten, D. Felinto, S. V. Polyakov, S. J. van Enk, and H. J. Kimble, "Measurement-induced entanglement for excitation stored in remote atomic ensembles," Nature **438**, 828–832 (2005).

[44] T. Chaneliere, D. N. Matsukevich, S. D. Jenkins, S.-Y. Lan, T. A. B. Kennedy, and A. Kuzmich, "Storage and retrieval of single photons transmitted between remote quantum memories," Nature **438**, 833–836 (2005).

[45] R. Heidemann, U. Raitzsch, V. Bendkowsky, B. Butscher, R. Löw, L. Santos, and T. Pfau, "Evidence for coherent collective rydberg excitation in the strong blockade regime," Phys. Rev. Lett. **99**, 163601– (2007).

[46] H. Carmichael, *An Open Systems Approach to Quantum Optics* (Springer-Verlag, 1992).

[47] M. J. Collett and C. W. Gardiner, "Squeezing of intracavity and traveling-wave light fields produced in parametric amplification," Phys. Rev. A **30**, 1386–1391 (1984).

[48] G. Hechenblaikner, M. Gangl, P. Horak, and H. Ritsch, "Cooling an atom in a weakly driven high-q cavity," Phys. Rev. A **58**, 3030– (1998).

[49] R. Grimm, M. Weidemuller, and Y. B. Ovchinnikov, "Optical dipole traps for neutral atoms," Adv. At. Mol. Opt. Phys. **42**, 95–170 (2000).

[50] B. Darquié, "Manipulation d' atomes dans des pièges dipolaires microscopiques et émission contrôlée de photons par un atome unique," Ph.D. thesis, Université Paris Sud (2005).

[51] R. Gehr, "Cavity based high-fidelity and non-destructive single atom detection on an atom chip," Ph.D. thesis, Université Pierre et Marie Curie (2011).

[52] M. Tavis and F. W. Cummings, "Exact solution for an n-molecule radiation-field hamiltonian," Phys. Rev. **170**, 379–384 (1968).

[53] L. Lugiato, "Theory of optical bistability," Progress in optics **21**, 69–216 (1984).

[54] P. Kwiat, H. Weinfurter, T. Herzog, A. Zeilinger, and M. A. Kasevich, "Interaction-free measurement," Phys. Rev. Lett. **74**, 4763–4766 (1995).

[55] T. Steinmetz, "Resonator-quantenelektrodynamik auf einem mikrofallenchip," Ph.D. thesis, Ludwig-Maximilians-Universitat München (2008).

[56] G. Dubois, "Preparation, manipulation et detection d'atomes uniques sur une puces à atome," Ph.D. thesis, LKB-ENS (2009).

[57] W. Hansel, P. Hommelhoff, T. W. Hansch, and J. Reichel, "Bose-einstein condensation on a microelectronic chip," Nature **413**, 498–501 (2001).

[58] S. W. Du, "Atom-chip bose-einstein condensation in a portable vacuum cell," Phys. Rev. A **70**, 053606– (2004).

[59] L. Ricci, M. Weidemüller, T. Esslinger, A. Hemmerich, C. Zimmermann, V. Vuletic, W. König, and T. W. Hänsch, "A compact grating-stabilized diode laser system for atomic physics," Optics Communications **117**, 541–549 (1995).

[60] G. C. Bjorklund, "Frequency-modulation spectroscopy: a new method for measuring weak absorptions and dispersions," Opt. Lett. **5**, 15–17 (1980).

[61] G. C. Bjorklund, M. D. Levenson, W. Lenth, and C. Ortiz, "Frequency modulation (fm) spectroscopy," Applied Physics B: Lasers and Optics **32**, 145–152 (1983-11-01).

[62] E. A. Donley, T. P. Heavner, F. Levi, M. O. Tataw, and S. R. Jefferts, "Double-pass acousto-optic modulator system," Review of Scientific Instruments **76**, 063112 (2005).

[63] R. Drever, J. Hall, F. Kowalski, J. Hough, G. Ford, A. Munley, and H. Ward, "Laser phase and frequency stabilization using an optical resonator," Applied Physics B: Lasers and Optics **31**, 97–105 (1983).

[64] J. Reichel, W. Hansel, and T. W. Hansch, "Atomic micromanipulation with magnetic surface traps," Phys. Rev. Lett. **83**, 3398–3401 (1999).

[65] R. Folman, P. Krüger, D. Cassettari, B. Hessmo, T. Maier, and J. Schmiedmayer, "Controlling cold atoms using nanofabricated surfaces: Atom chips," Phys. Rev. Lett. **84**, 4749– (2000).

[66] J. Reichel, W. Hänsel, P. Hommelhoff, and T. Hänsch, "Applications of integrated magnetic microtraps," Applied Physics B: Lasers and Optics **72**, 81–89 (2001).

[67] J. D. Weinstein and K. G. Libbrecht, "Microscopic magnetic traps for neutral atoms," Phys. Rev. A **52**, 4004–4009 (1995).

[68] M. P. A. Jones, C. J. Vale, D. Sahagun, B. V. Hall, and E. A. Hinds, "Spin coupling between cold atoms and the thermal fluctuations of a metal surface," Phys. Rev. Lett. **91**, 080401– (2003).

[69] Y.-j. Lin, I. Teper, C. Chin, and V. VuletiÄ‡, "Impact of the casimir-polder potential and johnson noise on bose-einstein condensate stability near surfaces," Phys. Rev. Lett. **92**, 050404– (2004).

[70] S. Aigner, L. D. Pietra, Y. Japha, O. Entin-Wohlman, T. David, R. Salem, R. Folman, and J. Schmiedmayer, "Long-range order in electronic transport through disordered metal films," Science **319**, 1226–1229 (2008).

[71] P. Treutlein, D. Hunger, S. Camerer, T. W. Hänsch, and J. Reichel, "Bose-einstein condensate coupled to a nanomechanical resonator on an atom chip," Physical Review Letters **99**, 140403 (2007).

[72] J. Reichel, "Trapping and manipulating atoms on chips," in "Atom Chips," (Wiley-VCH Verlag GmbH & Co. KGaA, 2011), pp. 33–60.

[73] W. Haensel, "Magnetische mikrofallen fuer rubidiumatome," Ph.D. thesis, Ludwig-Maximilians-Universitaet Muenchen (2000).

[74] P. Treutlein, "Coherent manipulation of ultracold atoms on atom chips," Ph.D. thesis, LMU (2008).

[75] R. Folman, P. Treutlein, and J. Schmiedmayer, "Atom chip fabrication," in "Atom Chips," (Wiley-VCH Verlag GmbH & Co. KGaA, 2011), pp. 61–117.

[76] I. Teper, Y.-J. Lin, and V. Vuletic, "Resonator-aided single-atom detection on a microfabricated chip," Phys. Rev. Lett. **97**, 023002–4 (2006).

[77] F. Brennecke, S. Ritter, T. Donner, and T. Esslinger, "Cavity optomechanics with a bose-einstein condensate," Science **322**, 235–238 (2008).

[78] S. Brakhane, W. Alt, T. Kampschulte, M. Martinez-Dorantes, R. Reimann, S. Yoon, A. Widera, and D. Meschede, "Bayesian feedback control of a two-atom spin-state in an atom-cavity system," Phys. Rev. Lett. **109**, 173601– (2012).

[79] D. Hunger, T. Steinmetz, Y. Colombe, C. Deutsch, T. W. Hänsch, and J. Reichel, "A fiber fabry-perot cavity with high finesse," New Journal of Physics **12**, 065038– (2010).

[80] R. Long, T. Rom, W. Hänsel, T. W. Hänsch, and J. Reichel, "Long distance magnetic conveyor for precise positioning of ultracold atoms," European Physical Journal D **35**, 125–133– (2005).

[81] A. Fuhrmanek, R. Bourgain, Y. R. P. Sortais, and A. Browaeys, "Light-assisted collisions between a few cold atoms in a microscopic dipole trap," Phys. Rev. A **85**, 062708– (2012).

[82] E. D. Black, "An introduction to pound–drever–hall laser frequency stabilization," Am. J. Phys. **69**, 79–87 (2001).

[83] T. M. Niebauer, R. Schilling, K. Danzmann, A. Rüdiger, and W. Winkler, "Nonstationary shot noise and its effect on the sensitivity of interferometers," Phys. Rev. A **43**, 5022–5029 (1991).

[84] T. T. Lyons, M. W. Regehr, and F. J. Raab, "Shot noise in gravitational-wave detectors with fabry-perot arms," Appl. Opt. **39**, 6761–6770 (2000).

[85] T. Holstein and H. Primakoff, "Field dependence of the intrinsic domain magnetization of a ferromagnet," Phys. Rev. **58**, 1098–1113 (1940).

[86] F. T. Arecchi, E. Courtens, R. Gilmore, and H. Thomas, "Atomic coherent states in quantum optics," Phys. Rev. A **6**, 2211–2237 (1972).

[87] W. Duer, G. Vidal, and J. I. Cirac, "Three qubits can be entangled in two inequivalent ways," Phys. Rev. A **62**, 062314– (2000).

[88] A. Sen(De), U. Sen, M. WieÅ›niak, D. Kaszlikowski, and M. Å»ukowski, "Multiqubit w states lead to stronger nonclassicality than greenberger-horne-zeilinger states," Phys. Rev. A **68**, 062306– (2003).

[89] H.-N. Xiong, J. Ma, W.-F. Liu, and X. Wang, "Quantum fisher information for superpositions of spin states," Quantum Info. Comput. **10**, 498–508 (2010).

[90] A. Gaetan, Y. Miroshnychenko, T. Wilk, A. Chotia, M. Viteau, D. Comparat, P. Pillet, A. Browaeys, and P. Grangier, "Observation of collective excitation of two individual atoms in the rydberg blockade regime," Nat Phys **5**, 115–118 (2009).

[91] J. A. Mlynek, J. Abdumalikov, A. A., J. M. Fink, L. Steffen, M. Baur, C. Lang, A. F. van Loo, and A. Wallraff, "Demonstrating w-type entanglement of dicke states in resonant cavity quantum electrodynamics," Phys. Rev. A **86**, 053838– (2012).

[92] W. Wieczorek, R. Krischek, N. Kiesel, P. Michelberger, G. Tóth, and H. Weinfurter, "Experimental entanglement of a six-photon symmetric dicke state," Phys. Rev. Lett. **103**, 020504– (2009).

[93] J. M. Radcliffe, "Some properties of coherent spin states," Journal of Physics A: General Physics **4**, 313– (1971).

[94] R. Friedberg and J. Manassah, "Dicke states and bloch states," Laser Phys. Lett. **4**, 900–911 (2007).

[95] J. P. Dowling, G. S. Agarwal, and W. P. Schleich, "Wigner distribution of a general angular-momentum state: Applications to a collection of two-level atoms," Phys. Rev. A **49**, 4101– (1994).

[96] R. Schmied and P. Treutlein, "Tomographic reconstruction of the wigner function on the bloch sphere," New Journal of Physics **13**, 065019– (2011).

[97] T. Zibold, "Classical bifurcation and entanglement generation in an internal bosonic josephson junction," Ph.D. thesis, Ruperto-Carola-University of Heidelberg (2012).

[98] K. Husimi, "Some formal properties of the density matrix," Proc. Phys. Math. Soc. Jpn **22**, 264–314 (1940).

[99] G. S. Agarwal, "State reconstruction for a collection of two-level systems," Phys. Rev. A **57**, 671–673 (1998).

[100] A. N. Kolmogorov, *Grundbegriffe der Wahrscheinlichkeitsrechnung* (Springer, 1933).

[101] K. E. Cahill and R. J. Glauber, "Density operators and quasiprobability distributions," Phys. Rev. **177**, 1882–1902 (1969).

[102] S. Kuhr, W. Alt, D. Schrader, I. Dotsenko, Y. Miroshnychenko, A. Rauschenbeutel, and D. Meschede, "Analysis of dephasing mechanisms in a standing-wave dipole trap," Phys. Rev. A **72**, 023406– (2005).

[103] P. A. M. Dirac, *The Principles of Quantum Mechanics* (Clarendon Press, 1930).

[104] W. K. Wootters and W. H. Zurek, "A single quantum cannot be cloned," Nature **299**, 802–803 (1982).

[105] J. Rehacek, Z. Hradil, and M. Jezek, "Iterative algorithm for reconstruction of entangled states," Phys. Rev. A **63**, 040303– (2001).

[106] A. Lvovsky, "Iterative maximum-likelihood reconstruction in quantum homodyne tomography," Journal of Optics B: Quantum and Semiclassical Optics **6**, S556–(2004).

[107] Z. Hradil, J. Rehacek, J. Fiurasek, and M. Jezek, "3 maximum-likelihood methods in quantum mechanics," in "Lecture Notes in Physics," , vol. 649, M. Paris and J. Rehacek, eds. (Springer Berlin Heidelberg, 2004), pp. 59–112–.

[108] V. Bužek, "6 quantum tomography from incomplete data via maxent principle," in "Lecture Notes in Physics," , vol. 649, M. Paris and J. Rehacek, eds. (Springer Berlin Heidelberg, 2004), pp. 189–234–.

[109] G. Sacchi, "Lagrange multiplier methods for optimization with constraints," in "Mathematical Concepts and Methods in Science and Engineering," , vol. 34, M. Save, W. Prager, and W. Warner, eds. (Springer US, 1986), pp. 271–288–.

[110] Y. Vardi and D. Lee, "From image deblurring to optimal investments: Maximum likelihood solutions for positive linear inverse problems," Journal of the Royal Statistical Society. Series B (Methodological) **55**, 569–612 (1993).

[111] A. Dempster, N. Laird, and D. Rubin, "Maximum likelihood from incomplete data via the em algorithm," J. R. Statistic. Soc. B **39**, 1 (1977).

[112] B. Efron and R. J. Tibshirani, *An Introduction to the Bootstrap* (Chapman and Hall/CRC, 1994).

[113] A. Einstein, B. Podolsky, and N. Rosen, "Can quantum-mechanical description of physical reality be considered complete?" Phys. Rev. **47**, 777–780 (1935).

[114] Aristotle, *Metaphysics* (available online at http://classics.mit.edu/Aristotle/metaphysics.html (Translated by W. D. Ross)).

[115] R. Horodecki, P. Horodecki, M. Horodecki, and K. Horodecki, "Quantum entanglement," Rev. Mod. Phys. **81**, 865– (2009).

[116] D. M. Greenberger, M. A. Horne, and A. Zeilinger, "Going beyond bell's theorem," Bell's Theorem, Quantum Theory, and Conceptions of the Universe pp. 69–72 (1989).

[117] Aristotle, *Physics* (Available online at http://classics.mit.edu/Aristotle/physics.html (Translated by R. P. Hardie and R. K. Gaye)).

[118] B. Misra and E. C. G. Sudarshan, "The zeno's paradox in quantum theory," Journal of Mathematical Physics **18**, 756–763 (1977).

[119] H. Nakazato, S. Pascazio, and M. Namiki, "Temporal behavior of quantum mechanical systems," International Journal of Modern Physics B **10**, 247–295 (1996).

[120] W. M. Itano, D. J. Heinzen, J. J. Bollinger, and D. J. Wineland, "Quantum zeno effect," Phys. Rev. A **41**, 2295– (1990).

[121] C. Balzer, R. Huesmann, W. Neuhauser, and P. E. Toschek, "The quantum zeno effect - evolution of an atom impeded by measurement," Optics Communications **180**, 115 (2000).

[122] E. W. Streed, J. Mun, M. Boyd, G. K. Campbell, P. Medley, W. Ketterle, and D. E. Pritchard, "Continuous and pulsed quantum zeno effect," Phys. Rev. Lett. **97**, 260402 (2006).

[123] L. Xiao and J. A. Jones, "Nmr analogues of the quantum zeno effect," Physics Letters A **359**, 424–427 (2006).

[124] M. C. Fischer, B. Gutiérrez-Medina, and M. G. Raizen, "Observation of the quantum zeno and anti-zeno effects in an unstable system," Phys. Rev. Lett. **87**, 040402– (2001).

[125] P. Facchi and S. Pascazio, "Quantum zeno subspaces," Phys. Rev. Lett. **89**, 080401 (2002).

[126] J. M. Raimond, C. Sayrin, S. Gleyzes, I. Dotsenko, M. Brune, S. Haroche, P. Facchi, and S. Pascazio, "Phase space tweezers for tailoring cavity fields by quantum zeno dynamics," Phys. Rev. Lett. **105**, 213601– (2010).

[127] J. Raimond, P. Facchi, B. Peaudecerf, S. Pascazio, C. Sayrin, I. Dotsenko, S. Gleyzes, M. Brune, and S. Haroche, "Quantum zeno dynamics of a field in a cavity," Arxiv (2012).

[128] F. e. a. Schäfer, "Coherent dynamics in a back-action engineered quantum space," Arxiv (2013).

[129] P. Facchi and S. Pascazio, "Quantum zeno dynamics: mathematical and physical aspects," Journal of Physics A: Mathematical and Theoretical **41**, 493001 (45pp) (2008).

[130] B. Brandstätter, A. McClung, K. Schüppert, B. Casabone, K. Friebe, A. Stute, P. O. Schmidt, C. Deutsch, J. Reichel, R. Blatt, and T. E. Northup, "Integrated fiber-mirror ion trap for strong ion-cavity coupling," Review of Scientific Instruments **84**, – (2013).

[131] F. Reiter, M. J. Kastoryano, and A. S. Sørensen, "Driving two atoms in an optical cavity into an entangled steady state using engineered decay," New Journal of Physics **14**, 053022– (2012).

[132] Y. Lin, J. P. Gaebler, F. Reiter, T. R. Tan, R. Bowler, A. S. Sorensen, D. Leibfried, and D. J. Wineland, "Dissipative production of a maximally entangled steady state of two quantum bits," Nature **504**, 415–418 (2013).

[133] T. Schneider, "Chip fabrication report for atomic clock on chip experiment," Tech. rep., Ecole Normale Superieure (2007).